AD-769 064

DESIGN, FABRICATION, TEST, AND EVALUA-
TION OF SPIRAL BEVEL SUPPORT BEARINGS
(TAPERED ROLLER)

A. J. Lemanski, et al

Boeing Vertol Company

Prepared for:

Army Air Mobility Research and Development
Laboratory

June 1973

ACCESSION for		
NTIS	White Section	☒
D.C	Buff Section	☐
UNANNOUNCED		☐
JUSTIFICATION		
BY		
DISTRIBUTION/AVAILABILITY CODES		
Dist.	AVAIL. and/or SPECIAL	

1a

AD 769064

DOCUMENT CONTROL DATA - R & D

(Security classification of title, body of abstract and indexing annotation must be entered when the overall report is classified)

1. ORIGINATING ACTIVITY (Corporate author)	2a. REPORT SECURITY CLASSIFICATION
The Boeing Company Vertol Division Philadelphia, Pennsylvania	Unclassified
	2b. GROUP

3. REPORT TITLE

DESIGN, FABRICATION, TEST, AND EVALUATION OF SPIRAL BEVEL SUPPORT BEARINGS (TAPERED ROLLER)

4. DESCRIPTIVE NOTES (Type of report and inclusive dates)

Final Report

5. AUTHOR(S) (First name, middle initial, last name)

A. J. Lemanski
J. W. Lenski, Jr.
R. J. Drago

6. REPORT DATE	7a. TOTAL NO. OF PAGES	7b. NO. OF REFS
June 1973	185	10

8a. CONTRACT OR GRANT NO. DAAJ02-71-C-0025 b. PROJECT NO. 1G162207AA74 c. d.	9a. ORIGINATOR'S REPORT NUMBER(S) USAAMRDL Technical Report 73-16 9b. OTHER REPORT NO(S) (Any other numbers that may be assigned this report)

10. DISTRIBUTION STATEMENT

Approved for public release; distribution unlimited.

11. SUPPLEMENTARY NOTES	12. SPONSORING MILITARY ACTIVITY Eustis Directorate U.S. Army Air Mobility R&D Laboratory Fort Eustis, Virginia

13. ABSTRACT

This report presents the results of an analytical and experimental program to evaluate the influence of critical bearing parameters on the performance of high-speed (20,000 fpm - 1.42 million DN), high-load (5500-lb thrust, 7500-lb radial) tapered-roller, spiral bevel gear support bearings for use in helicopter transmissions.

The program consisted of a generalized analytical investigation and then an experimental investigation based on the information obtained in the analytical investigation.

In the generalized analytical investigation, a method of analysis was developed which covered bearing kinematics, internal load distribution, oil film thickness, contact stress, and fatigue life. The experimental investigation was conducted on 53 tapered roller bearings of the 6500 series (3.50-in. bore) by performing rotating load testing.

Also, preliminary screening tests were conducted on 13 additional bearings to establish key bearing design modifications.

14. KEY WORDS	LINK A		LINK B		LINK C	
	ROLE	WT	ROLE	WT	ROLE	WT
Tapered roller bearings Spiral bevel support bearings						

1C

6595-73

This report was prepared by The Boeing Company, Vertol
Division, under the terms of Contract DAAJ02-71-C-0025.
It documents the research work to design, fabricate,
test, and evaluate tapered roller bearings for use in
supporting spiral bevel gears in helicopter transmissions.
The report also contains the results of a concurrent
effort carried out by Boeing-Vertol.

The use of tapered roller bearings for reaction of
combined loading produced by spiral bevel gears in
helicopter transmission systems offers distinct advan-
tages. The objectives of this program, which were
successfully accomplished, were to determine the
influence of various design factors on bearing per-
formance. These factors included oil-flow rate, roller-
end/cone-rib geometry, cage design configuration, cage
plating, roller-end and cone-rib finish, and fail-safe
bearing designs.

This report has been reviewed by this Directorate and
is considered to be technically sound. The technical
monitor for this contract was Mr. E. R. Givens, Technology
Applications Division.

id

Project 1G162207AA74
Contract DAAJ02-71-C-0025
USAAMRDL Technical Report 73-16
June 1973

DESIGN, FABRICATION, TEST, AND EVALUATION OF
SPIRAL BEVEL SUPPORT BEARINGS (TAPERED ROLLER)

Final Report

By

A. J. Lemanski
J. W. Lenski, Jr.
R. J. Drago

Prepared by

The Boeing Company, Vertol Division
Boeing Center
Philadelphia, Pennsylvania

for

EUSTIS DIRECTORATE
U.S. ARMY AIR MOBILITY RESEARCH AND DEVELOPMENT LABORATORY
FORT EUSTIS, VIRGINIA

SUMMARY

This report presents the results of an analytical and experimental program to evaluate the influence of critical bearing parameters on the performance of high-speed (20,000 fpm - 1.42 million DN), high-load (5500-pound thrust, 7500-pound radial) tapered-roller, spiral bevel gear support bearings for use in helicopter transmissions.

The program consisted of a generalized analytical investigation and then an experimental investigation based on the information obtained in the analytical investigation.

In the generalized analytical investigation, a method of analysis was developed which covered bearing kinematics, internal load distribution, oil film thickness, contact stress, and fatigue life. This analytical method permitted an evaluation of the following critical design parameters:

- Sliding velocity at cone-rib contact

- Roller centrifugal force and gyroscopic moment

- Declutching thrust load

- Oil film thickness at cone rib and roller race contacts

- Cone-rib contact height

- Cone or cup (inner/outer race flange) rib geometry

- Roller large-end curvature

- Hertz contact stress at cone-rib contact

- Flash temperature index at cone-rib contact

- Spacing of lube holes in cone

- Length of lube-hole orifices in cone

- Cone lube-hole orifice angle

- Fatigue life

The experimental investigation was conducted on 53 tapered roller bearings of the 6500 series (3.50-inch bore) by performing rotating load testing. Approximately half of the bearings were procured and tested under a current company program, and the results are reported herein.

Preceding page blank

Also, preliminary screening tests were conducted on 13 additional test bearings to establish key bearing design modifications. This investigation was successful in meeting the objective and aims of the program. The following results were achieved:

- Oil-flow rate was optimized for operation up to 20,000 fpm (1.42 million DN) based on bearing temperature and torque performance.

- Roller large-end curvature and cone-rib angle were optimized for operation up to 20,000 fpm based on the development of an adequate oil film thickness.

- Three platings (silver, phosphate, and brass) on the standard steel cage were evaluated, and under reduced or marginal oil flow, the silver-plated cages provided the best performance.

- The roller-end (large) and cone-rib surface finish in the range of 3 to 16AA was evaluated, and correlation was found with performance at 20,000 fpm.

- Three steel cage designs were evaluated (standard stamped, flared stamped, and Z-type fully machined); all three performed successfully at 20,000 fpm.

- Eighteen and twenty-four radial lubrication holes through the bearing cone were evaluated; optimization of oil distribution on the cone-rib was achieved with the 24-hole design.

- Four fail-safe bearing designs were evaluated: Vespel ring bonded to the cone rib with a silver-plated cage (the Vespel ring failed at 11,000 fpm); Vespel ring bonded to the cone rib with a boronized case hardened cage (the Vespel ring failed at 11,000 fpm); boronized case-hardened cone rib, large roller end, and cage (examination after 20,000 fpm operation revealed heavy wear on the large end of the rollers); and Tribaloy (Laves Phase) alloy ring brazed to the cone rib with a silver-plated cage (this design configuration operated at 20,000 fpm successfully with no evidence of wear).

FOREWORD

This is the final report of a program for the design, fabrication, test and evaluation of spiral bevel support bearings (tapered roller). This report also includes the work accomplished under a related Boeing-Vertol effort. This contracted program was conducted during the 21-month period from 4 March 1971 through 4 December 1972 for the Eustis Directorate, U.S. Army Air Mobility Research and Development Laboratory under Contract DAAJ02-71-C-0025, DA Project 1G162207AA74.

U.S. Army Air Mobility Research and Development Laboratory technical direction was provided by the Contracting Officer's Technical Representative, Mr. E. Rouzee Givens of the Technology Applications Division.

This program was conducted at the Vertol Division of The Boeing Company under the technical direction of A. J. Lemanski (Program Manager), Chief of Advanced Drive System Technology Department. Principal investigators for the program were Mr. J. W. Lenski, Jr. (Project Engineer) and Mr. R. J. Drago (Theoretical Analyst). Others who contributed to the success of the project at Boeing-Vertol were Mr. S. Binder and Mr. J. C. Mack.

Mr. R. F. Cornish (Applications Development Engineer) and Mr. Gary Dressler of The Timken Company, Physical Laboratories, Canton, Ohio, provided assistance and contributions during the experimental investigation. Mr. A. B. Jones (Bearing Consultant), Newington, Connecticut, derived the bearing fatigue life analysis data.

TABLE OF CONTENTS

Preceding page blank

LIST OF ILLUSTRATIONS

xi

LIST OF TABLES

LIST OF SYMBOLS

A,B   geometric constant, in.^{-1}

a,b   semimajor and semiminor axis of pressure ellipse, in.

a_{CROLL} centrifugal acceleration of roller, in./sec^2

A_H cross-sectional area of flange oil holes, in.^2

BTT   angle between roller-end/flange-load line and bearing centerline, deg

C   thermal constant, $\dfrac{\text{in.-lb}}{\text{in.}^2 \ °F \ \text{sec}^{1/2}}$

C_{DH} discharge coefficient for oil holes

CF   centrifugal force on a roller, lb

C_K thermal conductivity, $\dfrac{\text{in.-lb}}{\text{in. } °F \ \text{sec}}$

C_P specific heat, $\dfrac{\text{in.-lb}}{\text{lb } °F}$

d   mean roller diameter, in.

d'   dimension of pressure ellipse in direction of motion, in.

D_H diameter of flange oil holes, in.

D_I, D_O mean section inner and outer race diameters, respectively, measured to bearing centerline, in.

E   mean pitch diameter, in.

e   eccentricity of pressure ellipse

E_P reduced modulus of elasticity, psi

E_R, E_E modulus of elasticity for race and roller, respectively, psi

f   friction coefficient

F_X, F_Y	forces in X and Y directions, respectively, lb
g	acceleration of gravity, in./sec^2
GM	roller gyroscopic moment, in.-lb
h	film thickness, in.
H_{CG}	distance between roller mean section and roller center of gravity, in.
I_{ROL}	roller mass moment of inertia, lb-sec^2-in.
J	distance between theoretical intersection point between inner race and flange and roller-end/flange contact point, in.
J_C	J_C distance along flange to outer limit of contact band, in.
$\overline{K}, \overline{E}$	complete elliptic integrals of first and second kinds, respectively
L_E	effective roller length, in.
L_T	distance between bearing apex and intersection of a line parallel to the flange and the bearing centerline, in.
L_T'	distance between roller-end curvature center and intersection of the centerline of the second source lube holes with a line through this center and parallel to bearing axis, in.
ℓ	length of roller measured along roller centerline, in.
ℓ_F	effective lubricant path length, in.
M_I, M_O	inner and outer race moments, respectively, in.-lb
M_{ROL}	mass of roller, $\dfrac{\text{lb-sec}^2}{\text{in.}}$
m_R, m_E	poisson's ratio for race and roller, respectively
P_3	load on roller end due to flange, lb
P_I, P_O	inner and outer race loads, respectively, lb

q	heat flux, $\dfrac{\text{in.-lb}}{\text{in.}^2\text{-sec}}$
Q_{IIT}	theoretical flow through oil holes, gpm
R	effective curvature radius in direction of motion, in.
R_{CG}	radius to roller center of gravity, measured perpendicular to bearing centerline, in.
R_{CT}	radius to outer limit of contact band, in.
R_E	roller end spherical radius, in.
R_F	radius of curvature of flange, in.
R_I	radius to theoretical intersection point between inner race and flange, in.
R_I, R_O	effective curvature radii for inner and outer race contacts, respectively, in.
R_{IM}, R_{OM}	radii to inner and outer races respectively, at mean section measured perpendicular to bearing centerline, in.
R_{IMP}, R_{OMP}	radii of curvature of inner and outer races at the mean section, respectively, in.
R'_O	critical flow ratio
R_P	radius to roller-end/flange contact point, measured perpendicular to bearing centerline, in.
R_{RC}	radius perpendicular to bearing centerline to point at which a line through the roller-end/flange contact point perpendicular to the roller centerline crosses the roller centerline, in.
R_{RL}	radius of large end of roller, in.
R_{ROL}	radius of curvature of roller at mean section, in.
R_{RS}	radius of small end of roller
R_X, R_Y	radii of curvature in X and Y directions, respectively, in.

R_{X1}, R_{X2}	curvature radii in X direction for bodies 1 and 2, respectively, in.
R_{Y1}, R_{Y2}	curvature radii in Y direction for bodies 1 and 2, respectively, in.
S_{CRE}	maximum contact stress at roller-end/flange contact, psi
t	distance from roller mean section to roller-end/flange contact point, measured parallel to roller centerline, in.
T_{DC}	bearing declutching thrust load, lb
t_F	time required for oil stream to traverse effective flange area, sec
U	entraining velocity, in./sec
U_P	entraining (mean surface) velocity at the roller-end/flange contact point, in./sec
V_A	oil stream velocity, in./sec
V_{AX}, V_{AY}	oil stream velocity in X and Y directions, respectively, in./sec
V_{AXL}	velocity of oil stream parallel to bearing centerline, in./sec
V_{BADL}	velocity of oil stream perpendicular to bearing centerline, in./sec
V_F	linear velocity of flange at contact point, in./sec
$V_{F/CP}$	linear velocity of the flange at the roller-end/flange contact point with respect to the roller-end/flange contact point, in./sec
V_I, V_O	entraining (mean surface) velocity at inner and outer race mean sections, respectively, in./sec
V_{RE}	linear velocity of roller centerline at the point at which a line through the roller-end/flange contact point perpendicular to the roller centerline crosses the roller centerline, in./sec
V_{ROL}	volume of roller, in.^{3}

V_{RP}	linear velocity of roller at roller-end/flange contact point, in./sec
$V_{RP/CP}$	linear velocity of the roller at the roller-end/flange contact point with respect to the roller-end/flange contact point, in./sec
$V_{RP/RE}$	linear velocity of roller at roller-end/flange contact point with respect to roller centerline, in./sec
V_S	sliding velocity at the roller-end/flange contact point, in./sec
W	contact point load, lb
W'	contact load intensity, lb/in.
W'_I, W'_O	inner and outer race load intensity, respectively, lb/in.
y	distance from roller centerline to roller-end/flange contact point, measured perpendicular to roller centerline, in.
y_{CG}	distance from large end of truncated circular cone to center of gravity, in.
y, y_O	distance to inner and outer points of oil holes, respectively, in.
Z	number of rollers
α	inner race (cone) half angle, deg
α'	pressure-viscosity exponent, in.^{2}/lb
α_O	hole angular spacing, deg
β	outer race (cup) half angle, deg
γ	roller centerline half angle, deg
γ'	angle between inner race and flange, deg
γ_B	flange inclination angle, deg
γ_G	adjusted ratio of roller diameter and mean pitch diameter, deg
γ_H	angle of oil holes with respect to bearing centerline, deg

γ_O angle between V_{AX} and V_{AY} , deg

γ_R angle between direction of ω_P and bearing centerline

γ_{RF} angle between bearing centerline and direction of $\omega_{R/F}$

γ_{RR} angle between vectors $\vec{\omega}_R$ and $\vec{R}$

Δ undercut at inner race/flange junction, in.

δ_{RE} elastic approach of roller-end/flange contact, in.

θ angle between roller centerline and flange roller-end load line, deg

θ_O critical flow angle, deg

$\theta_1, \theta_2, \theta_3$ auxiliary angles used in determining ℓ_F

θ' angle between roller centerline and line joining roller-end/flange contact point with roller-end curvature center, deg

θ'' angle between roller centerline and line joining large end roller outside diameter and flange curvature center, deg

μ_O absolute viscosity, reyns $\left(\dfrac{\text{lb-sec}}{\text{in.}^2}\right)$

ν_R, ν_E material constants for roller and races, respectively, psi^{-1}

ζ switch for determining to which race the flange is attached

ρ_{ROL} weight density of roller, lb/in.^3

τ total roller included angle, deg

ω angle between X axes of bodies 1 and 2, deg

ω_F generalized angular velocity of flange, rad/sec

$\omega_{I/RE}$ angular velocity of inner race with respect to roller centerline, rad/sec

ω_O — angular velocity of outer race, rad/sec

$\omega_{O/RE}$ — angular velocity of outer race with respect to roller centerline, rad/sec

ω_R — angular velocity of roller, rad/sec

ω_{RE} — angular velocity of roller centerline, rad/sec

$\omega_{RE/F}$ — generalized angular velocity of roller centerline with respect to flange, rad/sec

$\omega_{R/F}$ — angular velocity of roller with respect to flange, rad/sec

$\omega_{R/RE}$ — angular velocity of roller about its own centerline, rad/sec

ω_1, ω_2 — angle between X axes of bodies 1 and 2, respectively, and pressure ellipse axes, deg

INTRODUCTION

Previous Boeing-Vertol advanced transmission design studies established the need to advance the technology of tapered roller bearings. These studies revealed that the current state of the art of ball and cylindrical roller bearing systems for reacting combined radial and thrust loads will impose severe restrictions (such as reduced system life, increased weight, decreased reliability and limited design flexibility) when used in an advanced helicopter drive system. In contrast, the utilization of tapered roller bearings for reaction of combined loads produced by high-speed spiral bevel gears in helicopter transmission systems offers distinct advantages. Their use can reduce the number of bearings in the system, lower system weight, lower cost, improve operating efficiency, and provide more design flexibility.

In the past, transmission designers and bearing engineers were misguided by archaic ideas concerning the ability of tapered roller bearings to operate at speeds greater than 5000 fpm cone-rib (flange) velocity. However, prior Boeing-Vertol independent research and development programs (CY 1967-1970), in conjunction with the Timken Company, have demonstrated that tapered roller bearings can operate successfully at speeds four times greater than that (20,000 fpm). To attain these speeds, new developments and advanced theories had to be incorporated in the bearing design.

It has long been recognized that tapered roller bearings had the potential to carry heavier radial and thrust loads per pound than any other type of bearing. However, due to lubricant starvation at the roller-end/cone rib (inner race flange) contact caused by centrifugal force deflecting the oil-flow path away from this critical area, the standard tapered roller bearing has been limited to a top speed of approximately 10,000 fpm cone-rib velocity. The prior Boeing-Vertol independent research established the design features to achieve high-speed operation. They include an advanced lubrication system that will provide oil to the critical roller-end/cone-rib contact area and improved roller-end/cone-rib geometry to kinematically develop an adequate oil film thickness.

The objective of the work under this contract was to determine the influence of various design factors on bearing performance. The design factors included oil-flow rate, roller-end/cone-rib geometry, cage design configurations, cage plating, roller-end and cone-rib finish, and fail-safe bearing designs.

1

PREVIOUS BOEING-VERTOL RESEARCH

In 1968, The Boeing Company's Vertol Division sponsored a tapered roller bearing research program with The Timken Company as subcontractor. The objective of this program was to develop high-speed tapered roller bearings to support spiral bevel gearing in advanced helicopter transmissions and drive systems. A number of transmission studies which were conducted by Boeing-Vertol prior to that time revealed that high-speed (over 10,000 fpm) tapered roller bearings offered the most potential for increased load capacity and bearing life, and a corresponding reduction in bearing size and weight, when compared to a system of ball and cylindrical roller bearings.

One such design study was made on Boeing's CH-47C engine nose transmission. The standard design is shown in Figure 1. The goal of this study was to increase the single-engine power from 2200 horsepower to 3750 horsepower and provide a growth potential to 4500 horsepower within the same envelope size. One facet of the study revealed five basic requirements for the bearing system in order to achieve this goal:

- Reduce centrifugal force on rolling elements

- Reduce number of bearings in system

- Reduce internal heat generation

- Increase system stiffness

- Increase operating efficiency

The standard engine nose transmission was redesigned by incorporating four tapered roller bearings in place of the two ball and four roller bearings. A detailed analysis of the advanced tapered roller system design (as compared to the standard design) revealed a 5-pound weight savings, a 33-percent increase in system reliability, a 20-percent reduction in friction power loss and a fourfold improvement in radial stiffness. Figure 2 shows the advanced design, and Table I shows its advantages over the standard design.

LUBRICATION PROBLEM AT HIGH SPEED

Designers have known for a long time that tapered roller bearings have the potential to carry heavier radial and thrust loads per pound of weight than any other type of bearing. However, helicopter transmission designers have not considered them for advanced applications because they have had a top speed limitation of approximately 10,000 fpm cone-rib velocity (π x cone-rib diameter in feet x cone speed in rpm). The speed

2
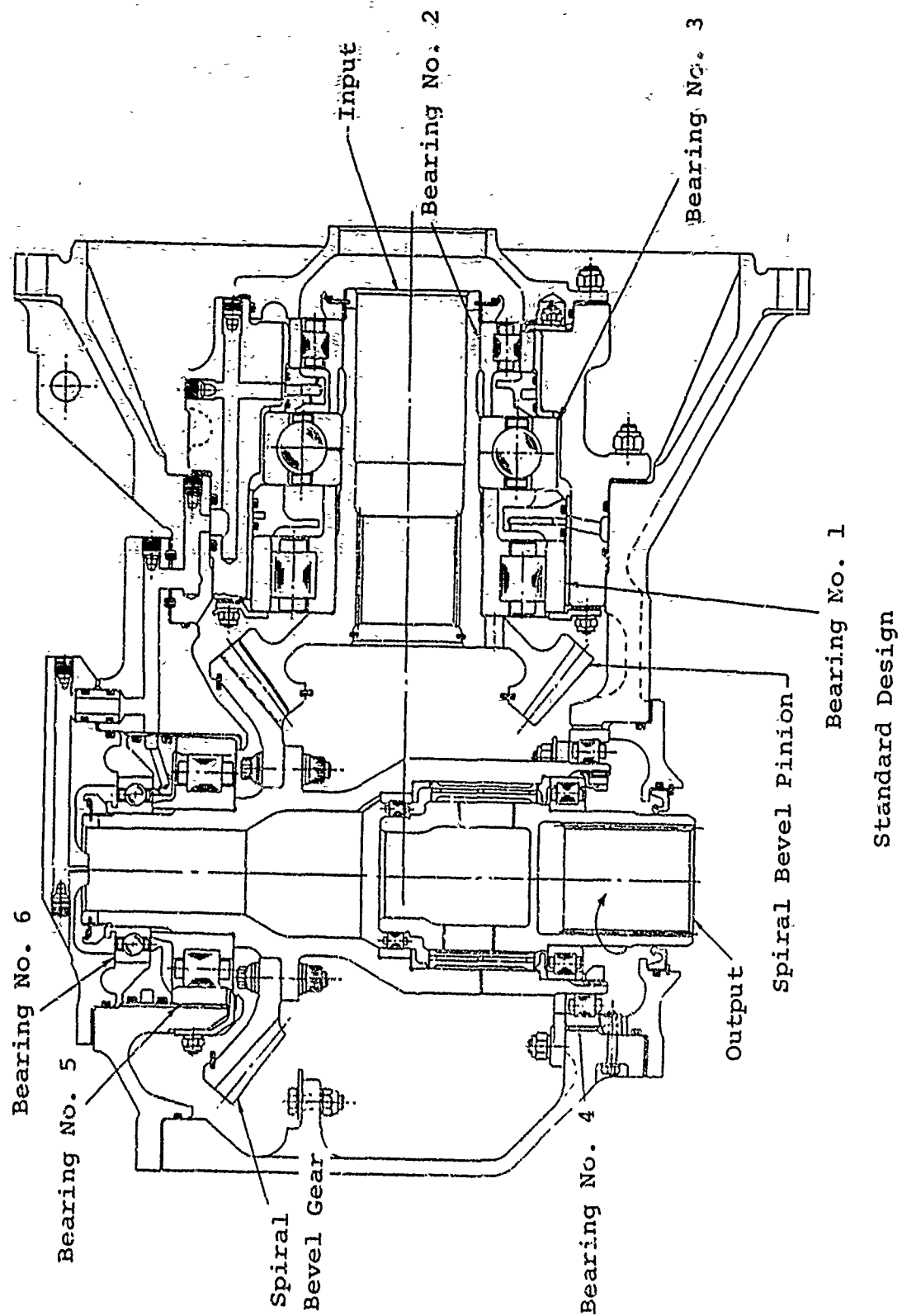
Figure 1. Typical Turboshaft Engine Transmission.

Standard Design

3

Input

Bearing
No. 1

Bearing No. 2

Spiral Bevel Pinion

Output

Bearing No. 4

Spiral
Bevel
Gear

Bearing No. 3
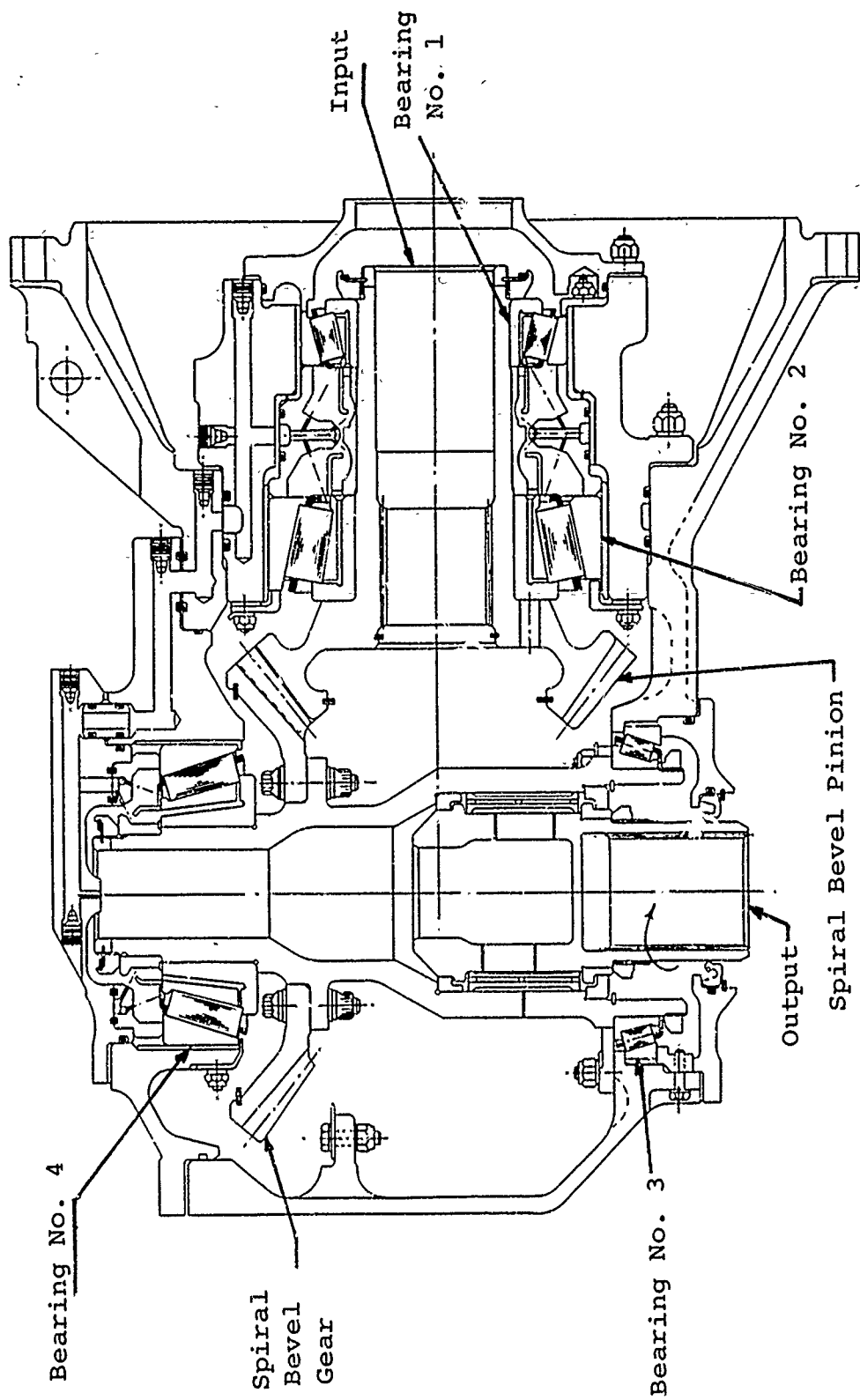
Figure 2. Modified Turboshaft Engine Transmission Tapered Roller Design.

4

TABLE I.	COMPARATIVE DESIGN STUDY OF BALL/ROLLER BEARING VERSUS TAPERED ROLLER BEARING	
	Current Technology	Advanced Technology
Configuration	SK20308	SK20548
Number of Bearings	2 Ball and 4 Roller	4 Tapered Roller
Bearing Weight	26 lb	21 lb
System Reliability	Baseline	33% Increase
Friction Losses	Baseline	20% Reduction
System Stiffness		
Axial $- K_X$ (lb/in.)	2.12×10^6	2.66×10^6
Radial $- K_Z$ (lb/in.)	2.07×10^6	8.02×10^6
Moment $- K_\theta$ (lb-in./rad)	3.73×10^7	8.25×10^7

limitation was imposed to prevent damage to the roller
spherical-end and cone rib (inner race flange) because cen-
trifugal force begins to cause lubricant starvation at this
speed.

Under a prior Boeing-Vertol Independent Research and Develop-
ment (IR&D) program, strobe lights and high-speed motion
picture film were used to isolate the problem areas in the
tapered roller bearing where lubricant starvation is a key
factor. The strobe-light photographs in Figure 3 show that,
as the speed increases, centrifugal force deflects the oil
flow path through the bearing further and further outward
until there is no lubricant at the critical contact area be-
tween the roller large end and cone rib.

At low speeds, some oil leaves the bearing between the cone
rib outside diameter (OD) and cage and some between the cage
and inside diameter (ID) of the cup. With increased speed,
the amount of oil leaving the bearing between the cone rib OD
and cage diminishes until there is almost none at a cone speed
of 7000 rpm.

This phenomenon is shown in Figure 4, where the oil flow path
is bent outward by centrifugal force as it progresses from the
small end of the bearing to the large end.

Test results indicated that if more oil than an optimum quan-
tity is forced through the bearing, churning results along
with the development of excessive heat.

APPROACHES TO SOLUTION OF THE PROBLEM

Prior Boeing-Vertol investigation indicated that, at high
speeds, the roller-end/cone-rib contact becomes the most
critical area. This contact between the roller end and cone
rib is one of pure sliding, and must be designed to entrap oil
and to continually replenish the oil film in the contact area.
To accomplish this, the large roller end is normally made
spherical and the cone rib is made in the shape of the inside
of a cone whose apex is on the cone centerline toward the
outside face on the large end of the cone. The roller
spherical-end radius is made smaller than the roller apex
length so that under no load the contact with the cone rib is
a point contact. The prior work also indicated that the cone
flange angle should be designed so that this contact point is
located at the mid-point of the available contact area as de-
scribed by the roller recess and the cone undercut.

This design will provide a wedge-shaped opening in all direc-
tions from the contact point to entrap lubricant as the roller
rolls relative to the cone rib. However, this contact point

6
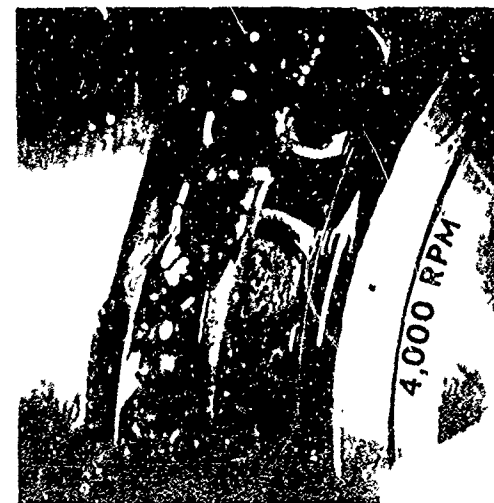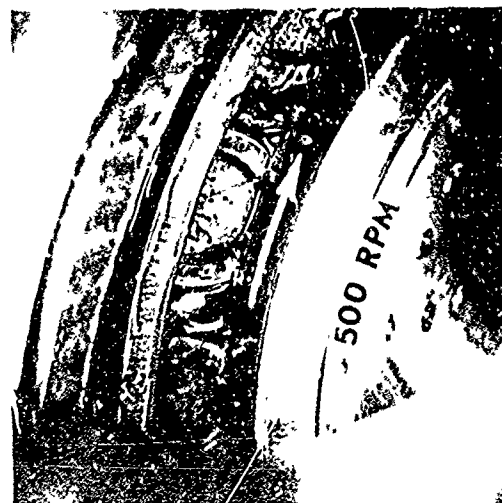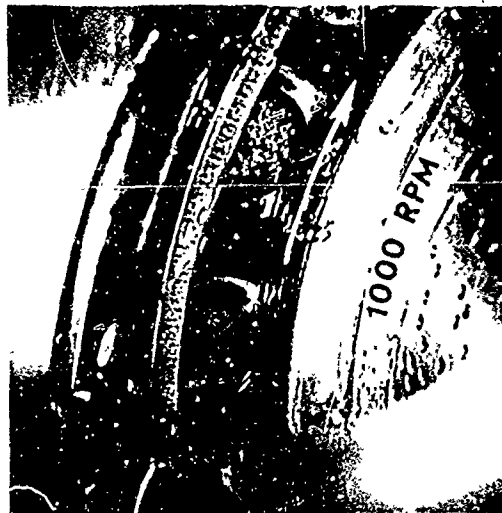
Figure 3. Centrifugal Force Effect on Oil Flow Path. Oil Flow of 6 Pts/ Min Through a 6500-Series Bearing (Lube at Small End Only).

7
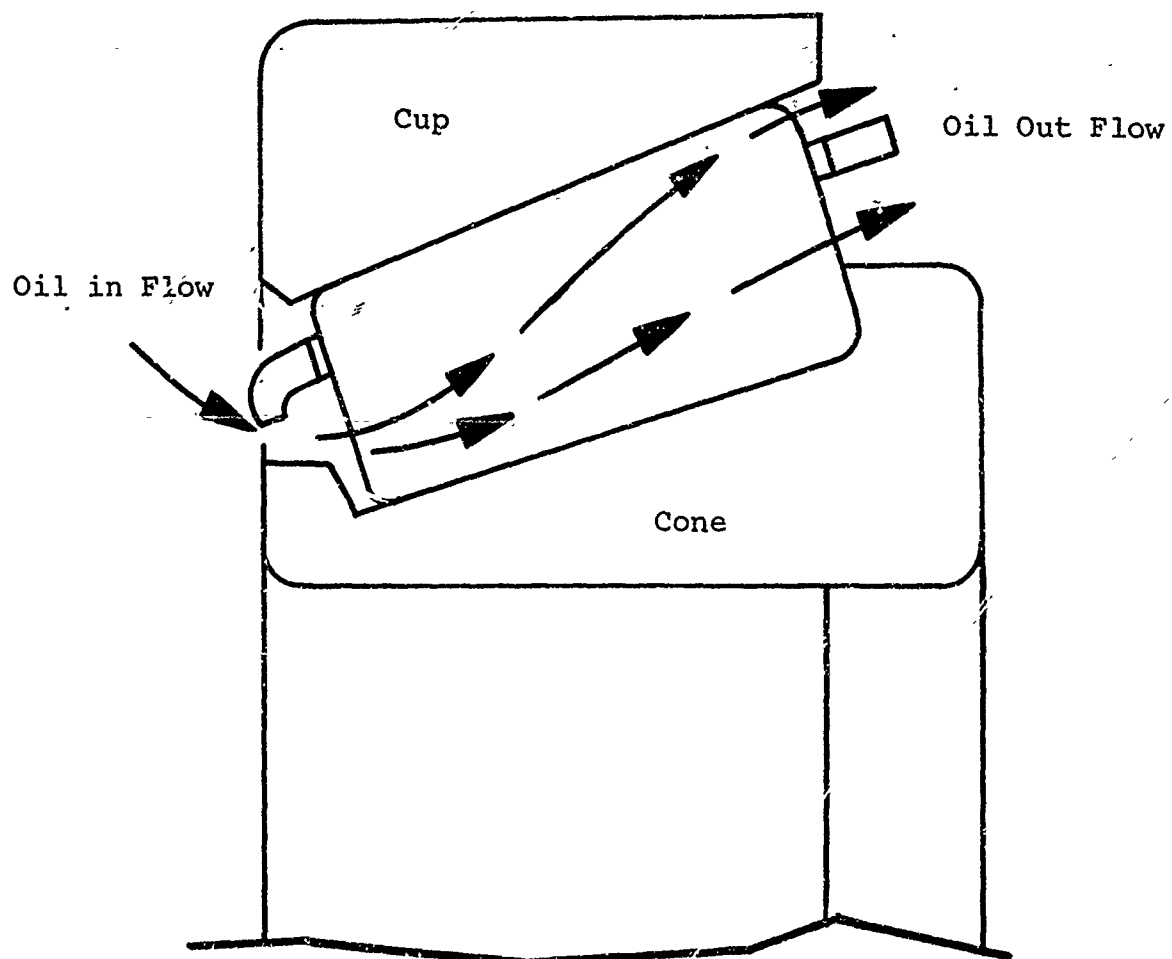
Figure 4. Normal Flow of Lubricating Oil Through
           Standard Bearing.

spreads into the form of an ellipse as load is applied to the
bearing. If the roller spherical-end radius is too large,
this ellipse of contact may be larger than the available con-
tact area, thus truncating the contact ellipse; and instead of
entrapping oil, the roller will scrap away oil.

The test results indicated that, as the bearing runs faster,
the wedge opening has to be increased to entrap sufficient oil
to replenish the oil film at the contact. Too small a roller
spherical-end radius will create higher stresses than the oil
film can support. Therefore, the roller-end/cone-rib geometry
is a very critical part of the bearing design.

Supplying sufficient lubricating oil to the roller-end/cone-
rib contact is an even more critical problem to high-speed
operation than the geometry of these surfaces, since
centrifugal force starves this area.

Under the Boeing-Vertol/Timken IR&D program, 134 test bearings
of the 6500 series (3.50-inch bore) were tested and evaluated.
The testing sequence which was used for this program is shown
in Figure 5 . The test program covered modifications to the
bearing geometry, cage design, and lubrication system.

The conclusions from the test results were that tapered roller
bearings can be successfully operated at high loads and
speeds. The test program demonstrated loads of 7500 pounds
radial and 4350 pounds thrust up to a speed of 16,000 rpm
(20,000 fpm cone-rib velocity). The test results also iden-
tified the need to optimize various parameters and develop an
understanding of the interactions of these parameters on
performance.

9

134 Test Bearings Fabricated

Standard Baseline Bearings
(Selected for Runout, Finish, and Cage Shake)
Test Variables:
- Shaft Speed
- Load
- Oil Flow Rate

80% Spherical Roller End Radius

95% Spherical Roller End Radius

Run-In with Special Fluid

Test Results Evaluated
Need for Curved Oil Dam Determined
80% Spherical End Radius Selected

Curved Oil Dam Initial Configuration Evaluated with Modifications

Cone

Cup

Roller

Oil Flow

Cage

Relief Holes with Oil Jet Large End

Relief Holes with Bearing Run-In

Relief Holes in Dam

Test Results Evaluated
Additional Configurations Required

11

Cone

Cage Oil Roller

Relief Holes with Oil Jet Large End

Relief holes with Bearing Run-In

Relief Holes in Dam

Test Results Evaluated Additional Configurations Required

Curved Oil Dam Welded to Cage

Curved Oil Dam with Scallops and Vortex Guides

Curved Oil Dam with Scallops

Test Results Evaluated Need for Oil Guides in Cage Determined

Oil Flow

Internal Annulus and Oil Tube Guides
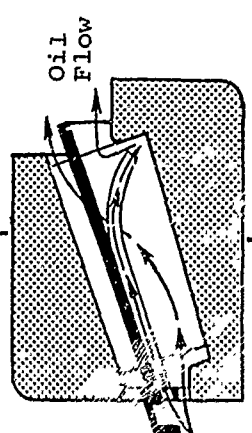
External Annulus and Oil Tube Guides

Test Results Evaluated Need for Alternate Lube Method Determined

Alternate Lube Source Through Holes in Cone (Inner Race) Evaluated
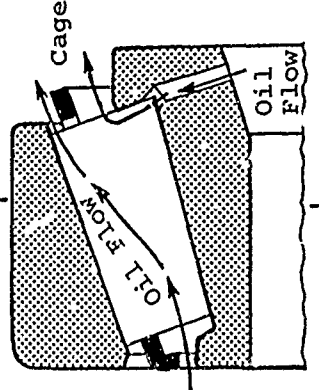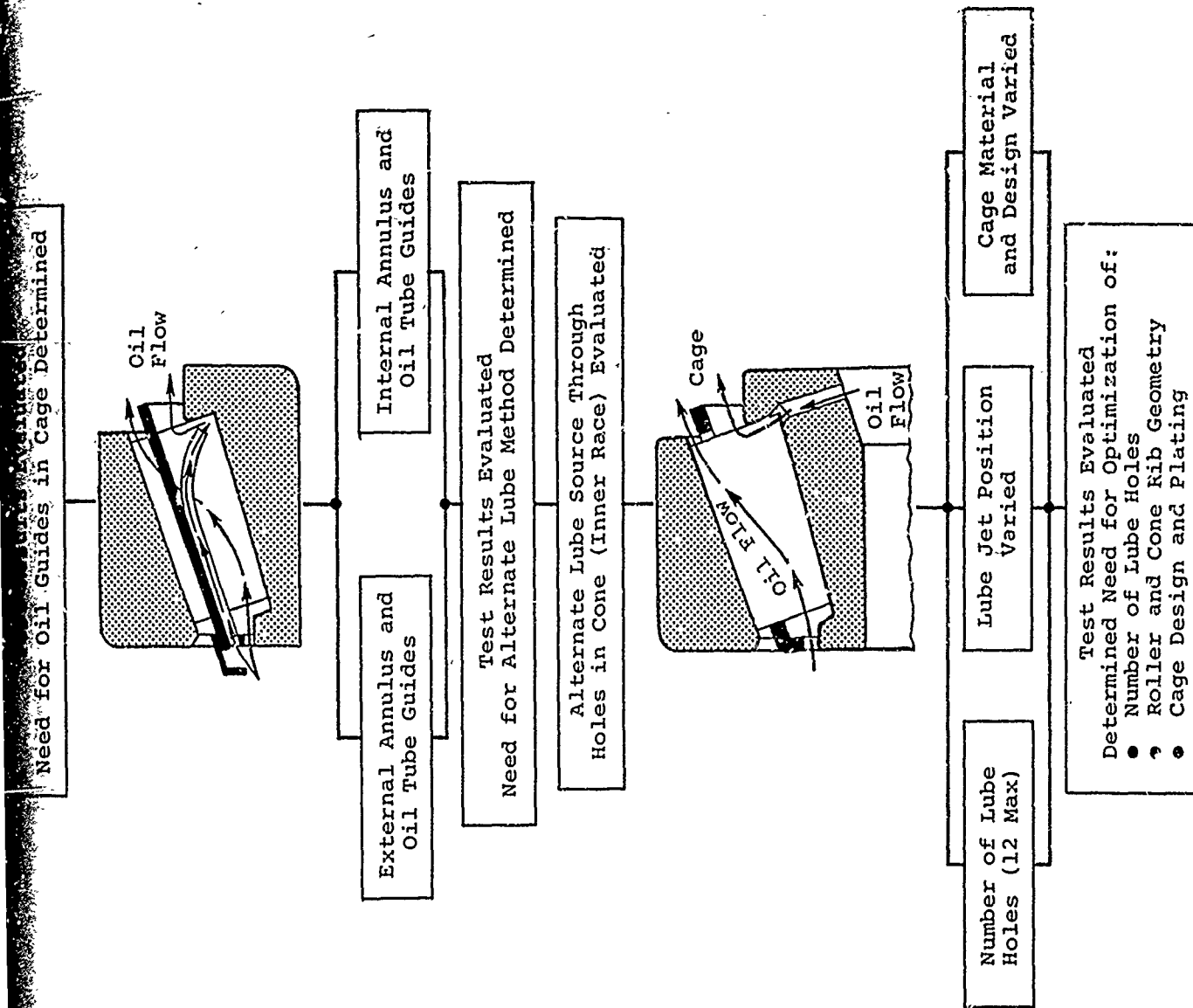
Cage

Oil Flow

Figure 5. Boeing-Vertol/Timken Independent Research and Development Tapered Roller Bearing Program.
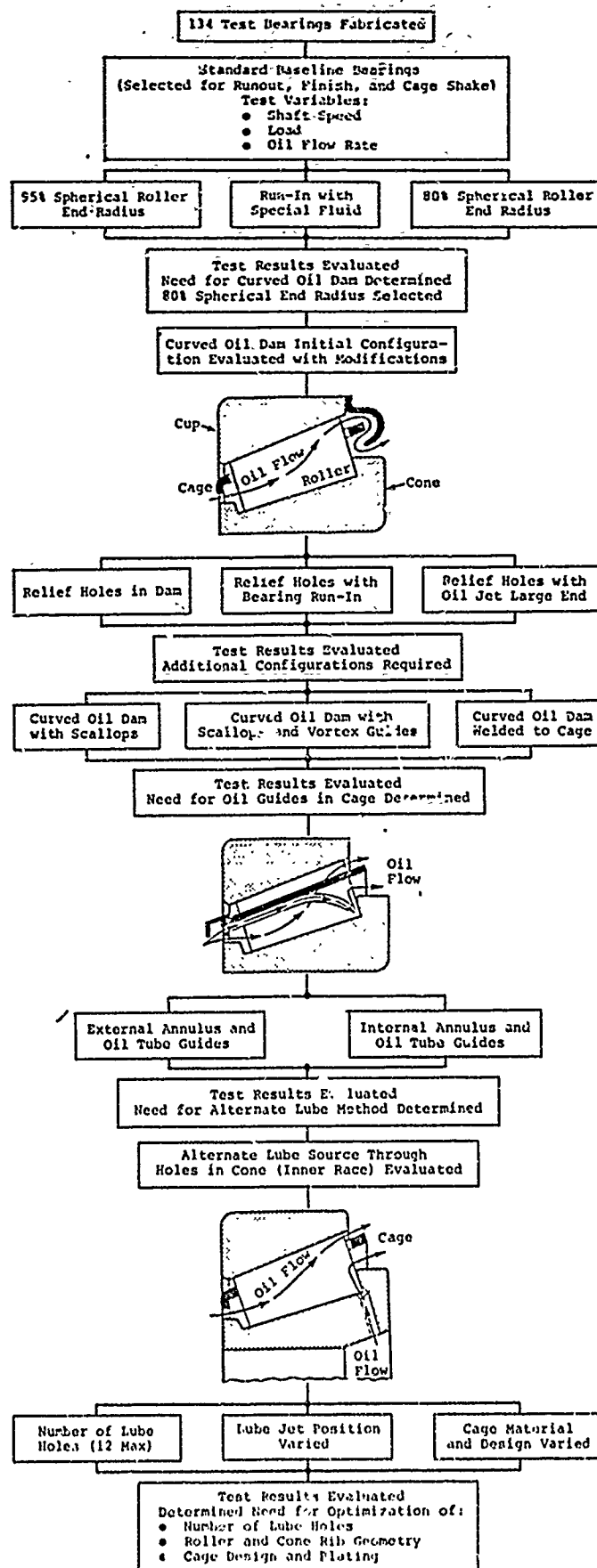
Figure 5. Boeing-Vertol/Timken Independent Research and Development Tapered Roller Bearing Program.

ANALYTICAL INVESTIGATION

In order to develop an understanding of the operating and performance characteristics of high-speed, tapered roller bearings, a two-phase program was conducted to evaluate and optimize a 6500-series, tapered roller bearing. The first phase of this program was the development of a theoretical analysis to provide the analytical tools necessary for predicting and evaluating the performance of high-speed, tapered roller bearings. The second phase was an experimental investigation to provide test data to substantiate the analytical investigation.

The analytical investigation was conducted to develop equations and methodology which could help evaluate the influence of critical bearing parameters on the performance of high-speed, tapered-roller spiral bevel gear support bearings. The analytical investigation was directed toward evaluating the kinematic relationships, speed/load effects, cone rib flange contact analysis, oil film thickness at contacting interfaces and fatigue life of a tapered roller bearing. For the complete detailed analysis and development of the equations, refer to the appendix. The following is a summary of the work completed in the analytical investigation.

DEVELOPMENT OF INTERNAL GEOMETRY OF TAPERED ROLLER BEARINGS

The appendix describes the basic principles of the tapered roller bearing and defines several geometry relationships which are used in later portions of the ana is. The principle of the tapered roller bearing consists constructing the rolling elements and raceways so that the ape s of the tapered surfaces meet on a common axis. This construction insures true rolling motion on the raceways and also provides the capability of reacting combined radial and thrust loading which must be reacted in supporting spiral bevel gears. The only contact area that does not have rolling action is the roller-end/flange contact. The equations shown in the appendix help to define the geometric relationships of a tapered roller bearing.

ROLLING ELEMENT KINEMATIC ANALYSIS

The kinematic relationships of a tapered roller bearing are very important in understanding the velocities and motions which help determine other parameters such as oil film thickness, fatigue life and speed effects. The kinematic analysis developed in this program neglected EHD and sliding effects and assumed sufficient applied load to insure pure rolling

13 **Preceding page blank**

motion on the raceways. The equations were developed for cage speed, angular velocities of the rolling element, linear and sliding velocity of the flange at the roller-end contact and the entraining velocities of the roller-end/flange and raceway. These equations were developed for the cases of both inner and outer race rotation and the flange located on either the cone or cup. The kinematic relationships developed are shown in the appendix.

ROLLING ELEMENT LOAD ANALYSIS

A load analysis was conducted on a single roller. The goal of the analysis was to understand the loads such as centrifugal force, gyroscopic moment, raceway load and flange reaction load which were reacted by a single roller. The most critical load reaction point of a roller is at the cone rib flange. In order to predict the contact stress and oil film thickness, it is essential to know how the roller loads are reacted in the cone rib flange area. In addition to the roller load reaction, the development of an equation to predict the declutching thrust is provided in the appendix. Declutching thrust is essential to establish a minimum load requirement necessary to keep the cup and cone assembly from separating axially due to the roller centrifugal force.

LUBRICANT FILM THICKNESS ANALYSIS

The roller-end cone/flange contact area is the most critical contact zone in a high-speed, tapered roller bearing. The contact is pure sliding between the roller end and cone flange and the geometry of this contact must be optimized to provide an adequate oil film thickness which would preclude metal-to-metal contact. Analyses were conducted to establish the relationship and effects of various parameters such as load, entraining velocity, contact curvature radii and lubricant viscosity on the generation of an oil film. Included in the appendix are the equations for determining the oil film thickness at both the cup and cone roller contact.

CONE RIB (FLANGE) CONTACT STRESS

In addition to being a very critical area for oil film generation, the roller-end cone/flange contact must also be analyzed for contact stress. Under no load, the contact of the roller end and cone rib flange is a point; however, under load the contact point spreads out elliptically. Accurate predictions of contact area size and the stress and location of the contact area on the flange are critical. The contact area can be drastically changed by variation of the roller-end

14

spherical radius and the flange angle. The equation necessary to calculate the dimensions of the contact ellipse, deflection of the contact point and the maximum compressive stress is given in the appendix.

CONE RIB SCORING ANALYSIS

The predominant mode of failure of high-speed, tapered roller bearings is scoring at the roller-end/flange contact. Scoring failure is the momentary welding, tearing apart and smearing of the contact surfaces due to a breakdown of the lubricant film. This breakdown can be the result of either insufficient oil supply or excessive heat generated by the pressure and sliding in the contact area. This mode of failure is very similar to scoring experienced in heavily loaded, high speed gears. Therefore, the flash temperature theory was applied to the analysis of the roller-end/flange contact zone. An analysis was developed based on the theory of what determined the temperature rise in the contact zone. Several assumptions were made to calculate the flash temperature. Details of the assumptions and analysis are included in the appendix.

CONE RIB LUBRICANT TRAJECTORY ANALYSIS

As the speed of a tapered roller bearing increases, the effect of centrifugal force on the oil passing through the bearing makes it very difficult to maintain an adequate supply of oil at the roller-end cone/flange contact. High speed photographs have shown oil starvation in this area when speeds exceed 10,000 fpm. In order to insure an adequate supply of oil, a secondary source of lubricant through radial holes in the cone at the flang undercut has been evaluated and proved to reduce the hazard c coring. Testing has shown that the number of holes and design of the hole arrangement have a significant influence on the operation of high speed bearings. An analysis was developed which provides a method for predicting the trajectory of the oil stream leaving the lube holes, the velocity of the oil, and area of the flange covered by each oil stream.

The analysis established a ratio of the angular spacing of the radial lubrication holes to the angular coverage of the oil stream on the cone-rib flange surface. This ratio can be used to evaluate the effectiveness of the second lube source to provide adequate lubrication to the roller-end/flange contact. Details of the analysis are presented in the appendix.

15

BEARING FATIGUE LIFE ANALYSIS

The data presented in the appendix include the equations
necessary to establish a system analysis of high-speed,
tapered roller bearings. These equations can be incorporated
into a bearing computer program and therefore will provide the
means to determine the applied load of a system of bearings
and also determine the internal load distribtuion for each
bearing. Methods for incorporating shaft flexibility and
initial displacement of bearing rings are included in this
analysis. Fatigue life is calculated in accordance with the
Lundberg-Palmgren statistical theory of rolling-element bear-
ing fatigue. The lines of the outer and inner contacts are
evaluated separately and then statistically combined to give
the life of the complete bearing.

EXPERIMENTAL INVESTIGATION

TEST SPECIMEN DESCRIPTION

Test Specimen Bearings

Thirty-six 6500-series bearings were fabricated to Timken Modified Code 436 (see Figure 6).

- Cone Bore - 3.500 Inches

- Outside Diameter - 6.375 Inches

- Width - 2.170 Inches

Twenty-four of these bearings were tested with eighteen 0.052-inch-diameter holes through the large rib undercut to the backface chamfer oil manifold (see Figure 7).

Twelve bearings were tested with twenty-four 0.043-inch-diameter holes through the large rib undercut to the backface chamfer oil manifold (see Figure 8).

Additional modifications to these bearings are listed in Table II.

The silver plating used in this program to plate the cages was applied according to Federal Specification QQ-S-365a. The plating is Type II Grade B with a matte finish. The first 4 bearing cages were processed with a tin strike before silver plating to a 0.001-inch thickness. The remaining cages were processed with a nickel strike and a silver strike before silver plating to a 0.001-inch to 0.002-inch thickness.

Four bearing cages were brass plated. The brass plating was a 70-percent copper, 30-percent zinc solution processed until a plating from 0.001-inch to 0.002-inch thick was obtained.

Figures 9 through 12 are photographs of typical new bearing configurations. Figure 13 is an example of cage flaring.

Fail-Safe Test Specimen Bearings

Four 6500-series bearings were modified with various fail-safe materials to evaluate their performance under lubricating oil-on and oil-off conditions. Table III describes the fail-safe bearings that were tested. Figures 14 through 16 are assembly drawings of these bearings. These bearings were tested with machined race/guided centerline-contact cages.

17

2.1290
2.1250
1.6895
1.6775

0.13 R

0.4375 Nom

6.3760 Dia
6.3750

4.322 Min

4.100 Max

22° 43'

2.1703
2.1683

3.5000 Dia
3.5010

3.780

4.922 Max

5.937 Max

29° 53'

0.51

0.50

0.165
0.140

0.035 R

0.035 R

0.186
0.140
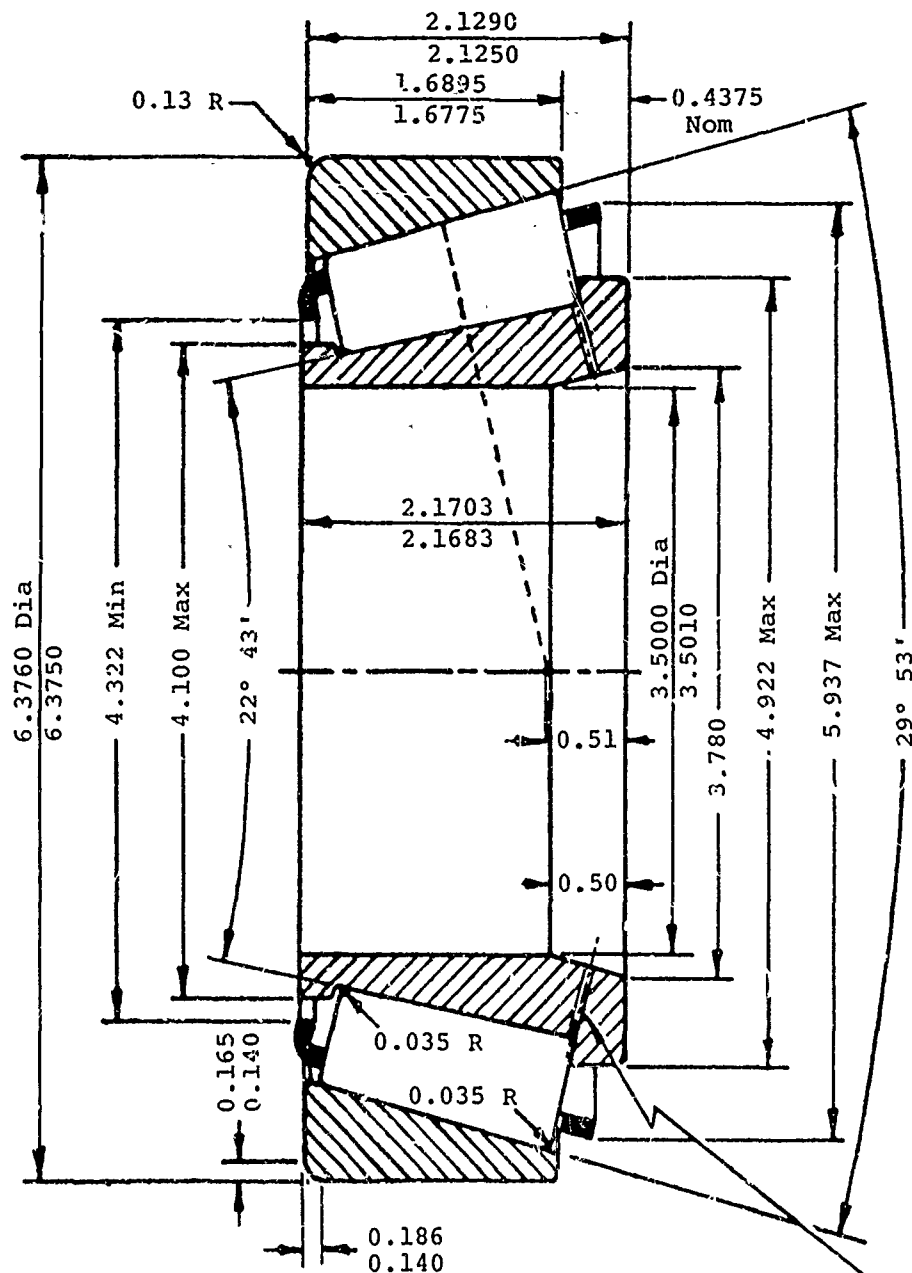
18 Holes, 0.052 in. Dia, or 24 Holes, 0.043 in. Dia, equally spaced, perpendicular to chamfer, opening into large end grinding relief

Basic Rating @ 500 RPM
Radial   16,000 Lb
Thrust   11,000 Lb
Dimensions are given in inches

Cone P/N
1. Materi
2. Rolli
3. 100%
    burns
4. Race
5. Class
6. Bare
    defec
7. All c
8. Rolle
    flat
    beari

Cup P/N
1. Mater
2. Rolli
3. 100%
    burns
4. Race
5. Class
6. Cup 1
    No de
7. All c

Rollers
1. Mater
2. Rolli
3. Rolle
4. Sample
    grind
5. Rolle
6. Rolle
7. Rolle
    defec
8. Rolle
    Rolle

Cage P/N
1. Mater
2. 100%
3. Cage,
    close
4. Cage
    shot
    wingi
    preve

Figure 6. Test Specimen Bearings per Timken Modified Code 436.

19

Preceding page blank

0.4375
Nom

3.5000 Dia
3.5010

3.780

4.922 Max

5.937 Max

29° 53'

0.51

0.50

R

24 Holes, 0.043 in. Dia,
ar to chamfer, opening
ief

ic Rating @ 500 RPM
Radial   16,000 Lb
Thrust   11,000 Lb
nensions are given in inches

en Bearings per Timken

19

Preceding page blank

Cone P/N 6580

1. Material: Consumable Electrode Vacuum Melt Electric Furnace Modified SAE 4620 Steel.
2. Rolling contact surface hardness 58 to 63 Rockwell C.
3. 100% Standard double etch all over to detect grinding burns.
4. Race to be honed to 8 microinches.
5. Class and Code No. 7-227 to be etched on the part.
6. Bare cone 100% visual inspected for undesirable surface defects – No defects allowed.
7. All cones checked for minimum hardness on either face.
8. Roller spherical end contact with cone large rib face flat – middle contact (must be blue checked on every bearing).

Cup P/N 6535

1. Material: Consumable Electrode Vacuum Melt Electric Furnace Modified SAE 4620 Steel.
2. Rolling contact surface hardness 58 to 63 Rockwell C.
3. 100% Standard double etch all over to detect grinding burns.
4. Race to be honed to 8 microinches.
5. Class and Code No. 2-436 to be etched on the part.
6. Cup 100% visual inspected for undesirable surface defects – No defects allowed.
7. All cups checked for minimum hardness on either face.

Rollers P/N 6003 (19 per Cone)

1. Material: Consumable Electrode Vacuum Melt Electric Furnace Modified SAE 4620 Steel.
2. Rolling contact surface hardness 58 to 63 Rockwell C.
3. Roller radii tumble polished after grinding.
4. Sample lots to be standard double etched to detect grinding burns – Samples to be scrapped.
5. Roller body crowned radius 400 to 600 inches.
6. Roller body honed to 8 microinches.
7. Rollers 100% visual inspected for undesirable surface defects – No defects allowed.
8. Roller spherical end radius – 75% to 80% of apex length. Roller spherical end finish – 6 microinches maximum.

Cage P/N 6512

1. Material: HRLC Steel Deep Drawing Quality P & O.
2. 100% Visual inspected for defects.
3. Cage, cone, and rollers to be nonseparable after cage is closed in.
4. Cage modification – Vapor blast cage to clean rather than shot blasting or tumbling to preserve finish obtained in winging (coining) operation. Use special handling to prevent distortion or nicking damage to cage.

20
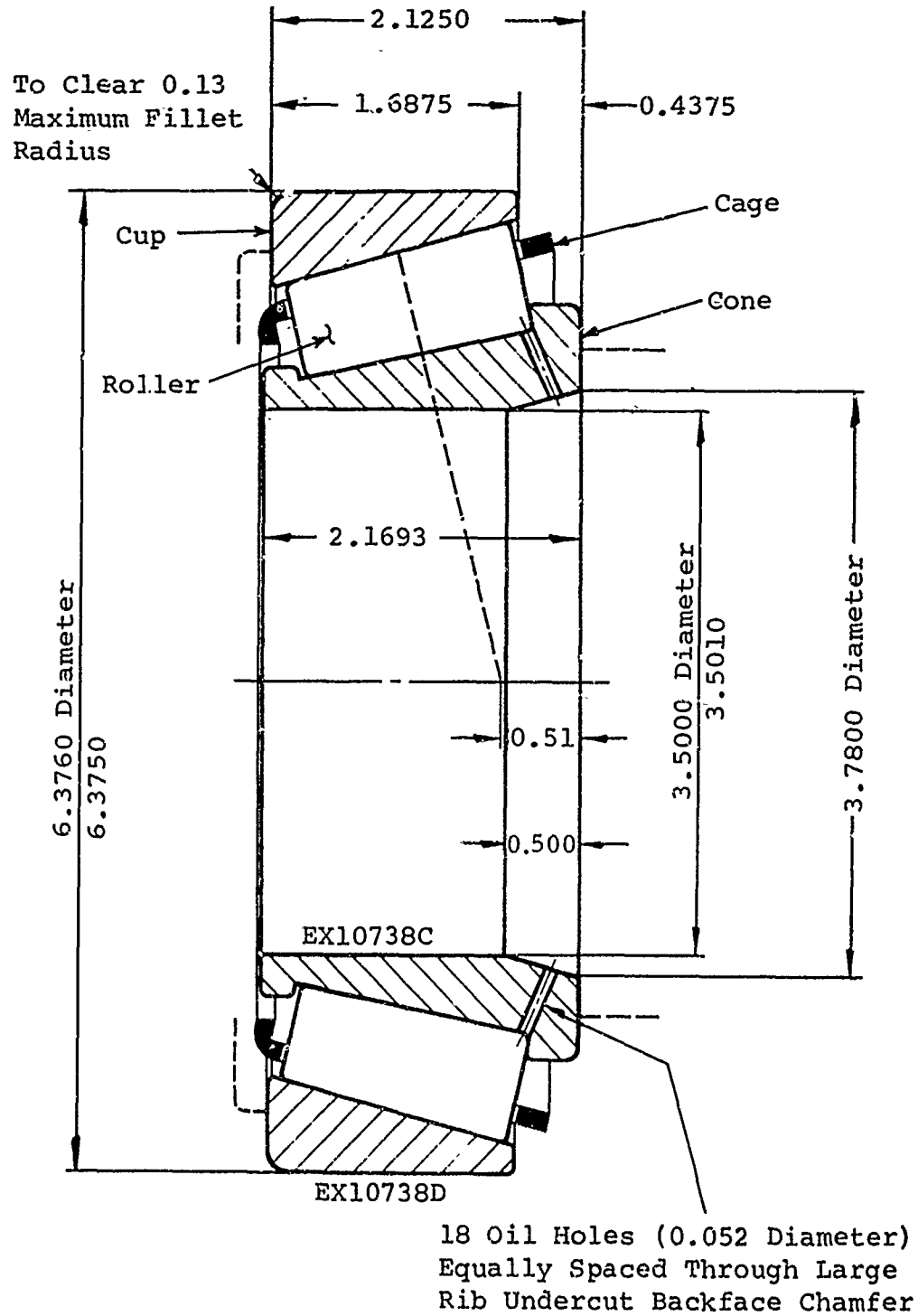
Figure 7. Test Bearing Design With 18 Oil Holes.

21
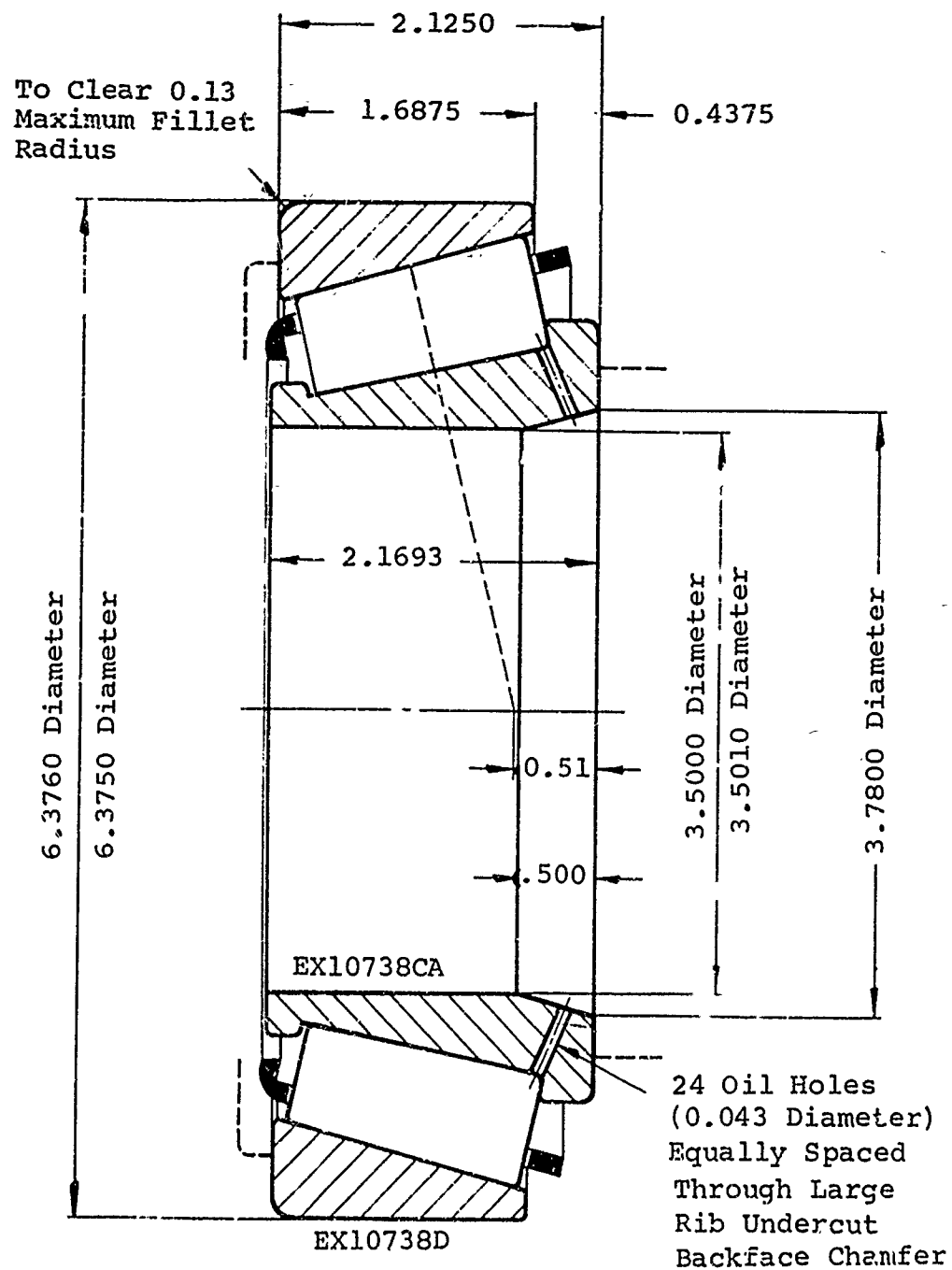
Figure 8.   Test Bearing Design With 24 Oil Holes.

TABLE II. HIGH-SPEED SPIRAL BEVEL SUPPORT TAPERED ROLLER BEARING PROGRAM

Bearing Number(1)	Test Number	Roller Spherical End Radius % Apex	Cage Finish	Number of Radial Holes Through Cone	Oil Flow Rate Pints/Minute Large End/ Small End	Level-Off Temperatures (°F) Bearing Cup Drive End/ Opposite Drive End	Outlet Oil	Housing Surface	Torque (Lb-In.) Total of Four Bearings	Remarks
1 & 2	1	80	Phosphate	18	4/4	273/263	209	215	154	OK
					4/3	282/269	209	222	149	OK
					4/2	280/266	212	210	137	OK
					4/1	277/272	217	230	128	OK
					4/0	300+/298	263	233	118	OK (2-1/2 hour run)
3 & 4(2)	2	80	Phosphate	18	4/4	274/256	211	220	161	No. 3 damaged (1-1/2 hour run)
5 & 6	3	70	Phosphate	10	4/4	266/261	209	210	146	OK
					4/3	271/262	206	220	150	OK
					4/2	278/264	205	220	145	OK
					4/1	285/274	220	230	136	OK
					4/0	-	-	-	-	No. 5 damaged (5 minute run)
7 & 8	4	70	Phosphate	18	4/4	270/262	212	216	154	No. 8 damaged reducing oil flow to 2 pints/minute
9 & 10	5	60	Phosphate	18	4/4	-	-	-	-	No. 9 damaged (15,000 rpm)
11 & 12	6	60	Phosphate	18	4/4	-	-	-	-	No. 11 damaged (30 minute run)
13 & 14	7	80	Silver	18	4/4	262/258	202	215	153	OK
					4/3	274/268	209	213	150	OK
					4/2	282/274	213	213	146	OK
					4/1	280/276	220	225	140	OK
					4/0	288/300+	249	230	146	No. 14 damaged (15 minute run)
15 & 16	8	80	Silver	18	4/4	268/257	202	208	150	OK
					4/3	275/262	208	220	146	OK
					4/2	279/263	210	225	140	OK
					3/2	288/268	210	230	139	OK
					2/2	298/274	212	240	139	OK
					1/2	300+/282	210	240	130	OK

TABLE II. Continued

Bearing Number[1]	Test Number	Roller Spherical End Radius & Apex	Cage Finish	Number of Radial Holes Through Cone	Oil Flow Rate Pints/Minute Large End/Small End	Level-Off Temperatures (°F) Bearing Cup Drive End/Opposite Drive End	Outlet Oil	Housing Surface	Torque (Lb-In.) Total of Four Bearings	Remarks
17 & 18	9	80	Brass	18	4/4	-	-	-	-	No. 18 damaged[4] (11,000 rpm)
19 & 20	10	80	Brass[3]	18	4/4	-	-	-	-	No. 20 damaged[4] (11,000 rpm)
19A & 17A	Rerun 9-10	80	Brass	18	4/4	-	-	-	-	No. 17A damaged[4] (14,000 rpm)
X-DE & X-ODE	-	80	Phosphate[3]	18	4/4	270/260	208	218	153	OK
21 & 22	11	80	Silver	24	4/4	266/262	208	220	147	OK
					4/3	271/265	207	245	145	OK
					4/2	280/275	212	235	141	OK
					4/1	286/285	229	235	133	OK
					4/0	278/271	230	248	122	
24 & 23	12	80	Silver	24	4/4	262/252	206	210	148	OK
					4/3	264/252	204	215	147	OK
					4/2	272/259	208	228	144	OK
					3/2	282/266	212	232	140	OK
					2/2	294/270	209	235	139	OK
					2/1	300/271	222	248	130	OK
					2/0	300+/273	225	250	116	
31L & 25H[5]	13	80	Silver[3]	18	4/4	-	-	-	-	No. 25 damaged[4] (13,000 rpm)
31L & 25H	Rerun 13	80	Silver[3]	18	4/4	-	-	-	-	No. 25 damaged[4] (12,000 rpm)
25H & 31L	Rerun 13	80	Silver[3]	18	4/4	-	-	-	-	No. 31 damaged[4] (5,000 rpm)
25H & 31H	Rerun 13	80	Silver[3]	18	4/4	-	-	-	-	No. 25 damaged[4] (16,000 rpm)
X-DE & X-ODE	-	80	Phosphate[3]	18	4/4	262/254	206	210	147	OK
33 & 32	17	80	Silver[3]	18	4/6	250/244	204	205	160	OK
					4/4	260/256	203	212	150	OK
					4/3	266/255	200	220	144	OK
					4/2	267/254	200	222	139	OK
					3/2	277/262	203	225	130	OK
					2/2	288/268	205	235	128	OK
					2/1	292/267	204	240	120	OK
					2/0	289/264	208	245	108	

TABLE II. Continued

Bearing Number [1]	Test Number	Roller Spherical End Radius & Apex	Cage Finish	Number of Radial Holes Through Cone	Oil Flow Rate Pints/Minute Large End/Small End	Level-Off Temperatures (°F)			Torque (Lb-In.) Total of Four Bearings	Remarks
						Bearing Cup Drive End/Opposite Drive End	Outlet Oil	Housing Surface		
27 & 26	14	80	Silver(3)	24	4/2	262/260	205	210	138	OK after 24 hour test
29 & 28	15	80	Silver	24	4/2	270/260	205	225	138	OK after 24 hour test
					4/2	264/256(6)	202	232	137	OK after 80 percent load test
34 & 30	16	80	Silver	24	4/2	-	-	-	-	No. 30 damaged (15,000 rpm)
35 & 36	18	80	Silver(3)	24	4/2	264/264	200	200	138	OK after 24 hour test No. 36 damaged reducing load to 60 percent.
35 & 34	Rerun 16-18	80	See above	24	4/2	270/263	206	223	138	OK after 24 hour test

(1) First number—drive end bearing, second number—opposite drive end bearing

(2) Cages were spread before flaring distorting cage shape causing premature damage

(3) Cage not flared

(4) All opposite drive end bearings

(5) Range of rib angle: L = low end of range, H = high end of range
M = middle of range

(6) 80 percent of radial and thrust load

25
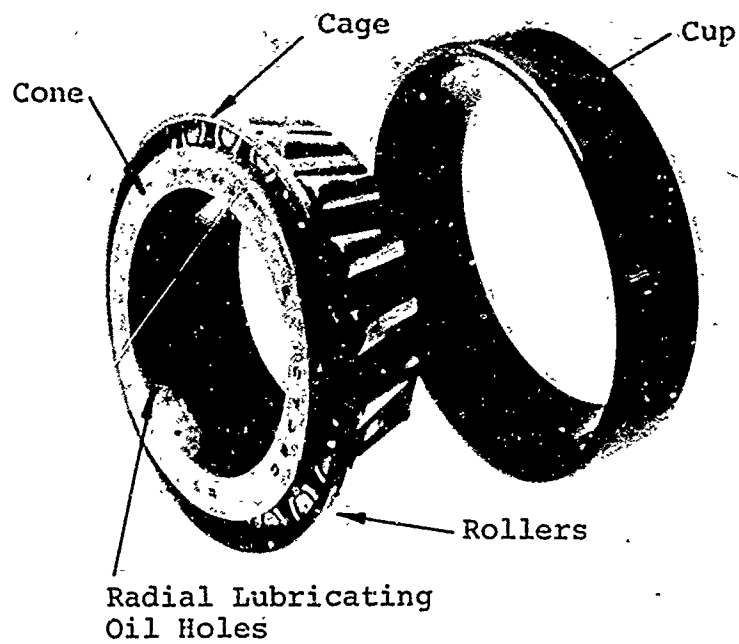
18 Radial Lubrication Holes
Roller Spherical End Radii - 80 Percent Apex Length
Cage - Phosphate-Coated Stamped Steel

Figure 9 .   Typical New Bearing.
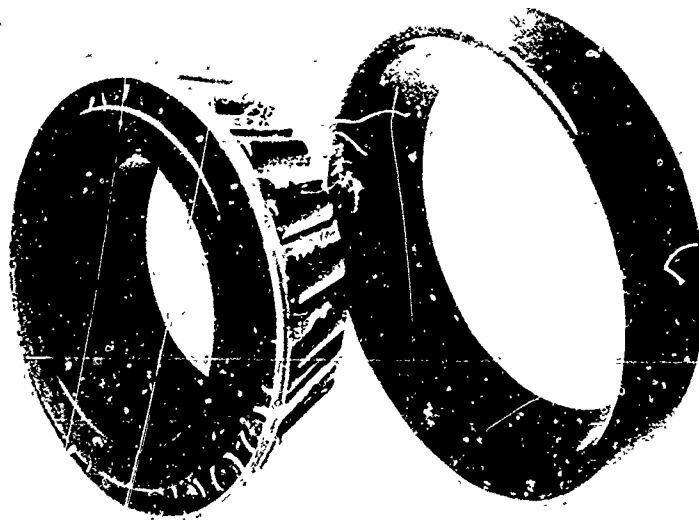
18 Radial Lubrication Holes
Roller Spherical End Radii - 80 Percent Apex Length
Cage - Silver-Plated Stamped Steel

Figure 10. Typical New Bearing.

27
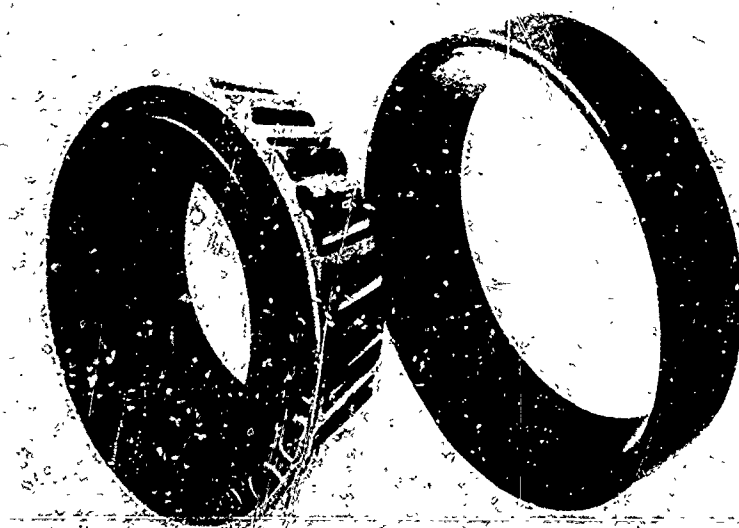
18 Radial Lubrication Holes
Roller Spherical End Radii - 80 Percent Apex Length
Cage - Brass-Plated Stamped Steel

Figure 11. Typical New Bearing.
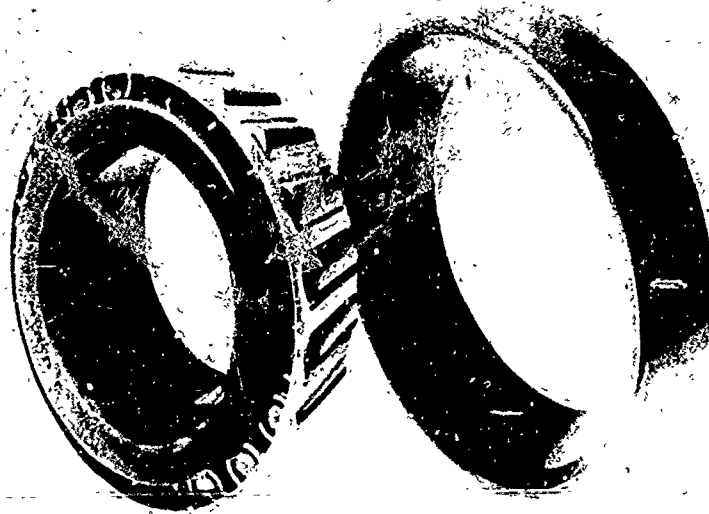
24 Radial Lubrication Holes
Roller Spherical End Radii - 80 Percent Apex Length
Cage - Silver-Plated Stamped Steel

Figure 12. Typical New Bearing.

Flared Cage to Relieve Roller
Body Contact Large End

Bend Cage At
This Point
After Winging
to Obtain
0.010 Minimum
Clearance Side
Between Roller
Large End and
Cage Bridge

0.810

Cage EX2052 AB

0.010
MIN
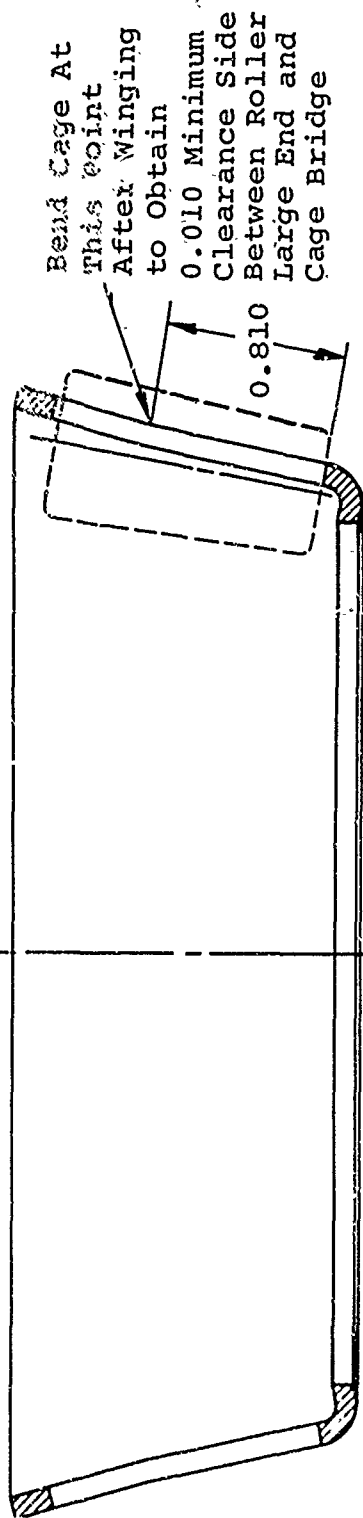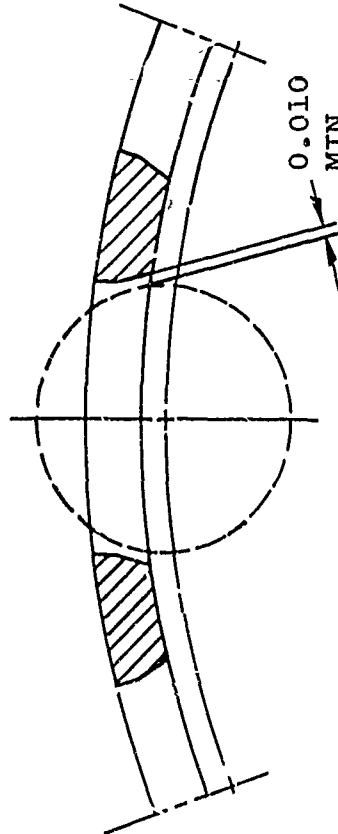
Section of Cage at Large End
of Pocket After Winging

Figure 13. Flared Cage Design to Relieve Body Contact at
Roller Large End.

30

TABLE III. SUMMARY OF FAIL-SAFE BEARING MODIFICATIONS, TESTS 19 AND 20

Bearing Number	Cone Rib	Roller	Cage (Race Guided Centerline Contact)
83031-37	Vespel SP-21* Insert Bonded and Mechanically Trapped at the Cone/Rib Interface (see Figure 14)	Standard	Silver Plated
83031-38	Same as Above	Standard	Borkote Treated
83031-39	T-400 Alloy** Ring High Temperature Brazed to Separable Cone/Rib Ring (see Figure 15)	Standard	Silver Plated
83031-40	Borkote Treated*** Separable Cone/Rib Ring (see Figure 16)	Spherical End Radius Borkote Treated	Borkote Treated

* Vespel SP-21 is made by the E. I. DuPont de Nemours and Company, Inc. It is a polyimide resin composite material containing 15 percent graphite by weight.

** T-400 alloy is made by the DuPont Company. It contains hard grains of an intermetallic compound of a Laves Phase structure dispersed in a softer matrix.

*** Borkote is a boronizing process developed by Atlantic Advanced Metals, Inc.
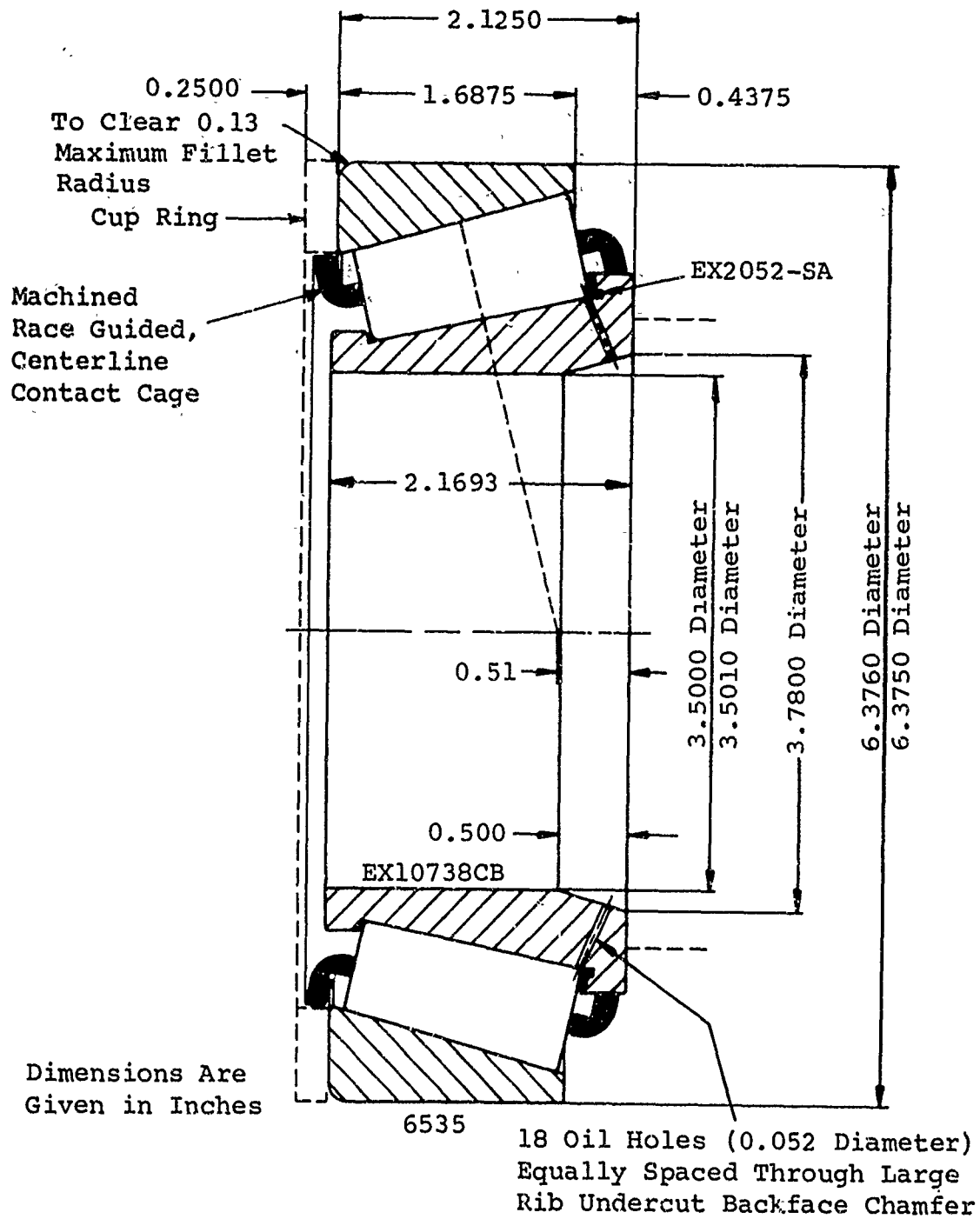
Figure 14. Fail-Safe Bearing Design With Rib Insert.
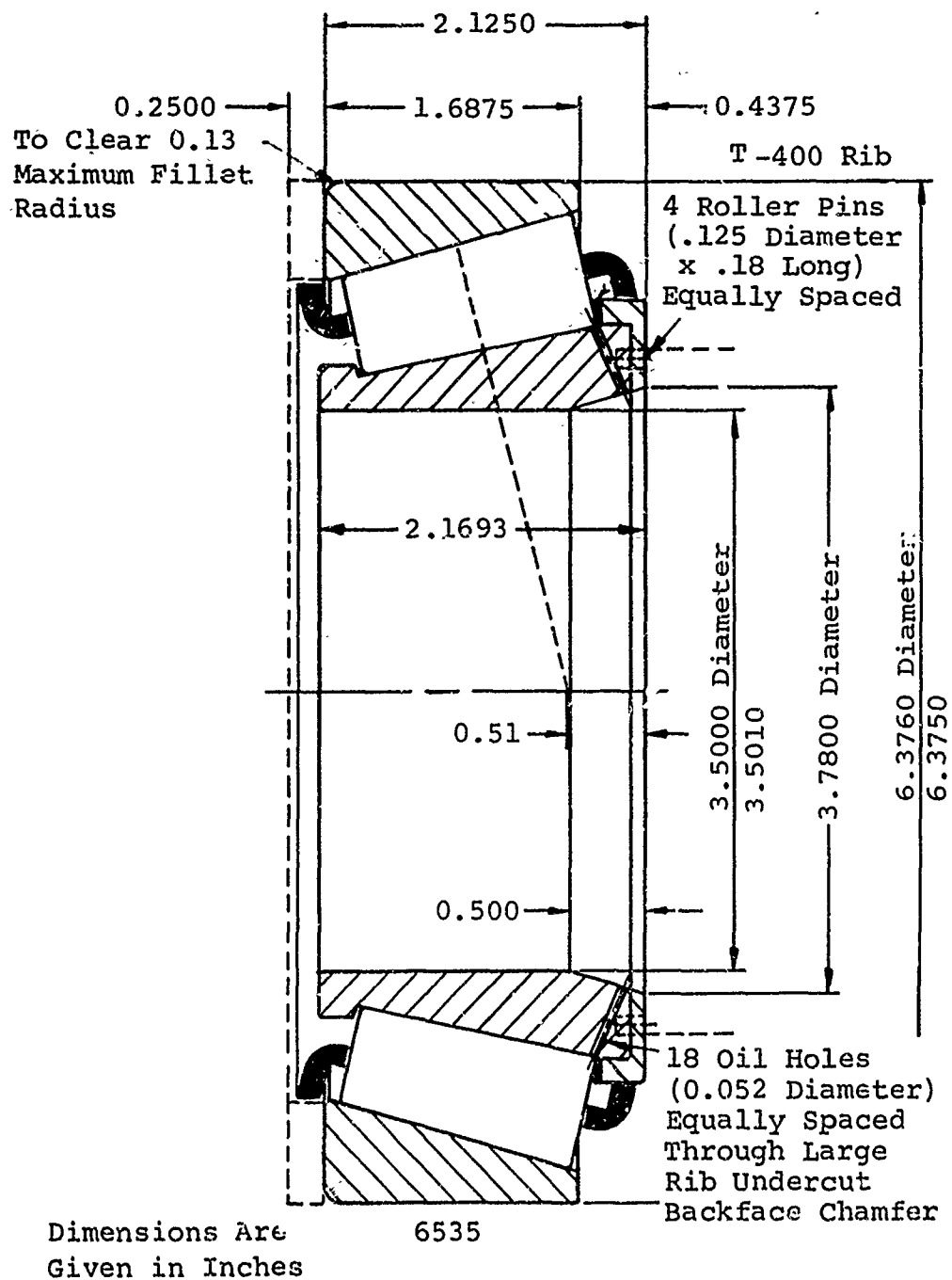
Figure 15. Fail-Safe Bearing Design With T-400 Rib.
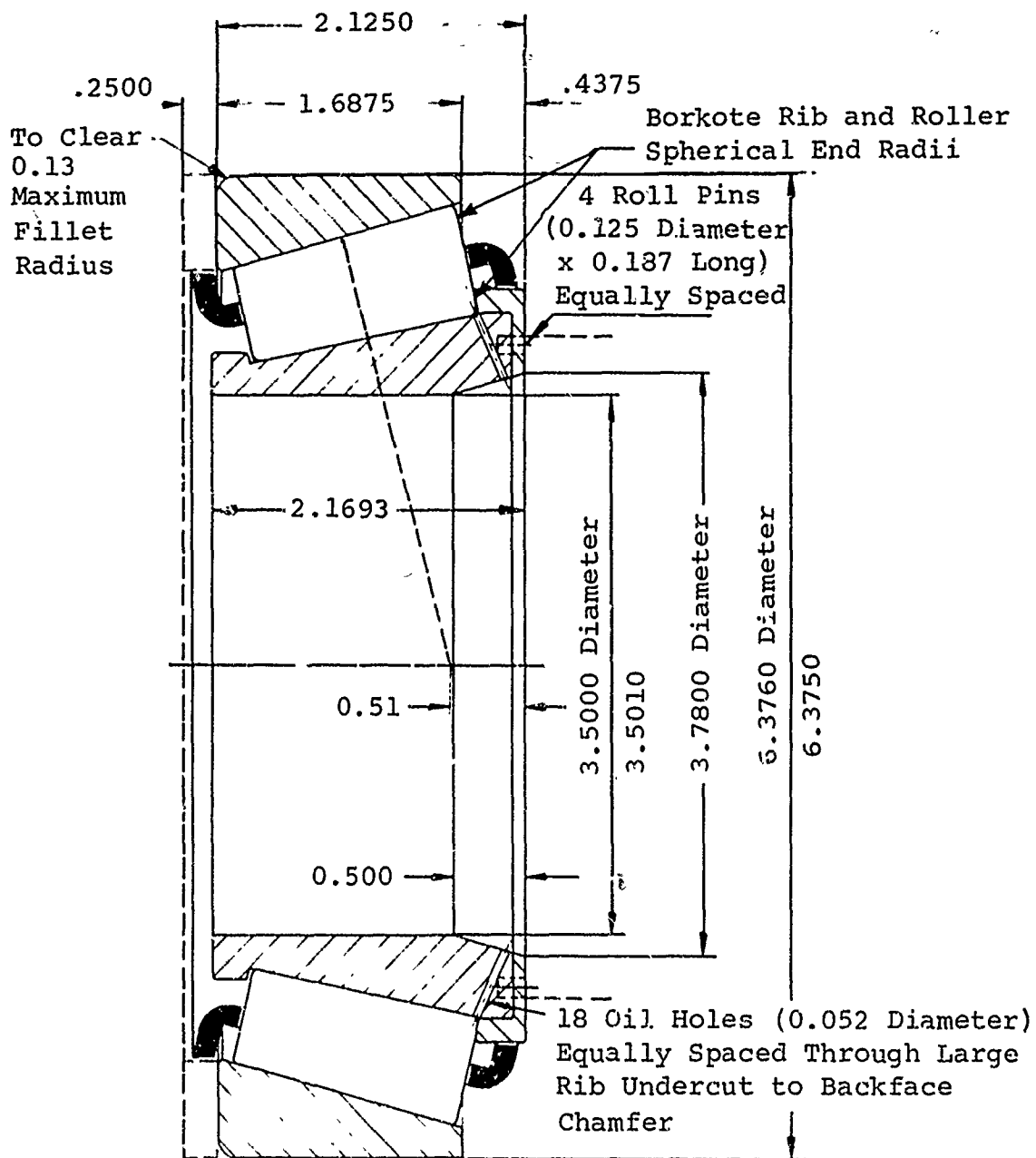
Figure 16. Fail-Safe Bearing Design With Borkote Rib.

34

This type of cage was chosen to facilitate inserting a fail-safe material between each roller for oil-off operation.

The Vespel SP-21 material used for the fail-safe rib inserts was purchased from the E. I. DuPont De Nemours and Company, Inc. Vespel SP-21 is a polyimide resin composite material containing 15 percent graphite by weight. Scotch-Weld Structural Adhesive 2216 B/A and 2214 (Hi-Temp) recommended by DuPont were used to bond the rib inserts to the cones.

The T-400 alloy made by the DuPont Company contains hard grains of an intermetallic compound of a Laves Phase (LP) structure dispersed in a softer matrix. T-400 is composed of 62 percent cobalt, 28 percent molybdenum, 2 percent silicon, and 8 percent chromium. The T-400 was hot consolidated into a ring by Principio Alloys Division of Wheeling-Pittsburgh Steel Corp., Columbus, Ohio. (Hot consolidation is a Principio patented process.) This ring was then high-temperature brazed onto a 4720 steel separable-rib ring. The T-400 and 4720-steel rings were oil quenched at 1400°F in the brazing process. The brazing compound (AMI 915) was made by Alloys Metals, Inc., Dearborn, Michigan. Four 1/16-inch x 1/16-inch x 0.002-inch shims were used between the T-400 ring and the steel ring for capillary action.

Borkote is a boronizing process developed by Atlantic Advanced Metals, Inc., Woburn, Massachusetts. It produces a hardened case on various ferrous and nonferrous materials. The Borkote was applied by Principio Alloys Division. The Borkote was applied to 1050 steel separable ribs at 1550°F and allowed to air cool. The Timken Company finish-ground the ribs before the Borkote treatment.

The 4320-steel rollers to be Borkote-treated were first processed by Timken as follows:

- Carburized at 1750°F

- Oil Quenched

- Austenitized 1525°F Oil Quenched

- Body Rough Ground

- Roller Spherical End Radius Finish-Ground

Principio then processed them as follows:

- Austenitized in Borkote at 1525°F

- Oil Quenched

- Tempered at 360°F for 2 Hours

35

After the Borkote process, Timken finish-ground the roller body. It was discovered that the rollers became barrel shaped in the Borkote process. The roller spherical-end radius was then reground with a minimum of stock removal. A metallurgical check showed that the Borkote was then from 0.0 to 0.0005 inch deep.

The machined race-guided centerline-contact cages were made from 1010 steel. Principio Borkote-treated them as follows:

- Austenitized in Borkote at 1550°F to 1600°F

- Air cooled

The fail-safe bearing configurations are shown in Figures 17 and 18.

TEST PROCEDURE

In order to determine the influence of various bearing design factors on performance, this program evaluated parameters such as roller spherical-end radius, cage plating materials, cage clearances, oil distribution at the cone rib interface, surface finish, and oil flow rates.

All tests were conducted by performing rotating-load testing in a high-speed test machine with a 40-horsepower variable-speed DC gear motor. During the testing, instrumentation was provided for obtaining critical parameters such as temperature, friction torque, and oil flows. The testing was conducted in accordance with the flow chart shown in Figure 19 under the following stabilized conditions:

- Speed   5000 to 16,000 rpm

- Load   Thrust 5500 lb

    Radial 7500 lb

- Oil Inlet Temperature   156°F ± 5°F

- Lubricant   MIL-L-7808

- Oil Flow Rates   Large end 4-0 Pints/Minute

    Small end 4-0 Pints/Minute

The optimum flow rate was established on the basis of minimum flow requirements and temperature stabilization.

36

Machined Race Guided
Centerline Contact Cage   Cup Ring
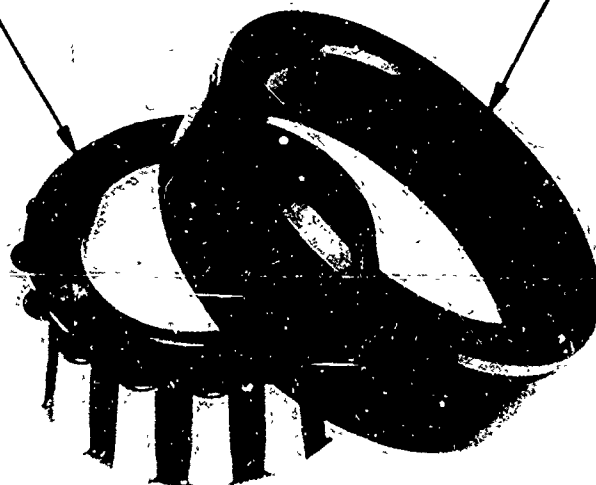
Borkote-Treated Cage Tested With Cone Having a Vespel SP-21
Rib Insert, Standard Rollers, and Borkote-Treated Cone Rib
and Roller Ends.

Figure 17.   Typical New Fail-Safe Bearing.

37

Silver-Plated Cage Tested With Cone Having a Vespel SP-21
Rib Insert, Standard Rollers, and a T-400 Cone Rib.

Figure 18. Typical New Fail-Safe Bearing.

```
                    ┌──────────────────────────────────┐
                    │      Fabricate Test Bearings     │
                    └──────────────────────────────────┘
                    ┌──────────────────────────────────┐
                    │   Evaluate Roller Rib Contact    │
                    │      Constant Parameters:        │
                    │                                  │
                    │  ● Cage Plating (Phosphate)      │
                    │  ● Number of Holes (18)          │
                    └──────────────────────────────────┘

┌───────────────────────┐  ┌───────────────────────┐  ┌───────────────────────┐
│ 80% Spherical End Radius│  │ 70% Spherical End Radius│  │ 60% Spherical End Radius│
└───────────────────────┘  └───────────────────────┘  └───────────────────────┘
                    ┌──────────────────────────────────┐
                    │ Evaluate Test Results and Determine│
                    │    Optimum Roller End Radius     │
                    │    (Radius to Remain Constant)   │
                    └──────────────────────────────────┘
                    ┌──────────────────────────────────┐
                    │      Evaluate Cage Plating       │
                    │       Other Than Phosphate       │
                    └──────────────────────────────────┘

     ┌───────────────────────┐              ┌───────────────────────┐
     │   Silver-Plated Cage  │              │   Brass-Plated Cage   │
     └───────────────────────┘              └───────────────────────┘
                    ┌──────────────────────────────────┐
                    │ Evaluate Test Results and Determine│
                    │   Optimum Cage Plating Material  │
                    └──────────────────────────────────┘
                    ┌──────────────────────────────────┐
                    │ Evaluate Increased Oil Distribution│
                    │      On Cone Rib Interface       │
                    │ Number of Lube Holes Increased to 24│
                    └──────────────────────────────────┘
                    ┌──────────────────────────────────┐
                    │      Evaluate Cage Design        │
                    │         Modifications            │
                    └──────────────────────────────────┘
                    ┌──────────────────────────────────┐
                    │ Determine Optimum Bearing Configuration│
                    │    Based on Above Test Results   │
                    └──────────────────────────────────┘
                    ┌──────────────────────────────────┐
                    │  Verify Test of Optimum Bearings │
                    └──────────────────────────────────┘
                    ┌──────────────────────────────────┐
                    │  Evaluate Four Fail-Safe Bearing │
                    │         Configurations           │
                    └──────────────────────────────────┘
```
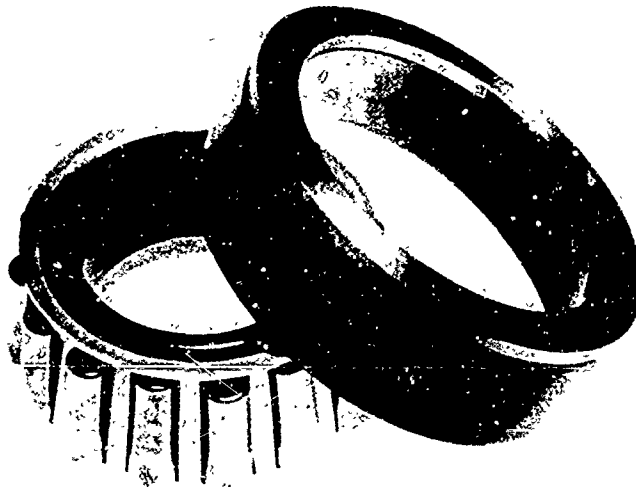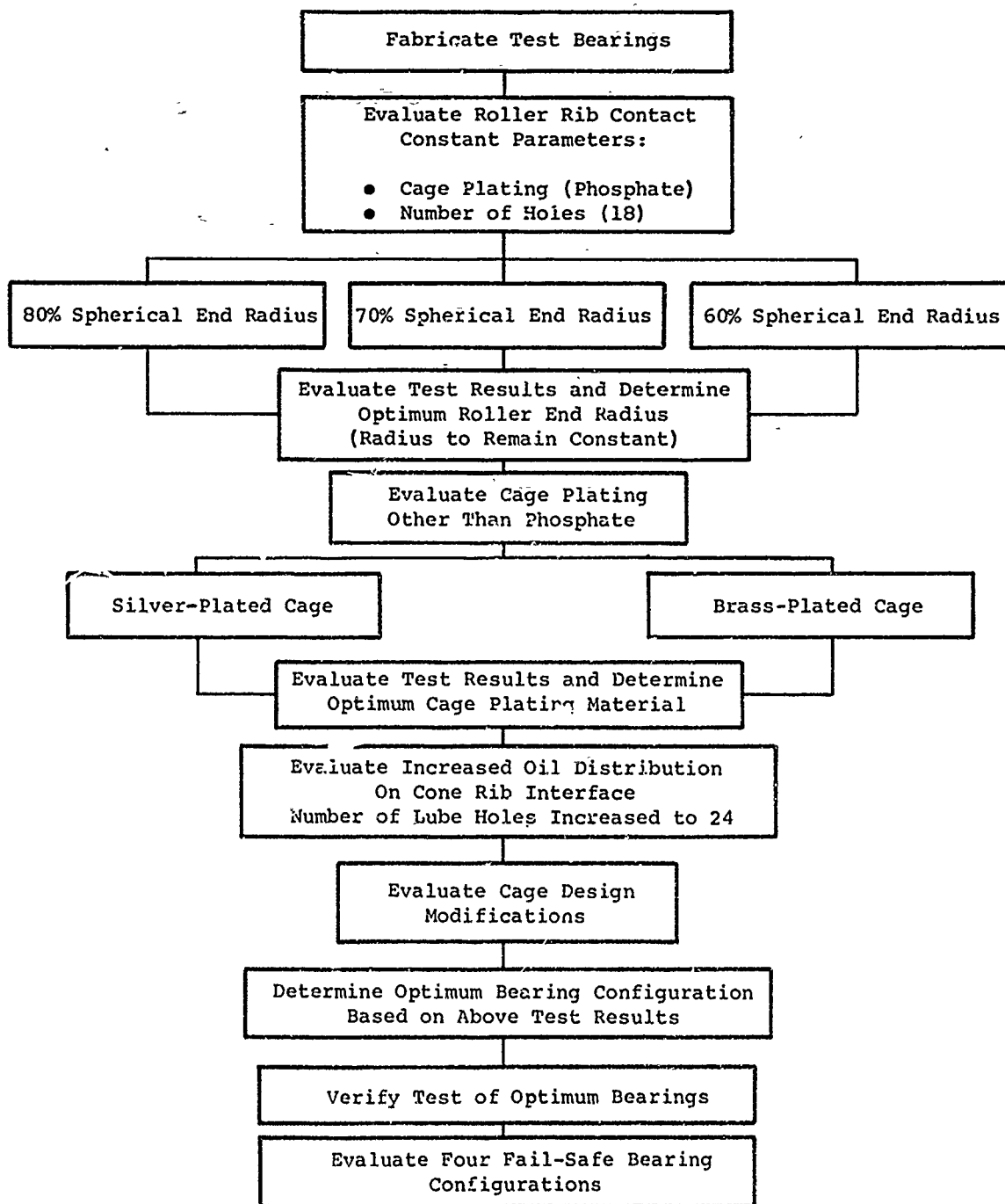
Figure 19.   Test Program Flow Chart.

39

For the oil flow variation tests, temperature and torque were recorded when conditions leveled off. The speed was increased until a maximum of 16,000 rpm was reached, or until bearing failure occurred. All conditions were stabilized for a minimum of 2 hours. If no failure occurred, running at 16,000 rpm was continued and the oil flow was varied. The system was then stabilized at each new flow rate or a failure point was determined.

The following data was recorded for each test:

- Outer Race Temperature

- Oil Flow

- Oil Inlet Temperature

- Oil Outlet Temperature

- Condition of Bearing at Completion of Testing

- Friction Torque

- Speed

- Load

After each variable was evaluated, an optimum value was established for this parameter and maintained for the continuation of the program.

The verification testing was conducted in the same manner as the previous testing; however, the following optimum design and operating parameters were utilized:

- Twenty-Four Cone-Rib Lub Holes

- Eighty Percent Roller Spherical-End Radius

- Finish of 8 Microinches

- Silver-Plated Cage

- Oil Flow Rates of 4 Pints/Minute at the Large End and 2 Pints/Minute at the Small End

In addition, verification tests were run at 80 percent and 60 percent of the basic load (7500 lb radial and 5500 lb thrust) with the optimized design and operating parameters listed above.

40

Instrumentation was provided to obtain adequate data (such as temperatures and power consumption) and to accurately evaluate the performance of each bearing. Each test bearing was visually examined after completion of testing to determine any evidence of wear or damage. Each new bearing design was photographed before and after every test.

Calibration of test and measuring equipment was in accordance with MIL-L-45662A in the performance of all testing.

TEST APPARATUS AND TECHNIQUE

Figures 20 through 23 are photographs of the test machine. The bearings are driven by a 40-horsepower variable-speed DC gear motor.

Figure 24 is a cross section of the test machine housing. Figure 25 is a schematic diagram showing the bearing mounting, loading, and lubricating system.

The manifold projecting into the hollow shaft discharges oil through orifices located axially in line with the radial holes in the shaft. There are two 3/16-inch radial holes through the shaft at each bearing position. The dams located between each bearing position along the length of the shaft serve to assure an equal distribution of lubricating oil to the four bearings. The cone backface chamfer (oil manifold) collects the oil and distributes it to the radial holes in the cone to lubricate the cone rib and roller ends (see Figure 26). Three 0.040-inch jets located at the small end of the bearing 120 degrees apart discharge the oil underneath the cage to lubricate the cage roller body contact and inner and outer race. The oil flow rate supplied to each bearing was calibrated by collecting the oil with a graduated measuring cup while being timed with a stopwatch. The oil flow rate was recorded on a strip chart and could be read directly from a digital counter. In addition, each orifice on the manifold projecting into the hollow shaft was sized and calibrated to assure an equal amount of oil supplied to each bearing.

The bearing cup OD, oil inlet, oil outlet, and ambient air temperatures were measured by strategically located thermocouples. Each thermocouple was calibrated with a precision laboratory thermometer. The temperatures are read and recorded on a strip-chart recorder.

The test housing was mounted on a Lebow Model 2230-101 torque table with 1,000 lb-in. rated capacity to measure and record the torque of the bearing system and to provide a means for detecting initiation of any damage to the bearings. Before
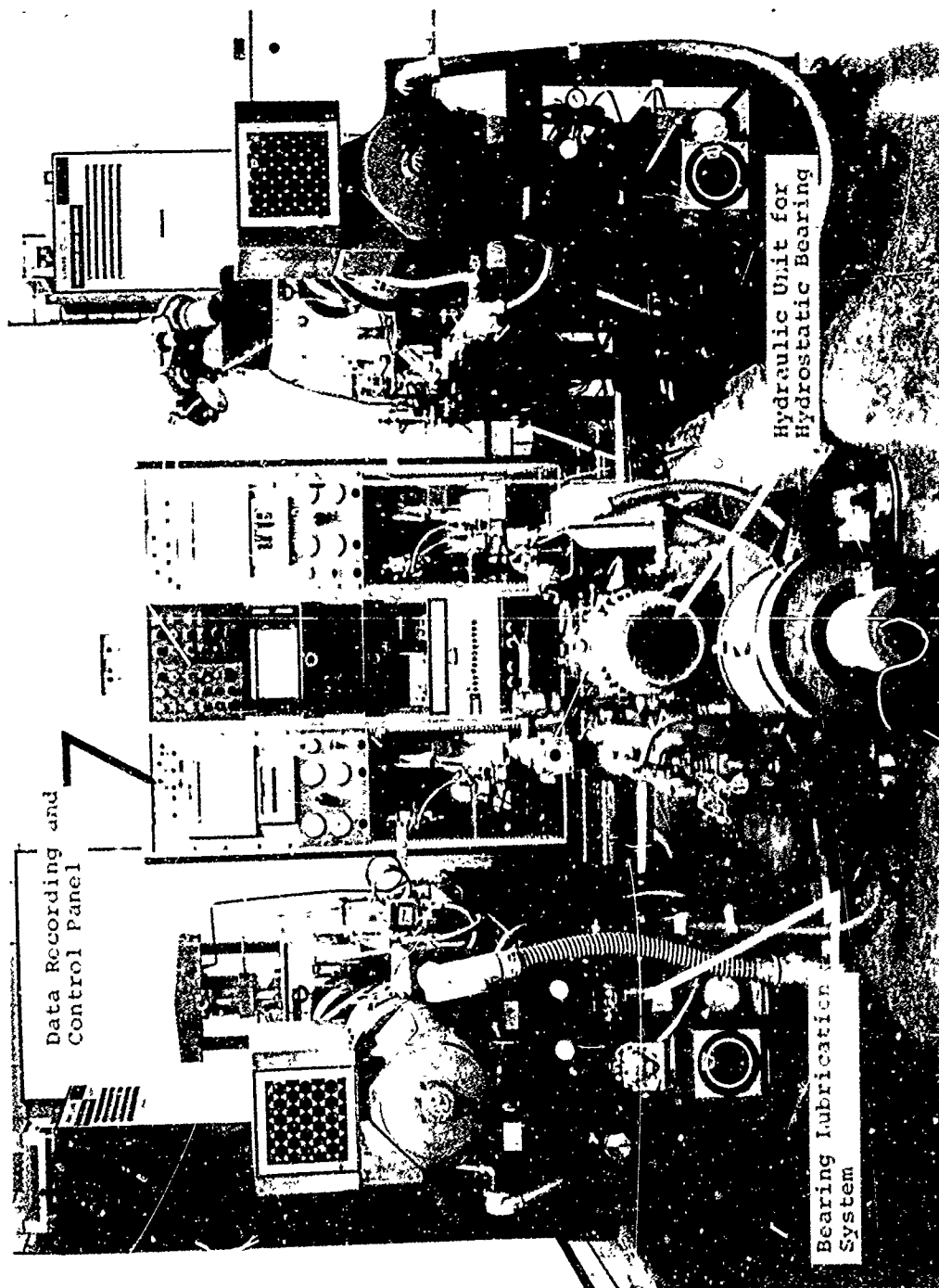
41
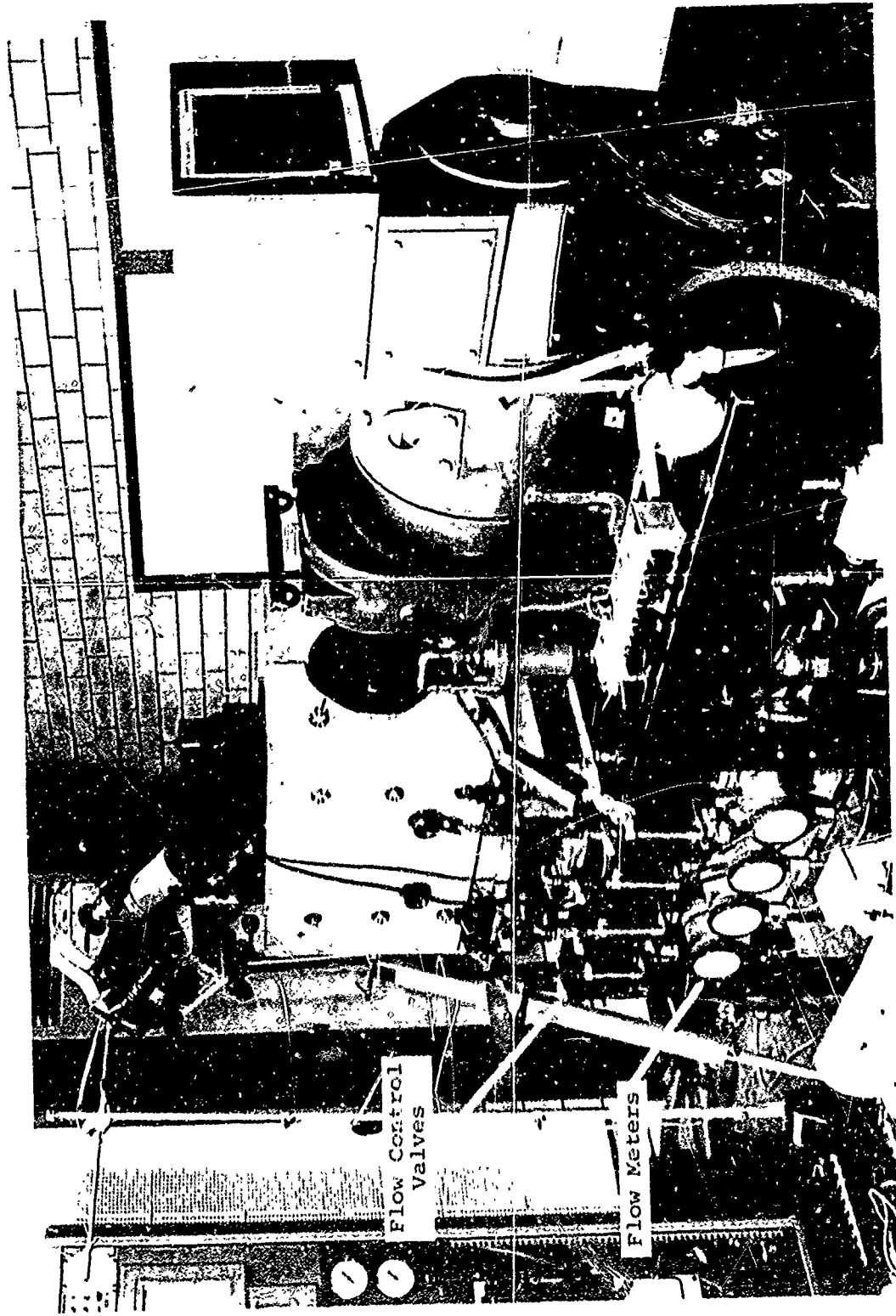
Figure 20. High-Speed Bearing Test Machine.

42

Figure 21. Lubricant Flow-Control System.

Flow Control Valves

Flow Meters

43
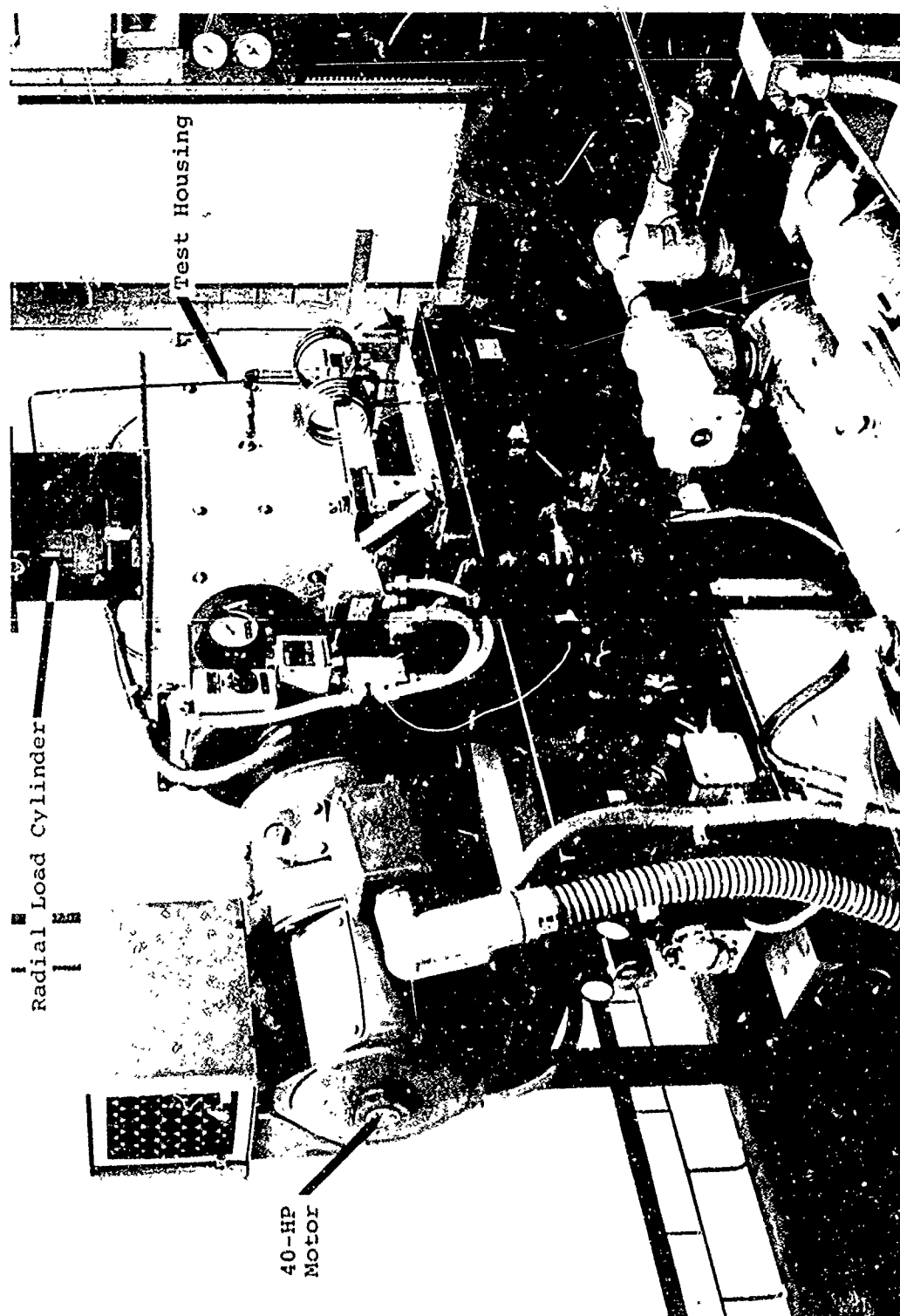
Figure 22. 40-Horsepower Variable-Speed DC Gear Motor.

Oil Flow and Radial
Thrust Load Recorder

Temperature Recorder

Torque Recorder

Radial Load
Controls

Shaft Speed
Digital Counter

Oil Flow
Digital Counter
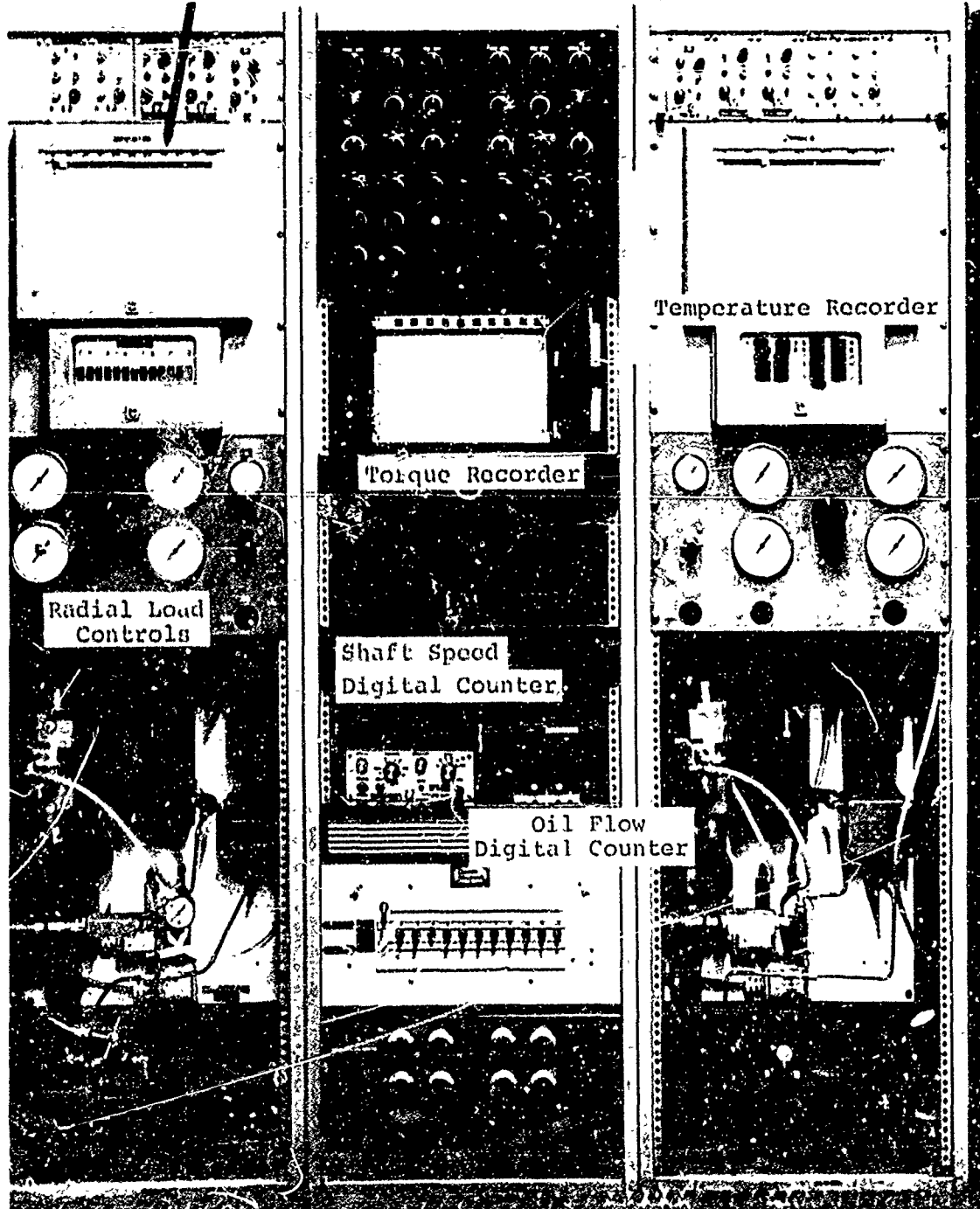
Figure 23.   Control and Data Recording Panel.

Center Cup
CPL-12...

End Cone Spacer
APL-12195

Center Oil Manif...
BPL-12194

Oil Jet Manifold ODE
CPL-12191

LH Oil Dam
Assembly
CPL-12660

Center Cone
Spacer
APL-12196

Oil Jet Inlet
60 PSI

Load Plate
BPL-13009

Thrust Loading
Assembly CPL-12712

Cone Lubrication

Overflow

Locking Cap
BPL-12186

Thermocouple Leads
End Cups
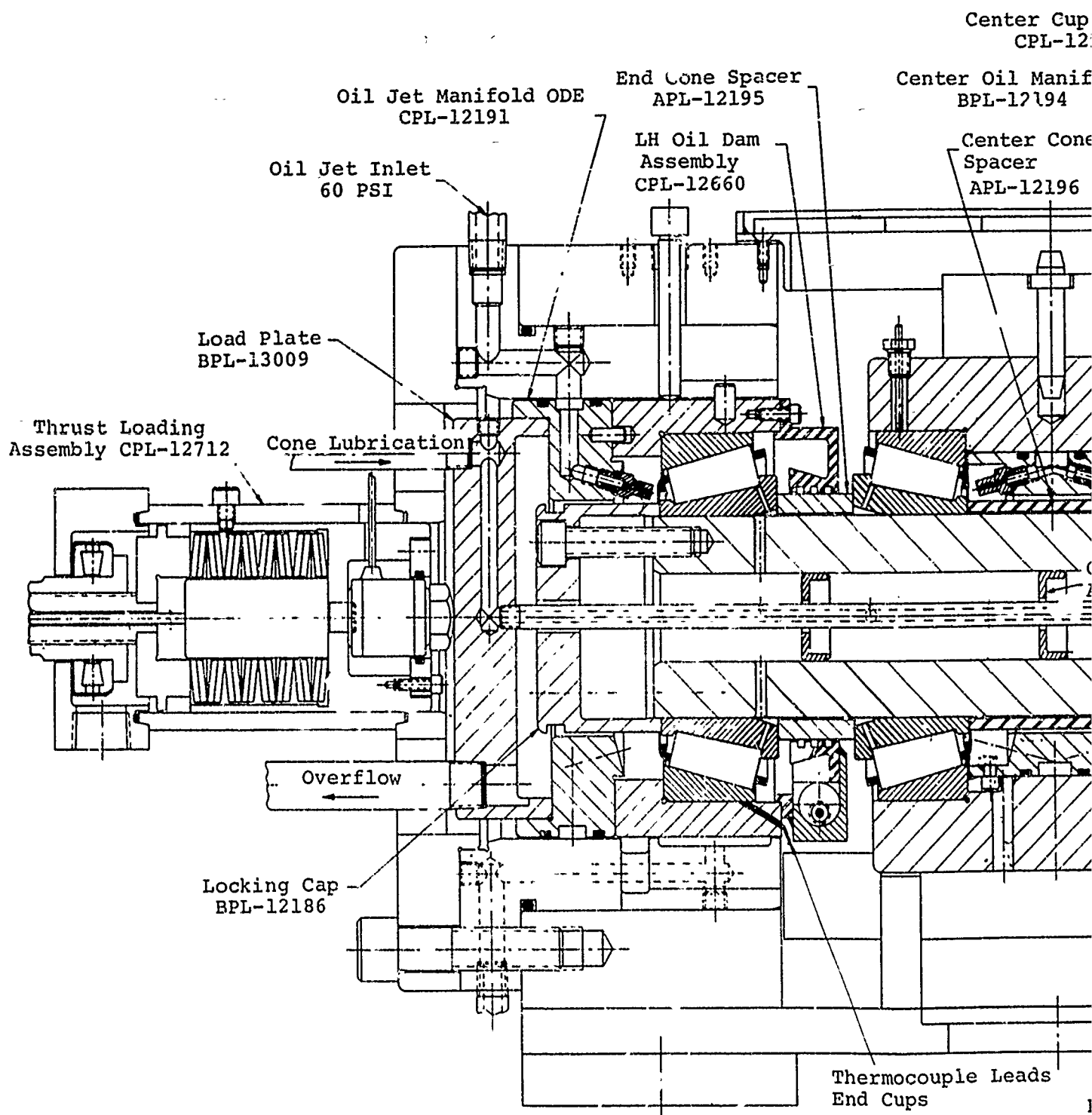
Figure 24.   Full-Size Subassembly Bearing High-Speed Test
Using Hollow Shaft.

Center Cup Adaptor
CPL-12193

Center Oil Manifold
BPL-12194

Center Cone
Spacer
APL-12196

RH Oil Dam Assembly
CPL-12650

Cup Adaptor
CPL-12187

Oil Jet
APL-12190

Oil Jet Manifold DE
CPL-12189

Labyrinth Seal
BPL-12182

Oil Dam
APL-13082

High-Speed Coupling
CPL-13023

Oil Jet Inlet
60 PSI

Cone Shown APL-13103 - 653
Bearing Assembly

Full Size

Thermocouple Leads
End Cups

Thermocouple
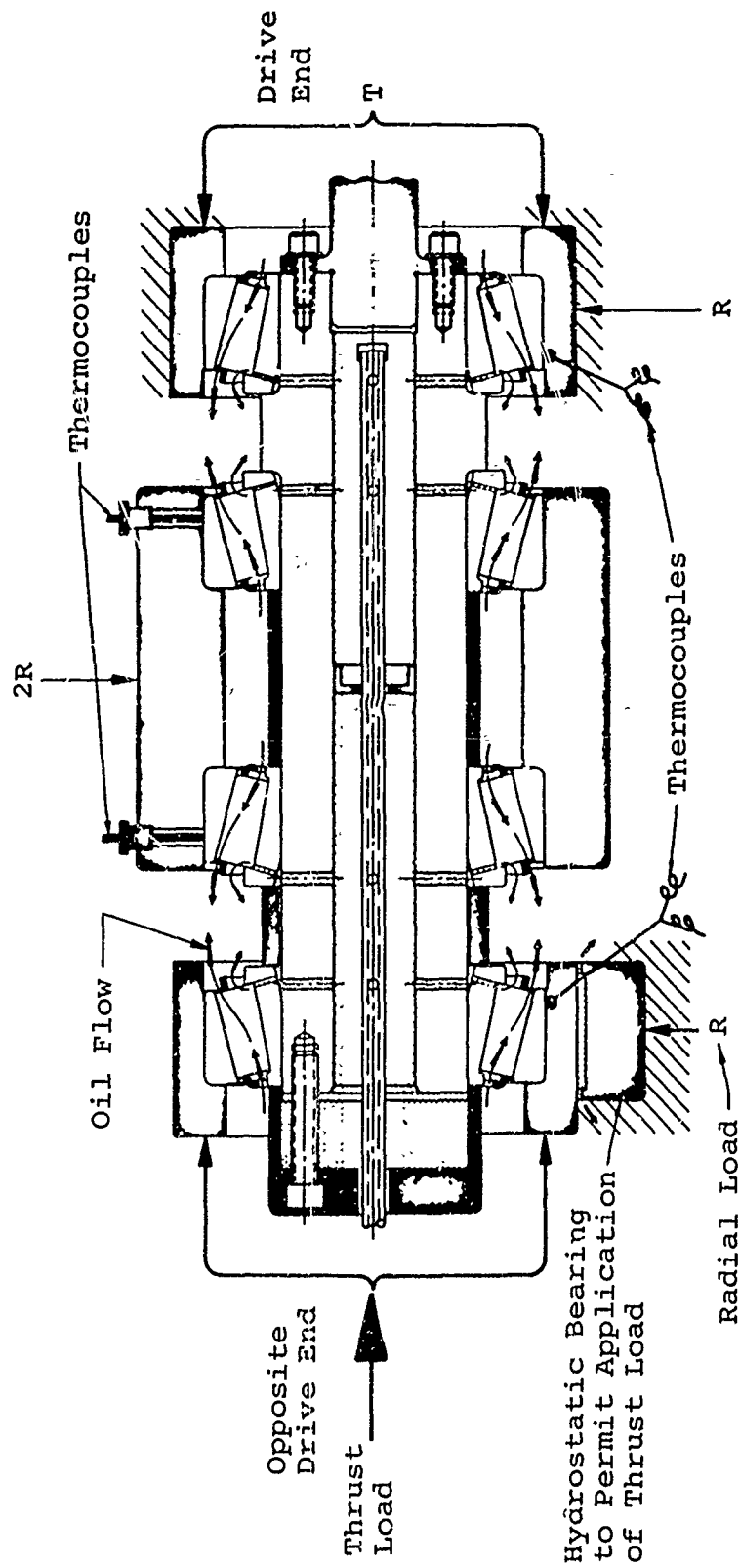Return Oil Temp

Figure 25. Schematic Diagram Showing Thermocouples, Lubrication System and Bearing Loading System. (Drive end bearing cup adapter is fixed. Opposite drive end bearing cup adapter is free to move axially on hydrostatic bearing.)

Preceding page blank

Bearing Cone

Cone Backface
Chamfer (Oil Manifold)

Test Shaft

Oil Collects Here
and is Distributed
to Radial Holes in
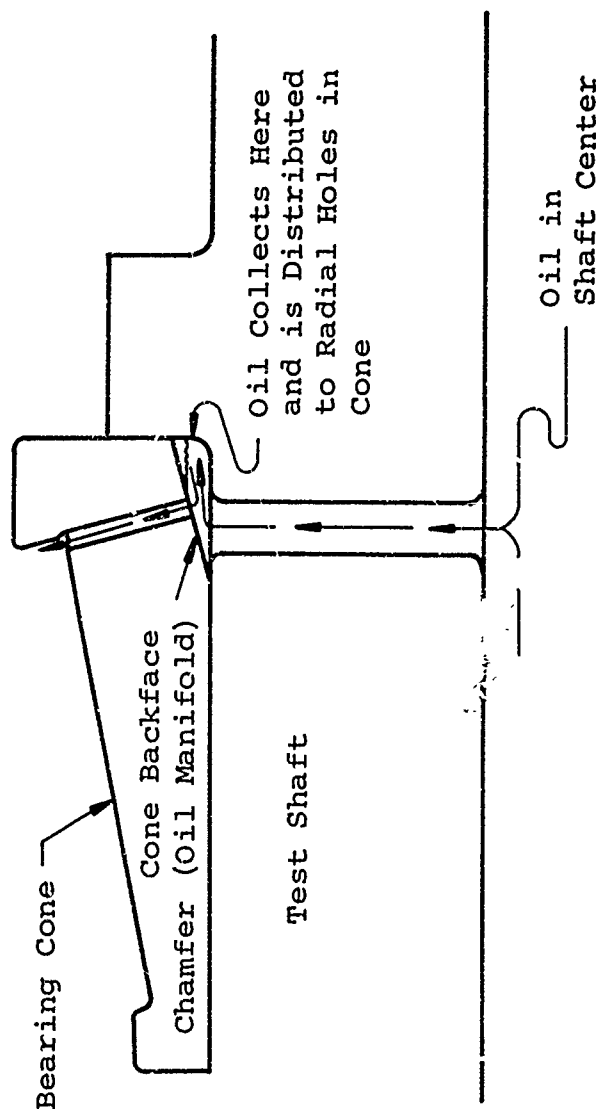Cone

Oil in
Shaft Center

Figure 26. Line Diagram Showing Lubricating Oil Collecting
at Top of Cone Backface Chamfer to Distribute Oil
to the Radial Holes to the Large End Rib.

each day's run, the torque table was calibrated with dead weights.

In this test program, four bearings were run at a time. The center two bearings were used to apply the radial load to the outer two bearings (see Figure 25). The outer two test bearings were run under a combination of radial and thrust loads. The center loading (radially loaded only) bearings were not changed each time a test was completed.

The thrust load applied to the outer bearings was measured by a Lockheed Model No. 1552 load cell. Belleville springs were used to apply the load. The thrust load cell was calibrated with a Baldwin Universal Testing Machine with a 120,000-pound capacity.

The radial load applied to the inner bearings was measured by pressure gages. A Miller hydraulic cylinder, Model No. H82, was used to apply the load to the cup (outer race) adapter of both center loading bearings. The radial load pressure gages were calibrated with a master pressure gage.

The bearing lubrication system is equipped with a heat exchanger to control the inlet oil temperature at a given value and with flow controls capable of maintaining any desired flow rate.

Four 55-gallon drums of MIL-L-7808G (Stauffer Chemical Company) were used in this test program. All four drums are identified as follows:

LGT
Lube Oil AGFT
Turb. Engine
Synthetic
MIL-L-7808G
9150-782-2679

Nov. 69   Lot 27
DSA 600-69-C-1722 Qual. 18C-3

TEST RESULTS

Bearings tested and documented during this program totalled 40; 28 bearings were used to optimize critical parameters and 8 were tested to verify the results of the optimization tests. An additional 4 bearings were used to conduct the evaluation of several fail-safe bearing configurations. The results of these tests are documented in the following sections.

Optimization Testing

Testing was conducted on a total of 28 bearings in order to optimize the essential parameters to provide satisfactory operation of a tapered roller bearing at 20,000 fpm. Prior to testing of each bearing, a detailed inspection and dimensional check were conducted. Results are shown in Table IV. Also included in this table are several after-test dimensional checks which were used to evaluate the performance of the bearing.

The results of the testing of the above 28 bearings are summarized in Table II. The table shows the various parameters which were investigated, operating oil flow rates, bearing temperature, oil outlet temperature, and operating torque of all four bearings on the test shaft. The data shown on this table is for stabilized operating conditions which required approximately 2 hours of running time at each test condition.

The following paragraphs discuss the various parameters which were investigated and evaluate the test results shown in Tables II and IV.

Bearing Element Failure Modes

Optimization testing conducted in this program was not directed toward evaluating long-endurance operation or fatigue life of a tapered roller bearing. It was specifically directed toward evaluating the oper. ion of several critical parameters influenced by lubrication. All failures experienced during this program were the result of surface damage occurring on one or more of the elements of the bearing. The type of damage that occurred is described as follows:

- Roller-end/cone-rib scuffing - This classification of damage was the most severe form of bearing failure. Roller-end/cone-rib scuffing is the result of lubrication starvation or breakdown at roller-end/rib contact. The failure results in sufficient increase in operating torque to cause termination of testing. A typical example of roller-end scuffing is shown in Figure 27.

- Cage roller pocket wear - Cage roller pocket wear is associated with marginal lubrication. Severe cage roller pocket wear usually occurred at very low oil flow rates to the small end of the bearing. This wear did not produce any noticeable increase in operating torque or temperature. Testing could continue with this mode of failure until cage

52

Bearing No. Drive End/Opposite Drive End	Test No	Member of Radial Holes Through Cone	Race Flatness Cone	Roller Bodies	Roller Spherical End Radius + Apex	Cone Rib Angle (Deg/Min/Sec)	Cone Bore (In.)
83031-1	1	18	Flat	Crown	80	11 23 30	3.5002
83031-2	1	18	Flat	Crown	80	11 23 30	3.5002
83031-3	2	18	Flat	Crown	80	11 23 30	3.5002
83031-4	2	18	Flat	Crown	80	11 23 30	3.5002
83031-5	3	18	Crown	Crown	70	11 13 0	3.5002
83031-6	3	18	Crown	Crown	70	11 13 0	3.5002
83031-7	4	18	Crown	Crown	70	11 13 0	3.50055
83031-8	4	18	Crown	Crown	70	11 13 0	3.5003
83031-9	5	18	Crown	Crown	60	10 54 0	3.5003
93031-10	5	18	Crown	Crown	60	10 54 0	3.5007
83031-11	6	18	Crown	Crown	60	10 54 0	3.50035
83031-12	6	18	Crown	Crown	60	10 54 0	3.50045
83031-13	7	18	Flat	Crown	80	11 23 30	3.5001
83031-14	7	18	Flat	Crown	80	11 23 30	3.5001
83031-15	8	18	Flat	Crown	80	11 23 30	3.5003
83031-16	8	18	Flat	Crown	80	11 23 30	3.5002
83031-17	9	18	Flat	Crown	80	11 23 30	3.5002
83031-18	9	18	Flat	Crown	80	11 23 30	3.5002
83031-19	10	18	Flat	Crown	80	11 23 30	3.5001
83031-20	10	18	Flat	Crown	80	11 23 30	3.5001
83031-19A	Rerun						
83031-17A	Rerun						
83031-21	11	24	Flat	Crown	80	11 28 30	3.5004
83031-22	11	24	Flat	Crown	80	11 18 45	3.5003
83031-24	12	24	Crown	Crown	80	11 28 30	3.5003
83031-23	12	24	Crown	Crown	80	11 18 45	3.5003
83031-31	13	18	Crown	Crown	80	11 18 45	3.5006
83031-25	13	18	Crown	Crown	80	11 28 30	3.5004
83031-31	13	18					
83031-25	13	18	Crown	Crown	80	11 28 30	3.5002
83031-25	13	18	Crown	Crown	80	11 28 30	3.5001
83031-31	13	18					
83031-25	13	18					
83031-31	13	18	Crown	Crown	80	11 23 30	3.5006
83031-33	17	18	Crown	Crown	80	11 18 45	3.5002
83031-32	17	18	Crown	Crown	80	11 23 30	3.5002
83031-27	14	24	Crown	Crown	80		3.5008
83031-26	14	24	Crown	Crown	80		3.5001
83031-29	15	24	Crown	Crown	80	11 18 45	3.5000
83031-28	15	24	Crown	Crown	90	11 18 45	3.5005
83031-34	16	24	Crown	Crown	80	11 18 45	3.5001
83031-30	16	24	Crown	Crown	80	11 18 45	3.5002
83031-35	18	24	Crown	Crown	80	11 23 30	3.5007
83031-36	18	24	Crown	Crown	80	11 23 30	3.50015
83031-35	Rerun Bearing	24					
83031-34	No. 83031-30	24					

(*) Surface finish measured after standard double pitching.

Cone Bore (In.)	Cone Fit (In.)	Cone(*) Rib Face	Surface Finish (AA) Cone(*) Race	Roller Bodies	Roller Spher End	Overall Bearing Width Before	After	Change	Cage Shake Before	After Test	After Test Visual Examination Cone	Rollers Spher end radius (SER)	Cage
3.5002	.0048	12-13	8.8-9.2	4.2-4.6	7.2-7.6	2.1280			.0086	.0082	OK	OK	OK
3.5002	.0048	13-14	9.2-9.6	4.2-4.6	6.8-7.4	2.1288			.0066	.0067	OK	OK	OK
3.5002	.0048	11-12	9.4-9.8	4.0-4.8	6.8-7.6	2.1270	2.1272	+.0002	.0083	.0113	Rib scuff	Scuff and pickup	Wea
3.5002	.0048	10-11	9.4-10	4.4-4.8	6.8-7.6	2.1280	2.1281	+.0001	.0076	.0070	OK	OK	OK
3.5002	.0048	8-14	6-10	3-6	2-5	2.1291	2.1300	+.0009	.005	.017	Rib scuff	Scuff and pickup	Wea
3.5002	.0048	10-14	7-14	3-5	3-6	2.1284	2.1299	+.0015	.0073	.0077	OK	OK	OK
3.50055	.00455	12-16	5-8	3-6	3-6	2.1281	2.1286	+.0005	.006	.0062	OK	OK	OK
3.5003	.0047	9-12	6-10	3-5	3-5	2.1279	2.1290	+.0011	.006	.0063	Rib scuff	Scuff and pickup	Wea
3.5003	.0047	6-12	6-10	3-5	4-7	2.1280	2.1281	+.0001	.0057	.006	Rib scuff	Scuff and pickup	Wea
3.5007	.0043	8-14	7-12	3-6	3-6	2.1275	2.1277	+.0002	.0063	.006	OK	OK	OK
3.50035	.00475	7-12	7-12	3-5	3-6	2.1279	2.1279	0	.0073	.0093	Rib scuff	Scuff and pickup	Wea
3.50045	.00465	7-13	6-12	3-5	4-7	2.1276	2.1276	0	.006	.0093	OK	OK	OK
3.5001	.0047	9-10	18-19	8-9	7-8	2.1258	2.1267	+.0009	.0053	.005	OK	OK	OK
3.5001	.0049	8-9	12-13	9-10	7-8	2.1261	2.1266	+.0005	.0057	.0097	Rib scuff	Scuff and pickup	Wea
3.5003	.0047	6-1/2 9-1/2	8-9	8-9	7-8	2.1251	2.1265	+.0014	.0067	.005	OK	OK	OK
3.5002	.0048	9-10	10-10-1/2	8-9	7-8	2.1256	2.1284	+.0028	.006	.0063	OK	OK	OK
3.5002	.0046	10-11	9-1/2 - 10-1/2	8-9	7-8	2.1255	2.1262	+.0007	.0071	.0133	OK	OK	OK
3.5002	.0048	9-1/2 10	9-10	6-7	7-8	2.1262	2.1269	+.0007	.0087	.016	Rib scuff	Scuff	OK
3.5001	.0047	8-9	10-1/2 - 11-1/2	7-8	7-8	2.1252	2.1253	+.0001	.0067	.0063	OK	OK	OK
3.5001	.0049	11-1/2 12	11-11/1/2	8-10	7-8	2.1255	2.1255	0	.007	.0067	Rib scuff	Scuff	OK
											OK	OK	OK
											Rib scuff	Scuff	OK
3.5004	.0044	6-8	8-9	6-8	5-6	2.1252	2.1265	+.0013	.0077	.0087	OK	OK	OK
3.5003	.0047	10-14	8-9	6-7	5-7	2.1264	2.1285	+.0021	.0058	.0083	OK	OK	OK
3.5003	.0046	5-10	8-9	6-8	5-6	2.1274	2.1289	+.0015	.0067	.0076	OK	OK	OK
3.5003	.0045	10-12	8-10	6-7	5-7	2.1262	2.1271	+.0009	.0087	.010	OK	OK	OK
3.5006	.0042	6-13	10-12	6-8	5-7	2.1271	2.1272	+.0001	.0067	.006	OK	OK	OK
3.5004	.0044	10-15	8-10	6-8	5-7	2.1269	2.1271	+.0002	.0067	.007	Rib scuff	Scuff	OK
											OK	OK	OK
3.5002	.0048	10-15	9-10	4-6	6-7	2.1269	2.1273	+.0004	.0067	.0053	Rib scuff	Scuff	OK
3.5001	.0047	5-12	6-9	4-7	3-7	2.1270	2.1280	+.001	.0057	.006	OK	OK	OK
											Rib scuff	Scuff	OK
											OK	OK	OK
3.5006	.0044	4-7	4-6	5-9	2-6	2.1269	2.1279	+.001	.0065	.007	Rib scuff	Scuff	OK
3.5002	.0046	7-12			3-6	2.1270	2.1281	+.0011	.0053	.007	OK	OK	OK
3.5002	.0048	7-15			3-6	2.1261	2.1279	+.0018	.0057	.006	OK	OK	OK
3.5008	.0040	12-18	7-12	3-5	3-6	2.1250	2.1263	+.0013	.006	.0062	OK	OK	OK
3.5001	.0049	14-18	7-11	4-9	3-5	2.1259	2.1267	+.0008	.006	.0068	OK	OK	OK
3.5000	.0048	4-15	11-12	5.5-7.5	6-7	2.1258	2.1258	0	.0073	.009	OK	OK	OK
3.5005	.0045	3-13	11-12	5.5-6.5	6.5-7	2.1266	2.1271	+.0005	.0057	.006	OK	OK	OK
3.5001	.0047	4-15	10-11	5-7	7-8	2.1268	2.1279	+.0011	.0053	.0062	OK	OK	OK
3.5002	.0048	5-15	8-9	5-7	7-9	2.1268	2.1283	+.0015	.0055	.006	Rib scuff	Scuff	OK
3.5007	.0041	10-30	5-8	3-7	2-5	2.1249	2.1261	+.0012	.007	.009	OK	OK	OK
3.50015	.00485	7-15	4-8	3-6	3-6	2.1267	2.1267	+.0009	.007	.0085	Rib scuff	Scuff	OK
											OK	OK	OK
											OK	OK	OK

breakage occurred. No cases of cage breakage were recorded in this test program. A typical example of cage roller pocket wear is shown in Figure 28.

- Roller body scuffing (pickup) - Roller body scuffing is a secondary failure of cage roller pocket wear. The wear particles of the cage material are transferred to the roller body, producing a severe wear pattern on the roller body. This damage is associated with low oil flow rates or improper cage design. Testing can continue with this type of damage without noticeable increase in operating torque or bearing temperature. A typical example of roller body scuffing is shown in Figure 29.

- Cone raceway and roller body oil staining - The most minor form of bearing distress experienced in this program was a form of oil staining on the cone raceway and roller body. The oil staining was the result of high operating temperatures within the bearing which produced a varnish type coating on the operating surfaces. This type of distress is a good indication of possible surface damage and early fatigue damage due to high operating temperatures and lubrication breakdown. A typical example of raceway and roller staining is shown in Figure 30.

Oil Flow Rates

Figure 31 is a graph showing the shaft speed versus the bearing cup temperature and total torque of the four-bearing system from Test 1. Cup temperature and torque data points were recorded in 1000-rpm increments from 5000 to 16,000 rpm. Figure 32 shows the condition of the bearing after completion of this test.

Figures 33 through 36 are graphs showing oil-flow rates versus bearing cup temperatures and torque for Tests 1, 3, 7, and 11. In these tests, the oil-flow rate to the small end was varied, while the rate to the large end through the radial holes was held constant. From these graphs, an oil-flow rate of 2 pints/minute to the small end of the bearing was chosen as the optimum.

Figures 37 through 39 are graphs showing oil-flow rates versus cup temperatures and torque for Tests 8, 12, and 17. In these tests, the oil-flow rate through the radial holes was varied, while the rate to the small end of the bearing was held at a constant 2 pints/minute. From these graphs, an optimum oil-flow rate of 4 pints/minute through the radial holes in the cone and 2 pints/minute to the small end was chosen.

Roller Spherical
End Radius Scuffing
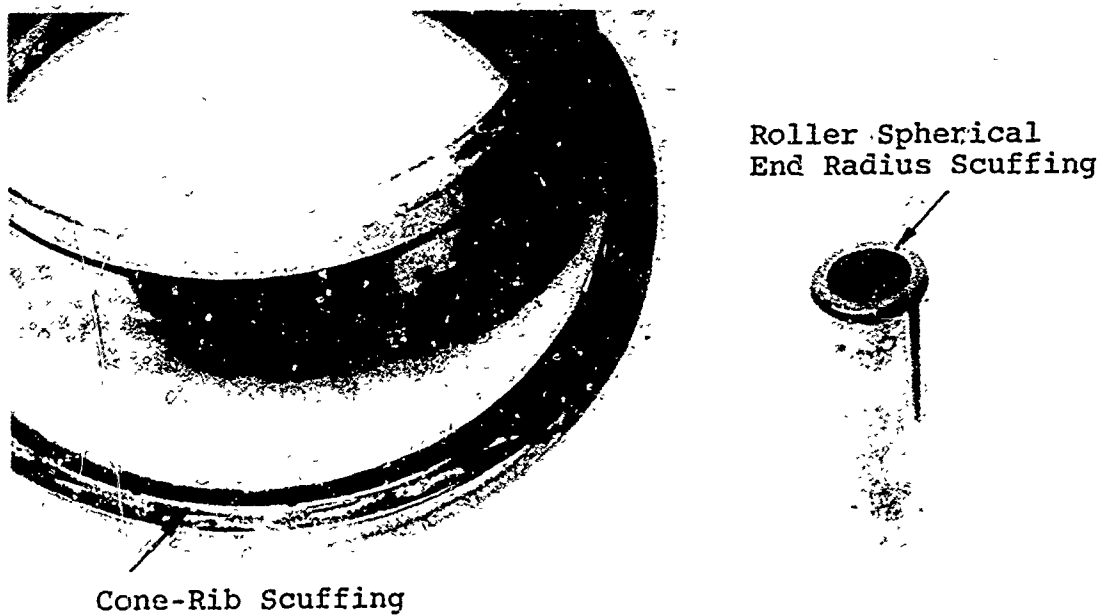
Cone-Rib Scuffing

Figure 27. Typical Roller-End/Cone-Rib Scuffing.
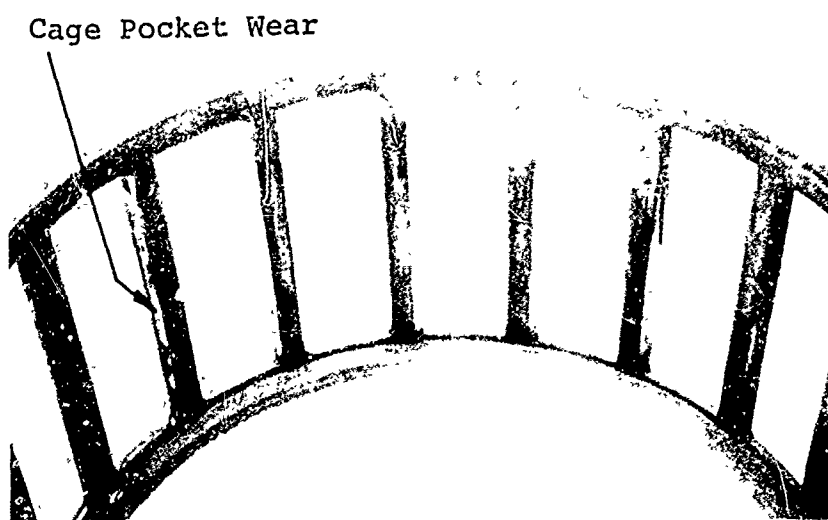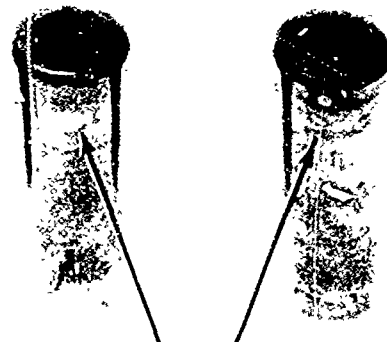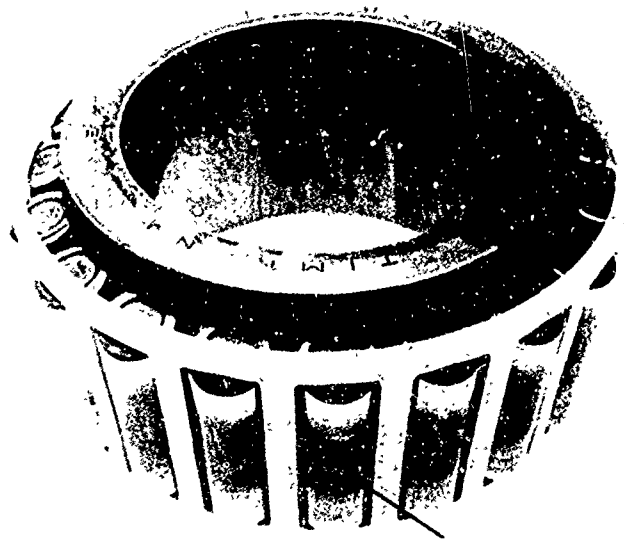

Cage Pocket Wear

Figure 28. Typical Cage Roller Pocket Wear.

Roller Body Scuffing

Figure 29. Typical Roller Body Scuffing.

Oil Stain

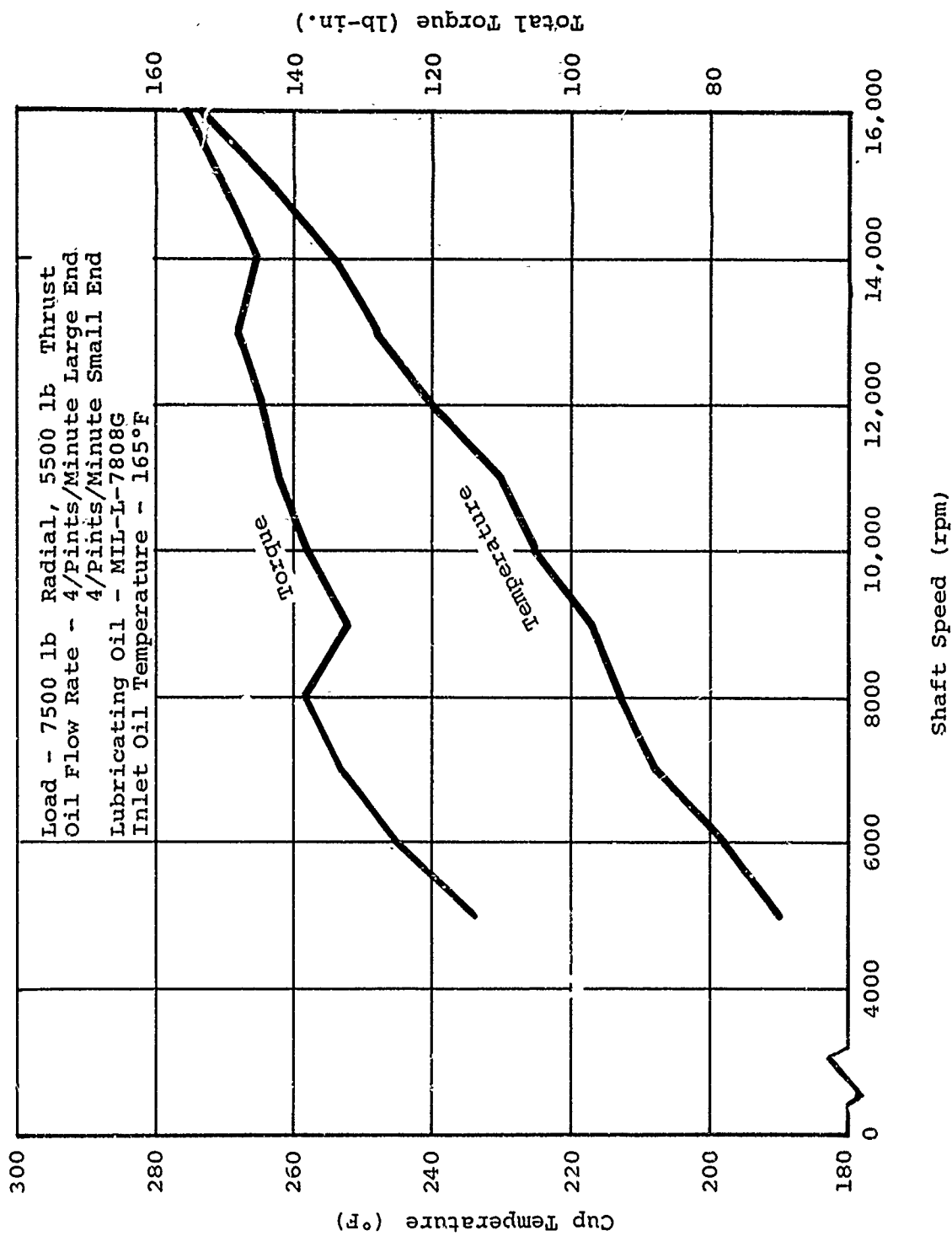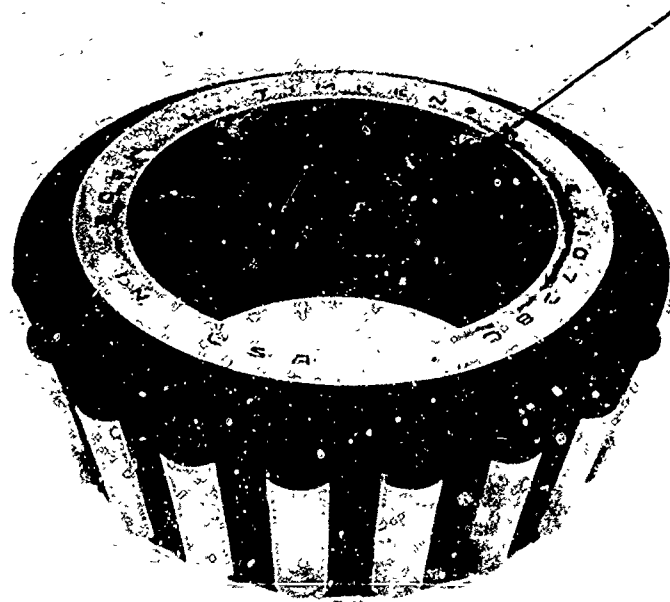Figure 30. Typical Cone Raceway and Roller Body Oil Staining.

Figure 31. Torque and Temperature Versus Shaft Speed (Test 1, Bearing 1).

58

Radial Lubricating
Oil Holes

Bearing 83031-1, Test 1, Running Time 10 Hours at 16,000 rpm
Oil Flow Rates as Low as 4 Pints/Minute Large End and No Flow
to the Small End

Figure 32.   Undamaged Bearing After Test.

59
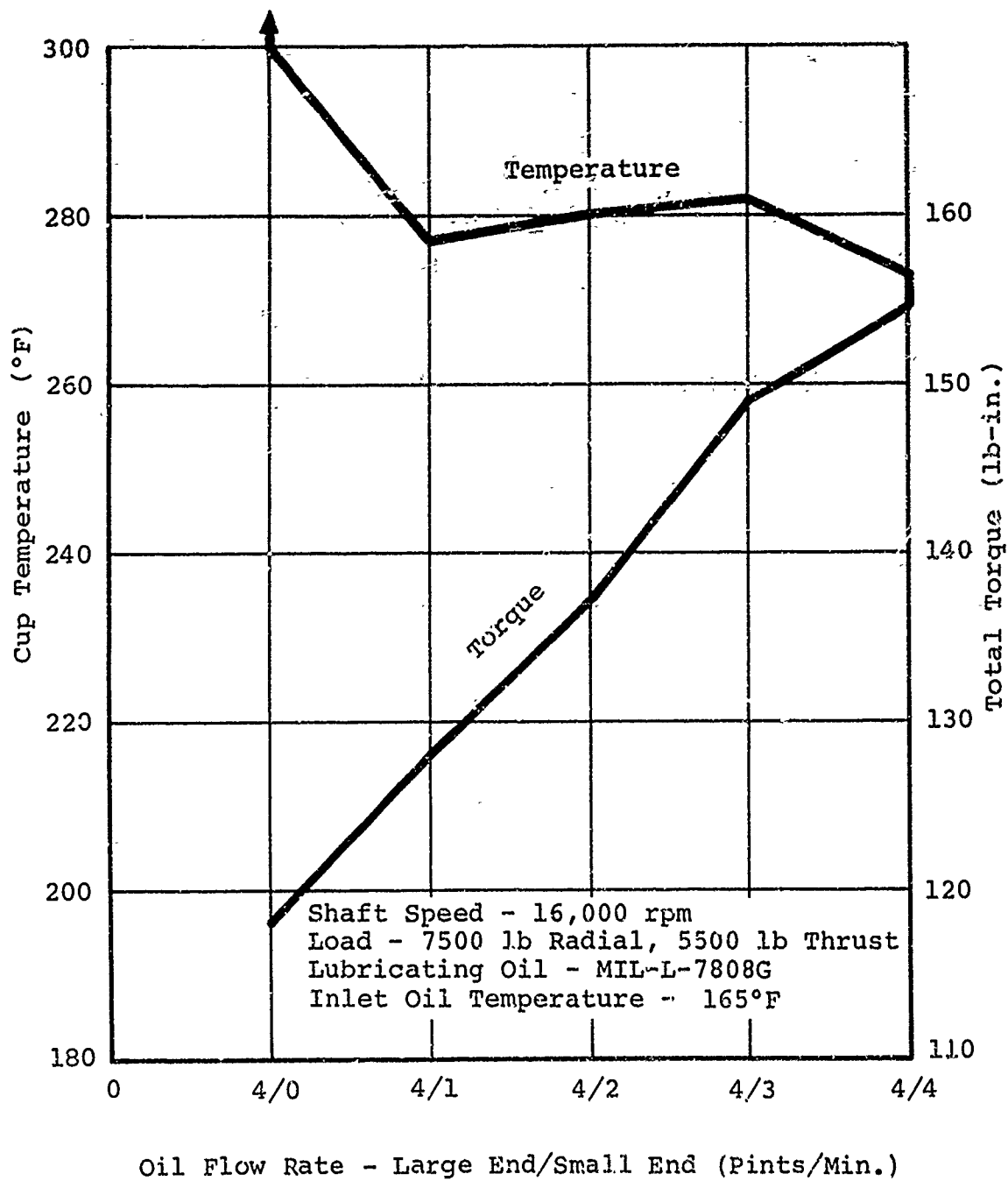
Figure 33 . Torque and Temperature Versus Oil Flow Rate
(Test 1, Bearing 1).
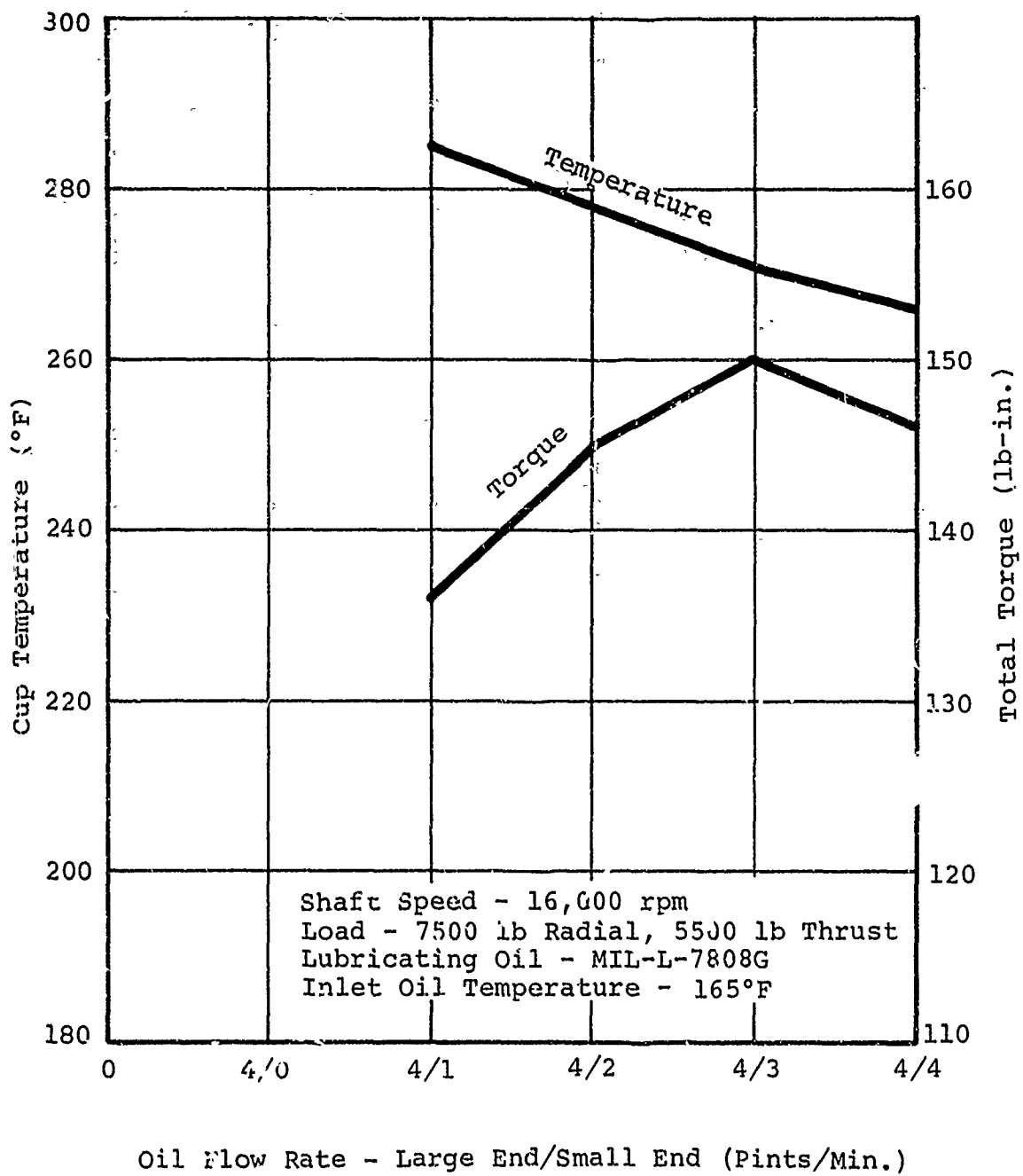
Figure 34. Torque and Temperature Versus Oil Flow Rate
(Test 3, Bearing 5).
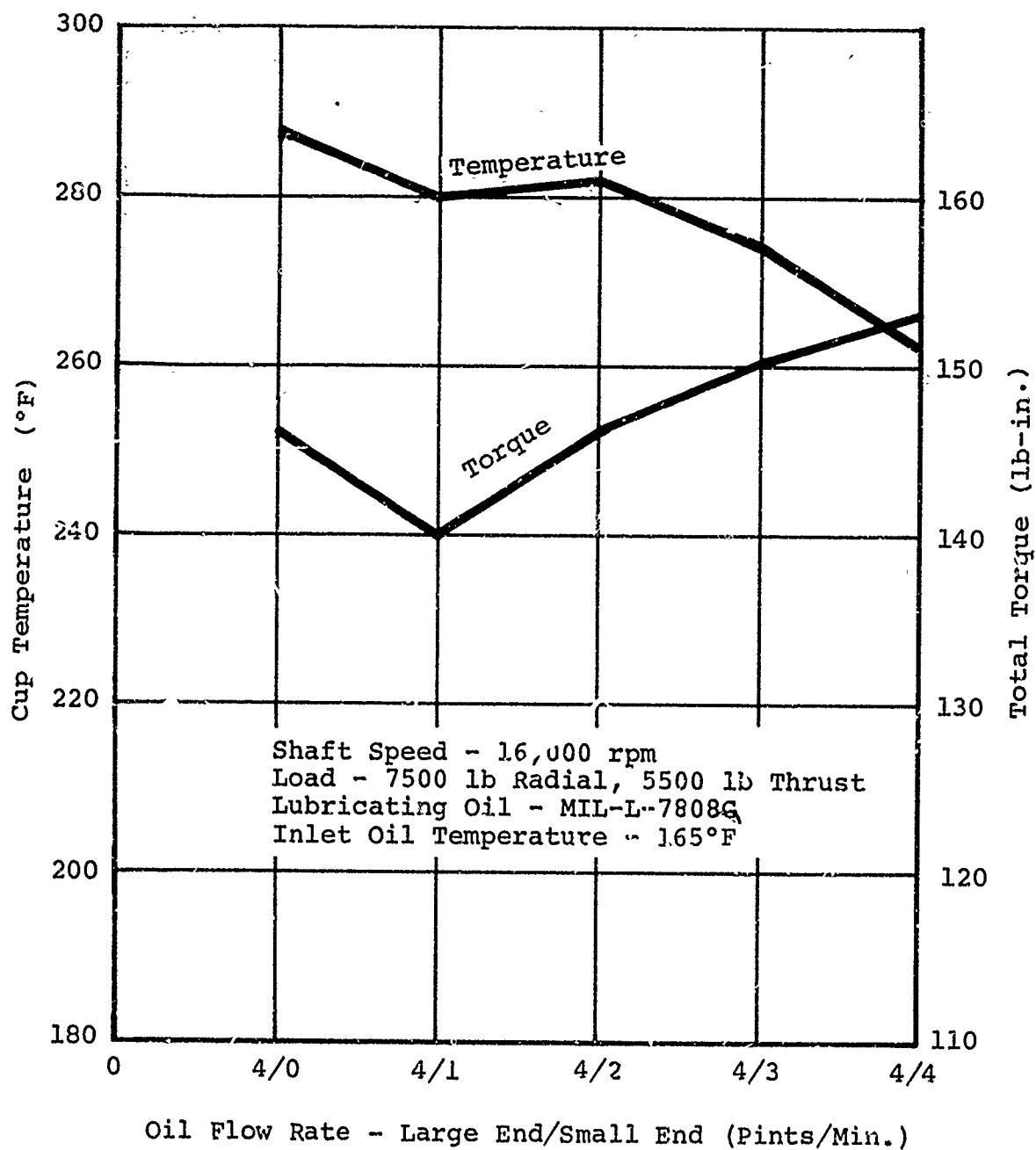
Figure 35. Torque and Temperature Versus Oil Flow Rate (Test 7, Bearing 13).
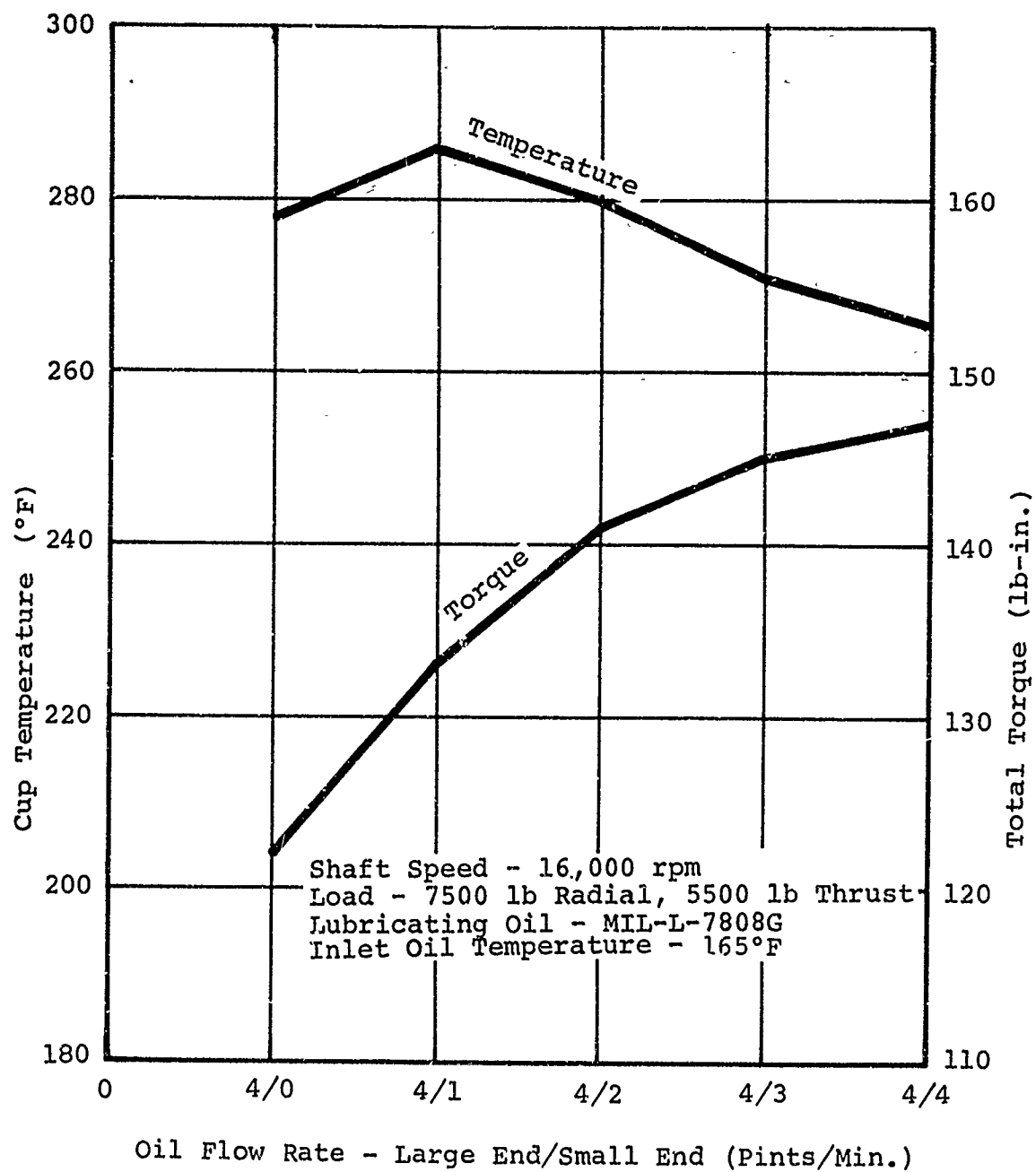
Figure 36.   Torque and Temperature Versus Oil Flow Rate
(Test 11, Bearing 21).
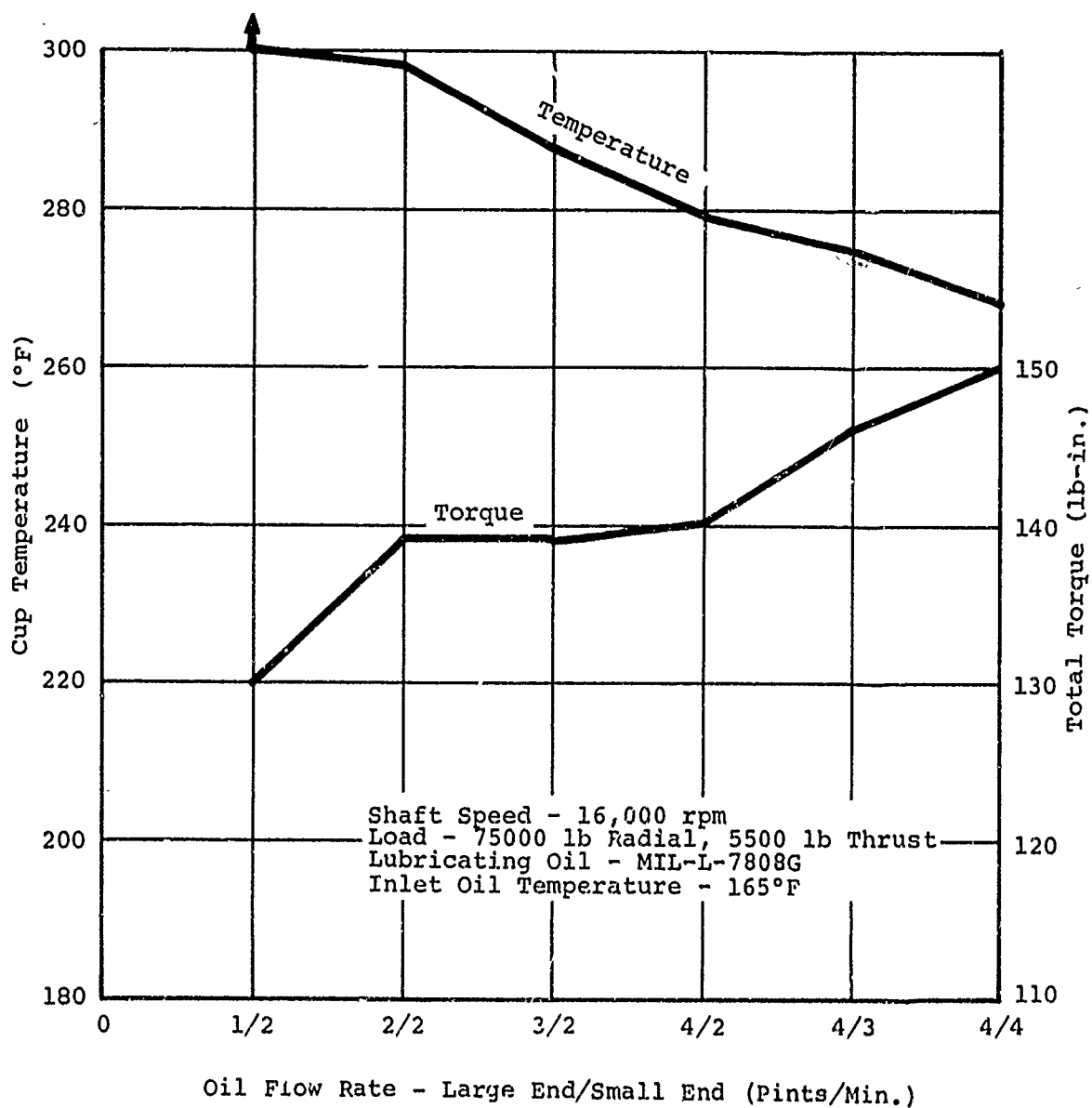
Figure 37. Torque and Temperature Versus Oil Flow Rate
(Test 8, Bearing 15).
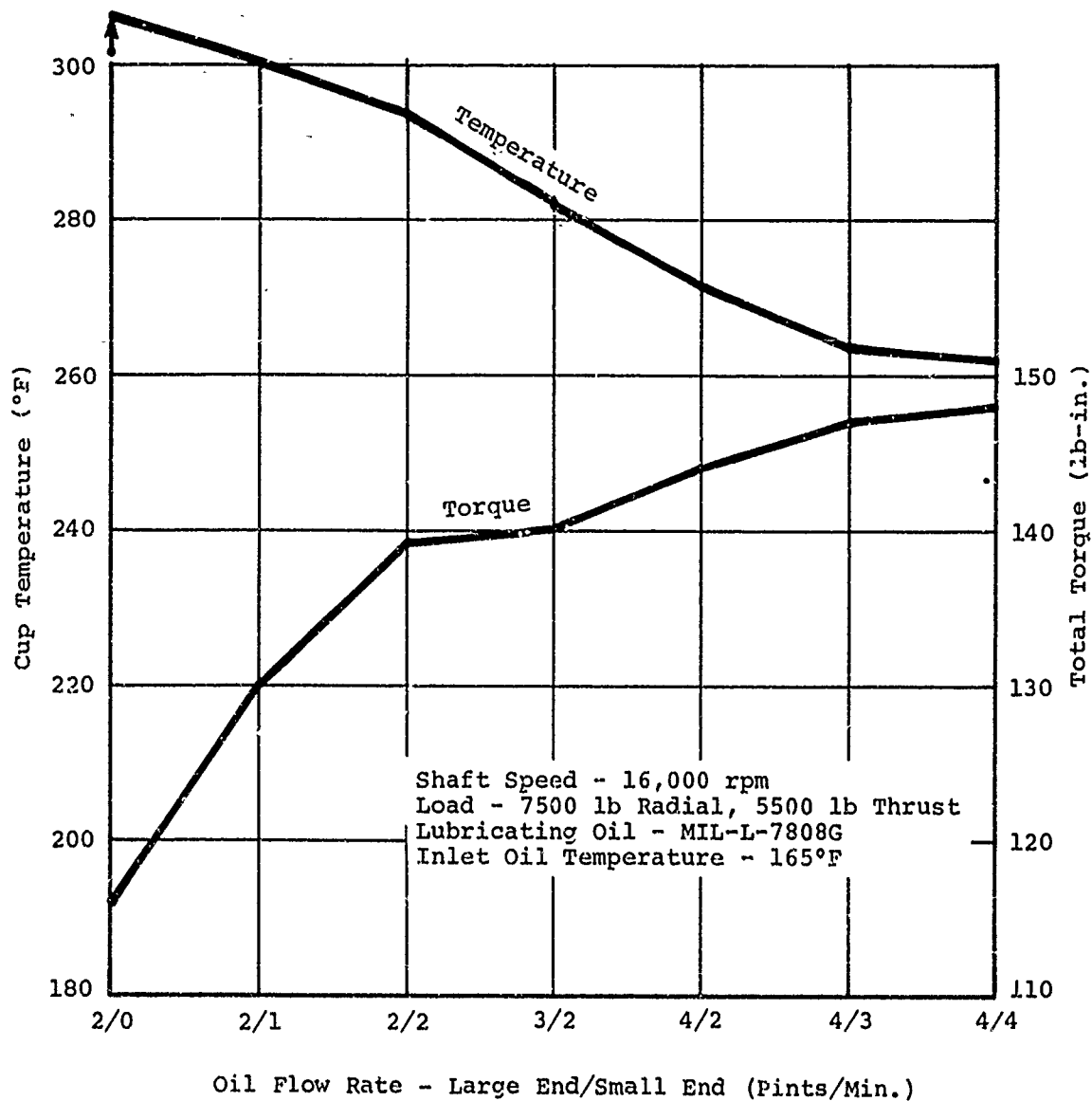
Figure 38. Torque and Temperature Versus Oil Flow Rate
(Test 12, Bearing 24).

65
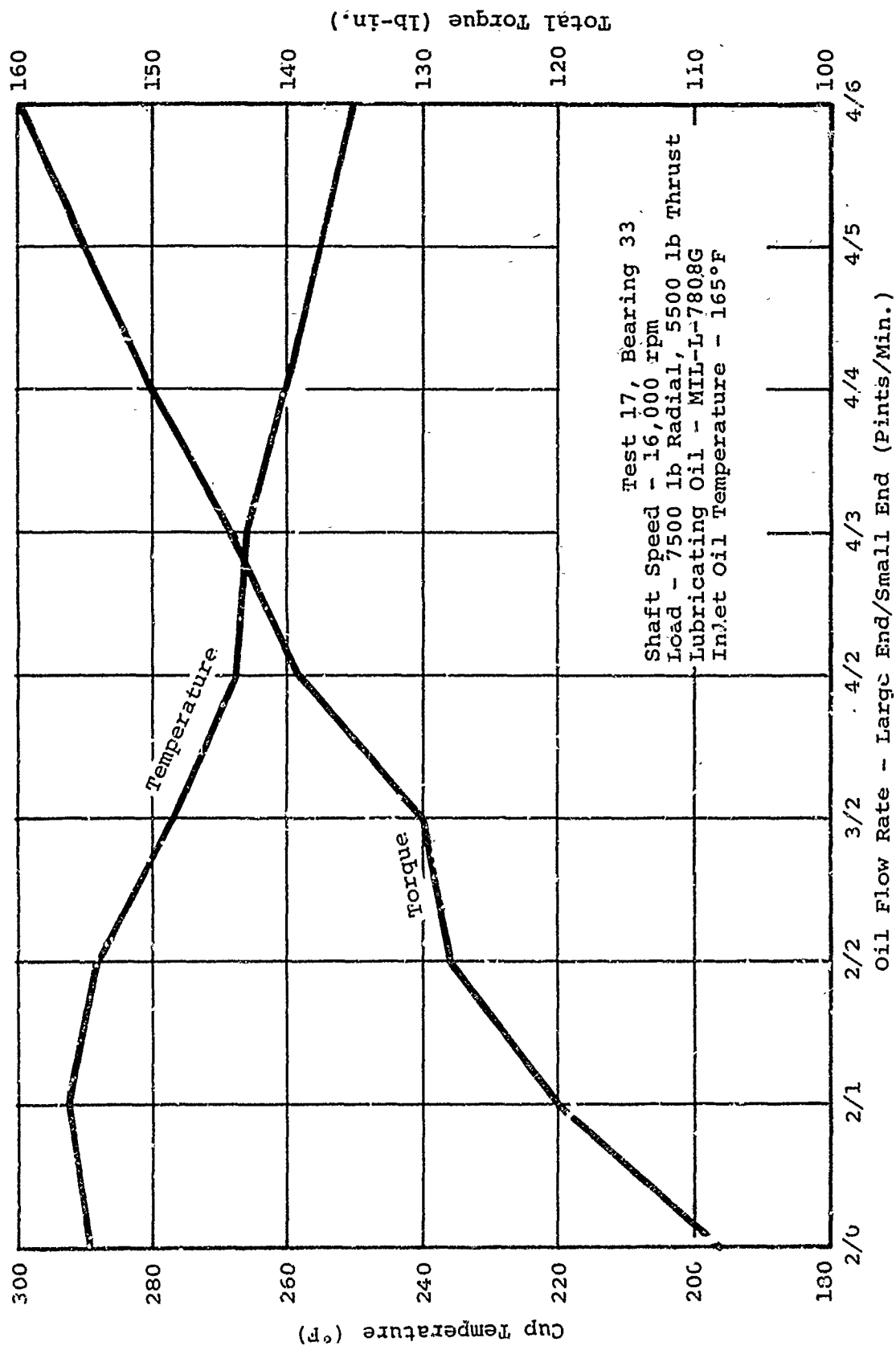
Figure 39. Torque and Temperature Versus Oil Flow Rate (Test 17, Bearing 33).

Test 17, Bearing 33
Shaft Speed – 16,000 rpm
Load – 7500 lb Radial, 5500 lb Thrust
Lubricating Oil – MIL-L-7808G
Inlet Oil Temperature – 165°F

Table II lists the oil-flow rates used in each test with the corresponding level-off condition data points (such as bearing cup temperature, test housing surface temperature, and total torque of the four-bearing test system). All of the level-off data points listed in this table were recorded after running at least 2 hours at the corresponding oil-flow rate test parameters.

Roller Spherical End Radii

Tests 3 and 4 (four bearings) were conducted with roller spherical end radii equal to 70 percent of the apex length. Test 3 ran at 16,000 rpm for 8 hours. The oil-flow rate to the small end of the bearing was reduced from 4 pints/ minute down to 1 pint/minute, while the oil-flow rate through the radial holes in the cone remained at 4 pints/minute. This test ran for 5 minutes at 16,000 rpm with no flow to the small end and 4 pints/minute through the radial holes in the cone before one of the bearings became damaged (see Figure 40). The torque was erratic during the acceleration and the loading-up period, as shown in Figure 41, as well as throughout the remainder of the test. Test 4 ran at 16,000 rpm for 2 hours with an oil-flow rate of 4 pints/minute to the small end and 4 pints/minute through the radial holes in the cone. While the oil-flow rate to the small end of the bearing was being reduced to 2 pints/minute, one of the bearings became damaged. The torque on this test was erratic, similar to that of Test 3.

Tests 5 and 6 with spherical end radii equal to 60 percent of the apex length could not be run at 16,000 rpm. In Test 5, bearing damage occurred at 15,000 rpm. Test 6 ran for 30 minutes at 16,000 rpm before bearing damage occurred. Both tests had erratic torque characteristics. Figure 42 is a section of the torque chart showing the erratic torque in Test 6.

The remainder of the test program was conducted with bearings with the roller spherical end radii equal to 80 percent of the apex length. Figure 43 is a section of torque-chart paper showing typical acceleration torque characteristics of bearings with 80 percent rollers.
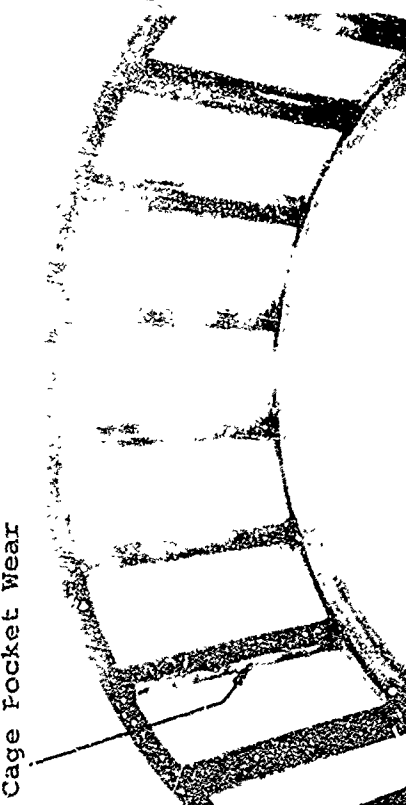
Previous Boeing-Vertol test work has shown that rollers with a radius greater than 80 percent of the apex length do not perform satisfactorily.

Table II lists the roller spherical end radius for each test bearing as a percent of the apex length.
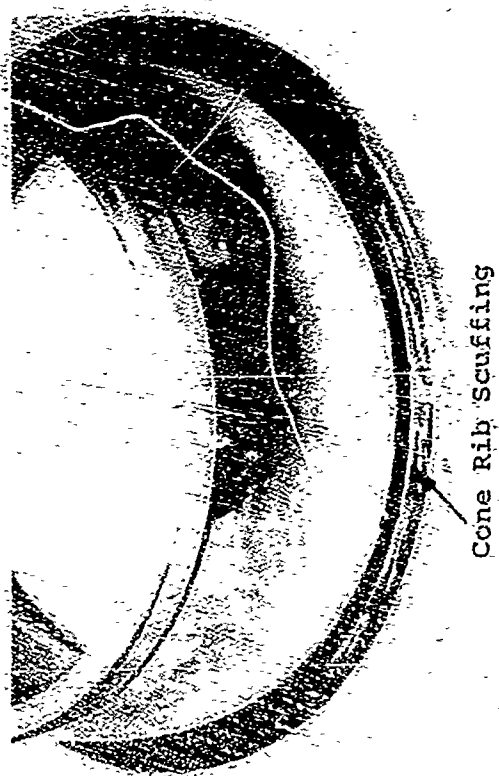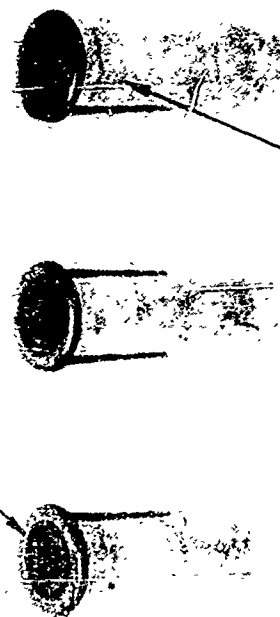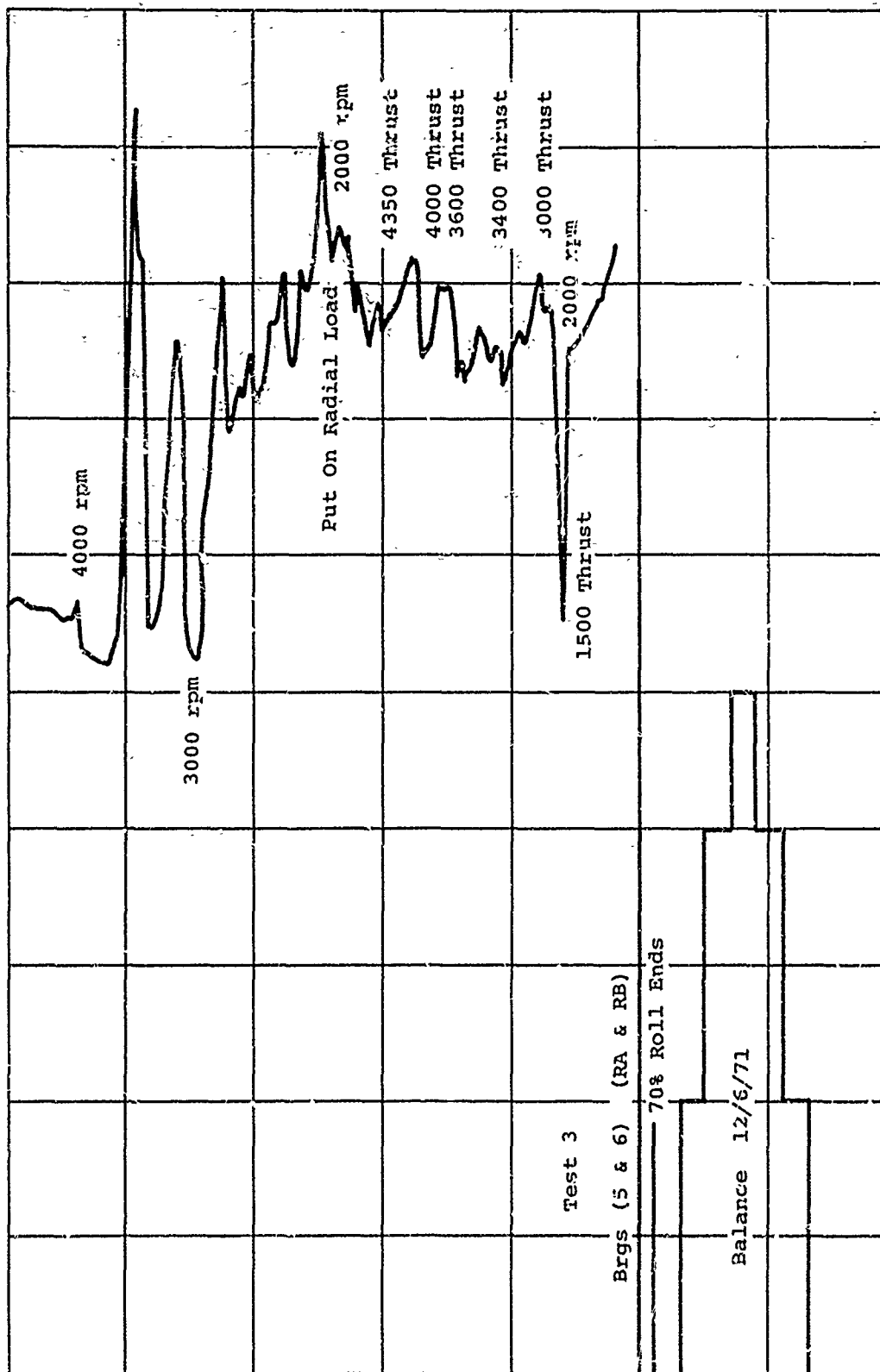
Cone Rib Scuffing

Roller Spherical
End Radius
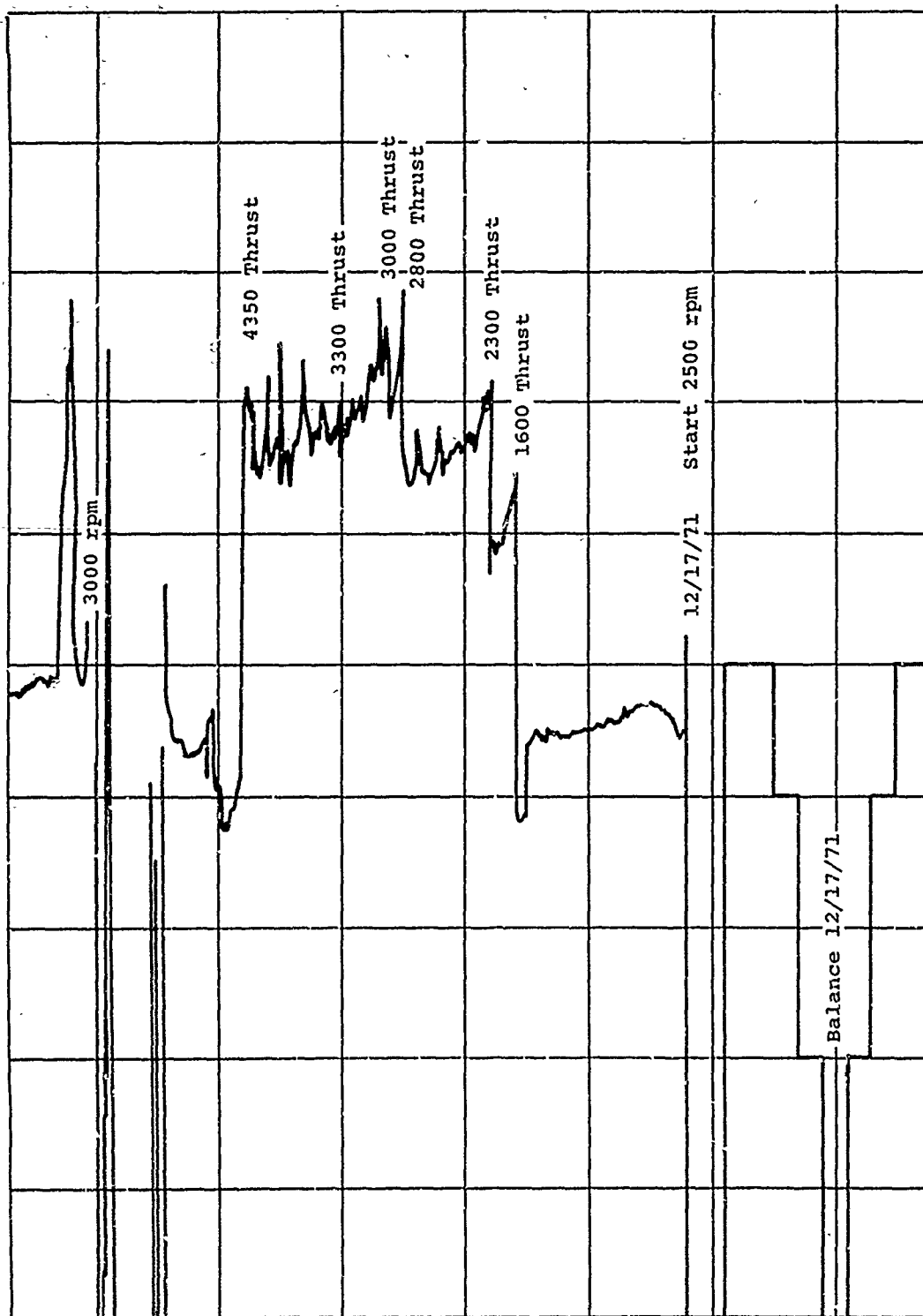
Roller Body Scuffing

Cage Pocket Wear

Bearing 83031-5, Test 3
Spherical End Radii = 70 Percent Apex Length
Note Roller-End/Cone-Rib Scuffing, Excessive Cage Wear and
Roller Body Scuffing

Figure 40. Damaged Bearing After Test.

Torque (lb-in.)

Figure 41. Erratic Torque of Bearings 5 and 6, Test 3.

Figure 42. Erratic Torque of
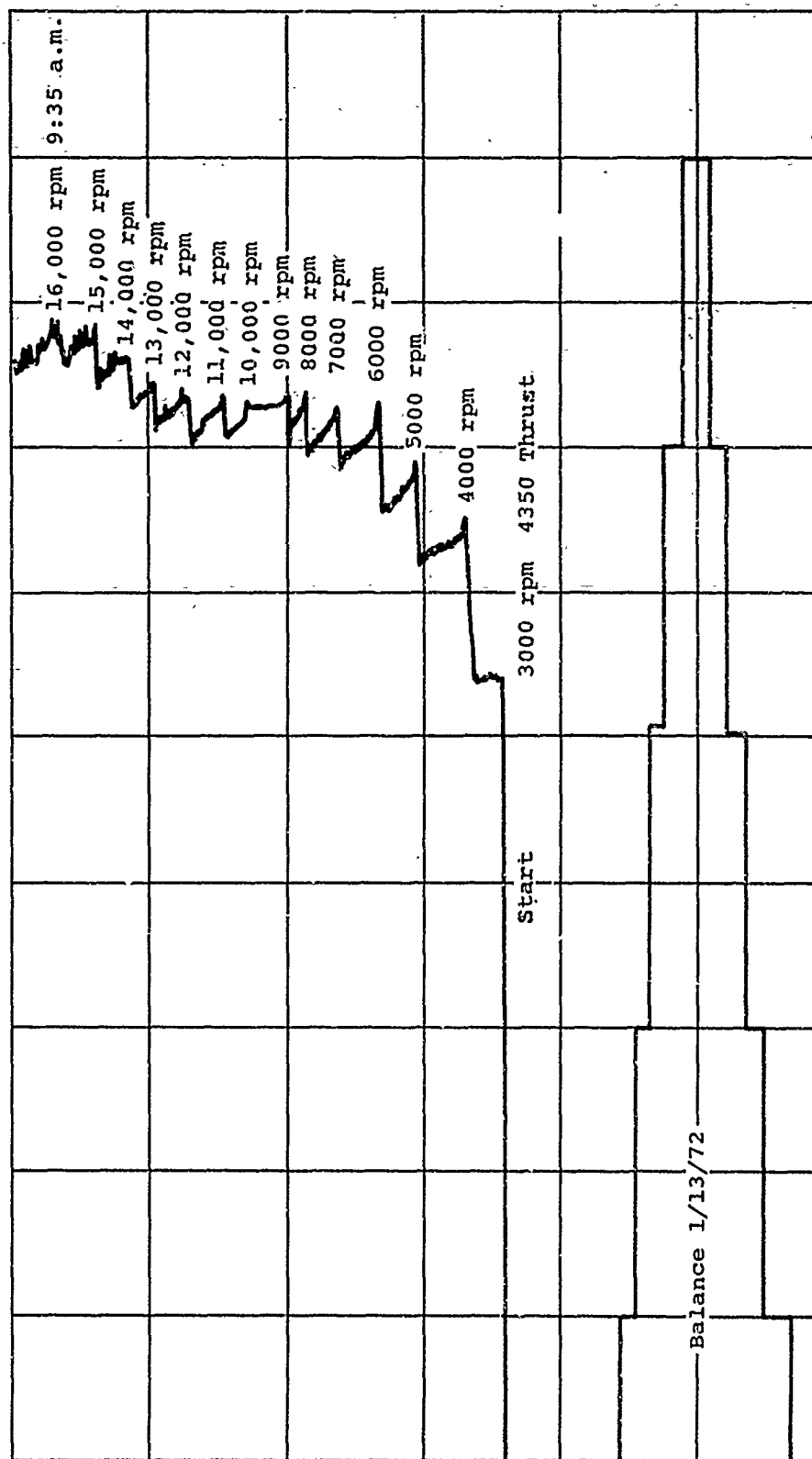Bearings 11 and 12, Test 6.

Figure 43.   Typical Torque Curve, Bearings 15 and 16
With Rollers Having Spherical End Radii
Equal to 80 Percent of the Apex Length.

71

## Bearing Cage Plating and Coating

Tests 1 through 6 were conducted with phosphate-coated cages that were flared to relieve roller body contact. Tests 7, 8 and 11 through 18 were conducted with cages having a silver plating from 0.001-inch to 0.002-inch thick. In Tests 9 and 10, the cages had a brass plating from 0.001-inch to 0.002-inch thick. Both the silver-plated and phosphate-coated cages performed satisfactorily at the optimum oil-flow rate of 4 pints/minute through the radial holes in the bearing large end and 2 pints/minute flow to the small end. In tests with bearings with phosphate-coated cages, when the oil-flow rate to the small end was reduced to 1 pint/minute or less, the cage pockets wore excessively, and the roller bodies became scuffed. Only one of the eight bearings with silver-plated cages that were tested with an oil-flow rate of 1 pint/minute or less developed excessive cage wear and scuffing of the roller bodies (see Figure 43). This would indicate that the silver-plated cage should have an advantage over the phosphate-coated cage in a marginal lubrication situation. Figure 44 shows how the silver plating separated from the cage. The tin strike that was applied before plating melted at high operating temperature and caused this separation. This problem was solved by applying a nickel strike before plating.

Bearings in Tests 9 and 10 had cages that were brass plated from 0.001-inch to 0.002-inch thick. These bearings could not be run at 16,000 rpm; however, the cages did not show any signs of damage or unusual wear patterns. It is suspected that the 18 radial holes from the backface chamfer (oil manifold) to the rib undercut are not adequate for a good distribution of oil to the rib face and, therefore, caused these bearings to become damaged.

Surface Finish

Table IV lists the bearing cone rib face, cone race, roller body, and roller spherical end radius surface finish measurements before and after testing. The bearing cone race and rib face finish measurements as shown in Table IV were taken after standard double etching. They ranged from 4 to 18 microinches (AA) as measured by a Brush-Instrument Surfindicator, Model No. MS 1300-01.

Cone rib face traces were taken on cones before and after standard double etching by a Clevite 1200 Surfanalyzer System (see Figure 45). This investigation showed that the finishes after etching were twice those of the before-etched cone. A fine steel wool was used to remove the

72
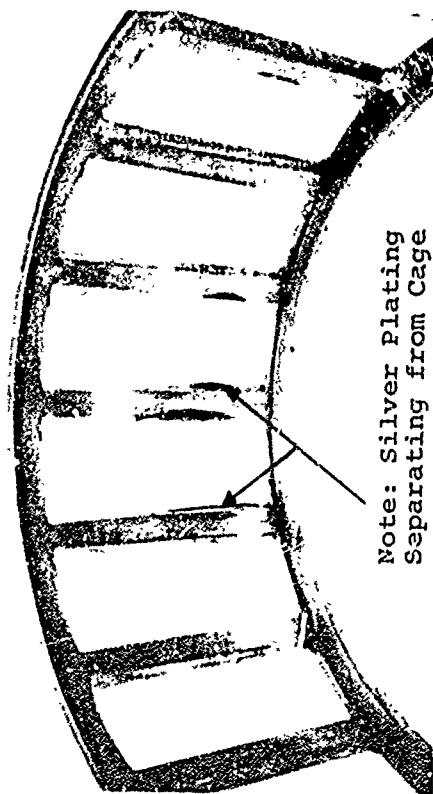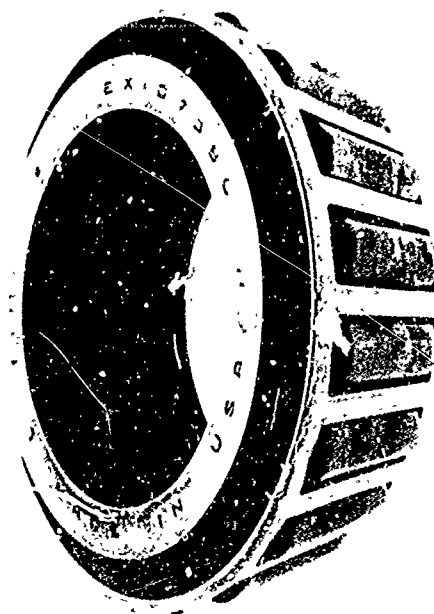
Note: Silver Plating
Separating from Cage

Bearing 83031-14, Test 7
Note Separation of Silver Plating from Cage Due to Tin Strike Melting.
Plating Procedure was Changed to Nickel Strike, Silver Strike,
and then Silver Plating.

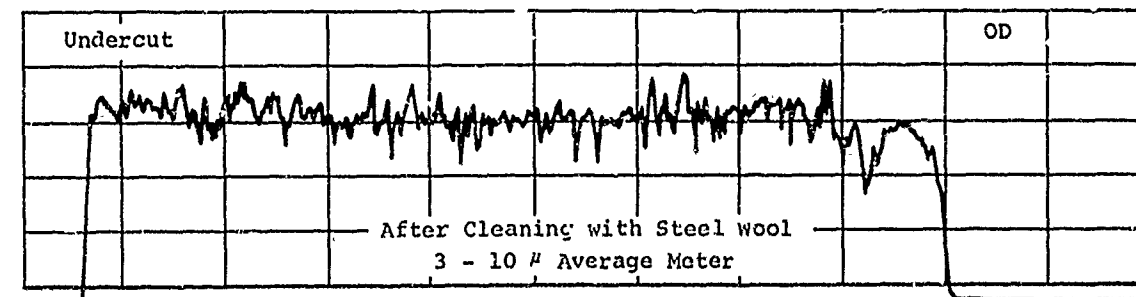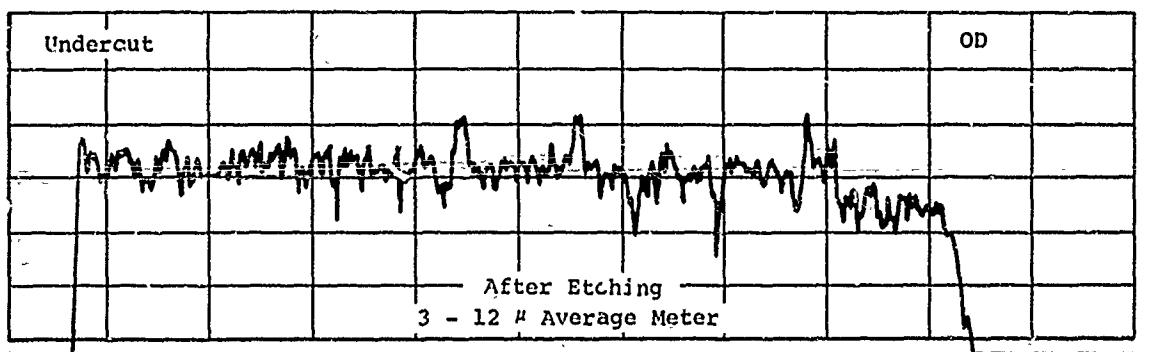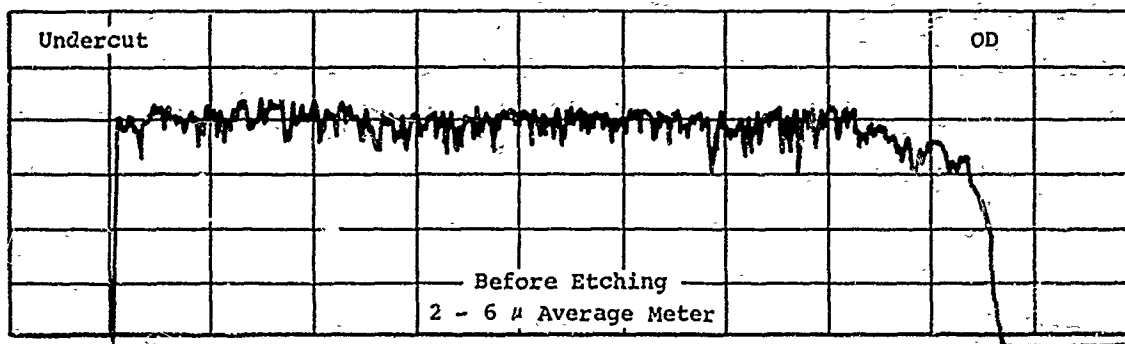Figure 44.   Damaged Bearing After Test.

73

Figure 45. Rectilinear Traces of Cone Rib Face Showing Surface Finish.

74

dark residue produced by the standard double etching. This reduced the surface finish measurements by 17 percent. In addition, two bearings were run in the test machine for 5 hours at 16,000 rpm under 7500-pound radial and 5500-pound thrust load. The rib face finishes on the 2 bearings before test were 10 to 13 and 13 to 19 microinches. The surface finish measurements after test were 3 to 7 and 3 to 9 microinches, respectively.

The above discussion shows that the rib face and cone race surface finish measurements are, in fact, half of those shown in Table IV.

Cage Design

The test results have shown no apparent difference between cages that are flared to relieve roller body contact (see Figure 13) and standard stamped-steel cages. Most of the tests were conducted with flared cages. Tests 10, 13, 14, 17, and 18 were conducted with standard stamped-steel cages. None of the standard stamped-steel cages had excessive wear or roller body scuffing after test. The excessive cage wear and roller body scuffing that occurred in bearings with flared cages were caused by the reduced oil-flow rate to the small end of the bearing.

Tests 13 and 17 were conducted with standard stamped-steel silver-plated cages. Bearings from Test 13 could not be run at 16,000 rpm successfully. This test was rerun three times; each time the rib of the damaged bearing was reground and new rollers were used. There was no evidence that the standard stamped-steel cages caused the bearing damage. It is suspected that 18 radial holes through the cone were not adequate for a good distribution of oil, and this caused the premature failures. Test 17 ran satisfactorily at 16,000 rpm.

Number of Holes Through Cone

Although there was no measurable difference between bearings with cone designs having 18 and 24 radial lubrication holes, the occasional cone-rib/roller-end scuffing indicated that 18 holes were not adequate for good distribution of the lubricating oil.

Thirteen of the twenty-four bearings with 18 radial holes in the cone were damaged during testing. Only one of the 12 bearings with 24 radial holes in the cone was damaged during testing. There is no apparent explanation for this failure, since the remaining 11 bearings ran well.

Verification Testing

Full Radial and Thrust Load Tests

Tests 14, 15, 16, and 18 were run with optimized parameters as verification tests. These tests were run at 16,000 rpm for 24 hours with 4 pints/minute oil flow through 24 radial holes in the cone and 2 pints/minute oil flow to the small end of the bearing. The applied external load was 7500 pounds radial and 5500 pounds thrust. The bearings had rollers with spherical end radii equal to 80 percent of the apex length. Tests 14 and 18 were run with bearings having silver-plated standard stamped-steel cages, and Tests 15 and 16 had bearings with cages that were silver plated and flared.

Bearing 30 from Test 16 was damaged before reaching 16,000 rpm. Bearing 34 from Test 16 was later tested with bearing 35 from Test 18; therefore, bearing 35 accumulated 48 hours by the conclusion of this test program.

Reduced Radial and Thrust Load Tests

The bearings that were tested with reduced radial and thrust loads were run after the completion of two of the 24-hour full-load verification tests (Numbers 15 and 18). At the end of these two tests, the bearings were disassembled and inspected before reinstalling for the reduced load testing. The 80 percent load tests were run for 8 hours at 16,000 rpm with the optimum oil-flow rate of 4 pints/minute through the cone and 2 pints/minute to the small end.

The bearings tested under 60 percent of the radial and thrust load became damaged upon reducing the loads to 60 percent. This damage would not occur in an actual application. Table V is an analysis of the loading on the 6500-series bearing. Due to the design of this type of test machine (Figure 46) where the external thrust load is applied through the cup or outer race, it must be greater than the internal load due to centrifugal force, plus the induced thrust reaction from the radial load. Otherwise, the internal loads will back out the external thrust loading device and unseat the bearings. This is not the case in the normal gearbox application, where the cone is fixed on the shaft and the cup is fixed in a housing to resist the separating force of the internal loads and cannot be backed out (see Figure 47).

TABLE V. ANALYSIS OF LOADING FOR REDUCED
RADIAL AND THRUST LOAD TESTS

Test Load (pounds)		Percent Load	Axial Component of CF		Induced Thrust .47R/K		Sum	Test Load Thrust Divided by Sum x 100
Radial	Thrust							
7500	5500	100	2581	+	2414	=	4995	110.1
6000	4400	80	2581	+	1932	=	4513	97.5
4500	3300	60	2581	+	1449	=	4030	81.9

Axial Component of Roller CF

CF is Reacted on the Outer Race Resulting in Normal and Thrust Load. Summation of Thrust Load at each Roller Counteracts the Applied Thrust Load. Load is Constant for each Speed Setting.

Thrust Load is Applied Through Cup. In Actual Operation, Thrust Load is Applied Through Cone.

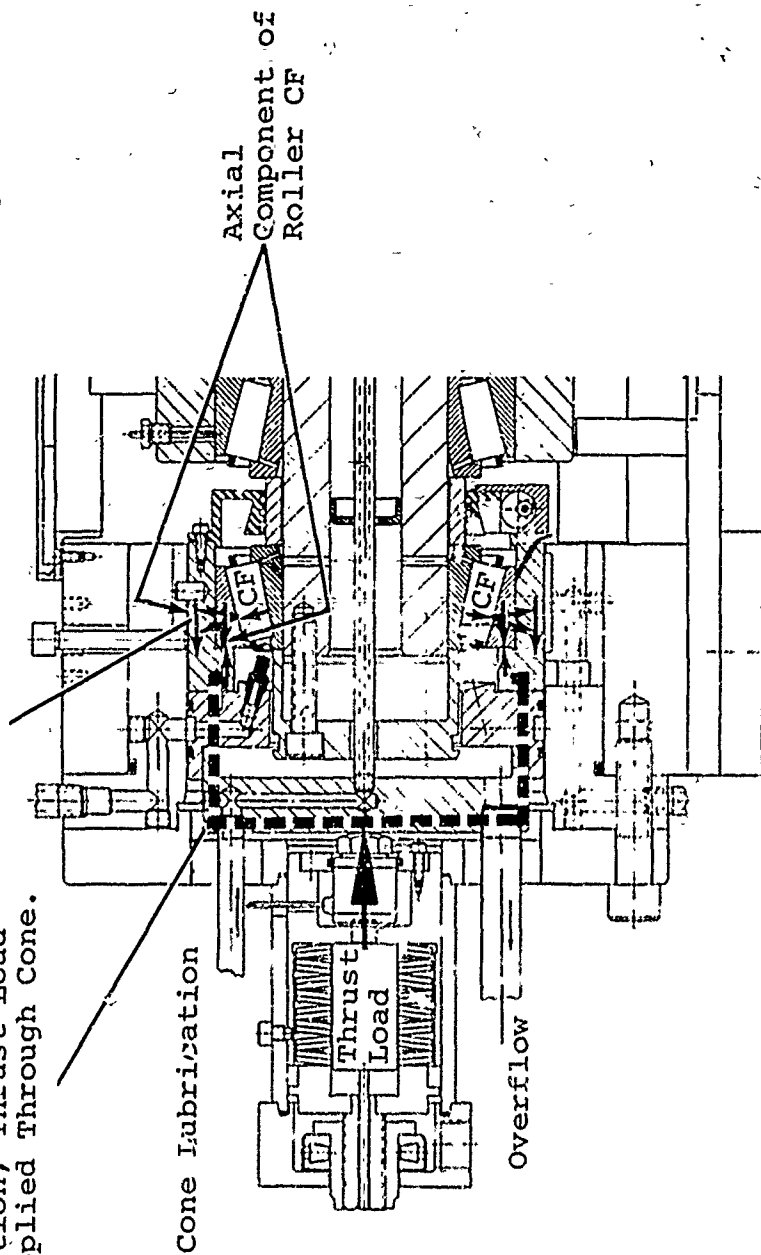Cone Lubrication

Thrust Load

Overflow

Figure 46. Loading Diagram for Test Rig.

Gear Thrust Load is
Applied Directly to
the Bearings.

Axial Component of CF
Bearings is Axially Locked;
Therefore, Axial Component
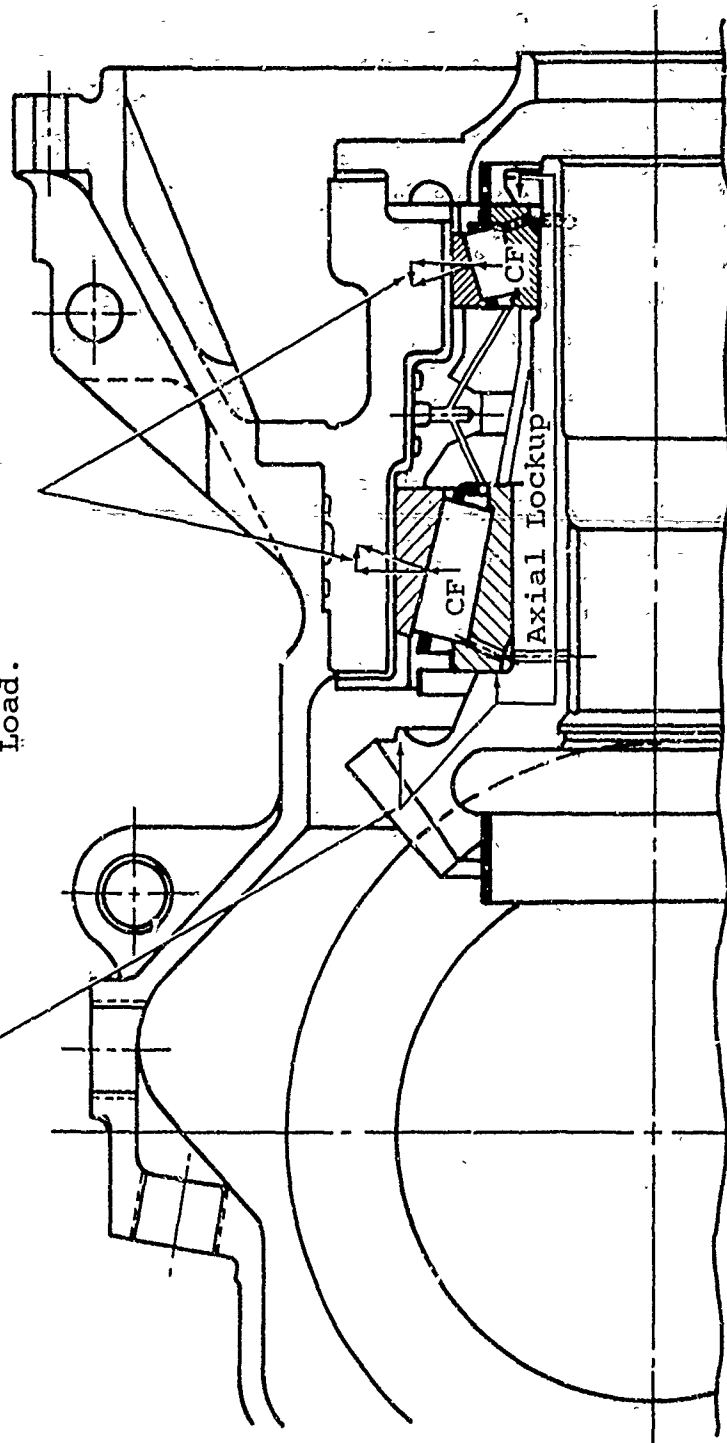Reacts Against Housing and
Results in Additive Internal
Load.

CF

CF

Axial Lockup

Figure 47. Loading Diagram for a Typical
Transmission Application.

79

Radial-Load-Only Tests

Bearing 83031-RA was run in the drive-end-center radially loaded position and accumulated 209 hours during this test program. Bearing 83031-RB was tested in the opposite drive-end-center radially loaded position and accumulated 60 hours during the program.

Fail-Safe Testing

Table VI is a summary of visual inspections made on the fail-safe bearings after Test 19 and 20. Figures 48 through 51 show the after-test condition of the fail-safe bearings. This test ran for 15 minutes at 9000 rpm before excessive torque caused the test machine drive to stop. After test, inspection showed that the two bearing cones with the DuPont Vespel SP-21 rib inserts were pitted. One of the Vespel SP-21 rib inserts broke loose and turned on the cone.

The bearings with DuPont T-400 and Borkote applied to the cone ribs appeared satisfactory after running at 9000 rpm for 15 minutes. There was gross wear on the large end guiding flange of the centerline contact cage where this flange contacts the bearing cone rib outside diameter. This was due to lubricant starvation in this area. A high speed movie plus strobe-light still photographs substantiated the lubricant starvation problem (see Figure 52).

The two bearings with the T-400 and Borkote applied to the ribs were modified by drilling four radial holes from the bearing cone backface chamfer to the bearing cone large-end rib outside diameter to lubricate the area where the cage inside diameter contacts the cone rib outside diameter, and to provide an oil film to help center the cage. One of the cages was modified to include four 1/8-inch-radius notches filed in the cage flange inside diameter (see Figure 53). These bearings were tested to observe the cage lubrication at various speeds with a strobe tachometer. The bearing with the 1/8-inch-radius notches was damaged after running a short time at 16,000 rpm (see Figure 53). It was concluded that the notches allow too much lubricant to escape through the radial holes in the cone, thereby starving the roller/cone-rib contact.

Bearing 83031-39 with the T-400 rib, standard rollers, and silver-plated machine-steel race-guided centerline cage was run in the center radial-load-only position for the remainder of this program. At the end of the program,

80

Bearing Ser No 83031-	Cone Rib	Roller Large End	Machined Race-Guided Centerline Contact Cages
	TABLE VI. SUMMARY OF VISUAL INSPECTIONS OF FAIL-SAFE BEARINGS AFTER TEST		
37	VESPEL SP-21	STANDARD	SILVER PLATED
	Rib insert broke loose and turned	Undamaged	Gross wear 90% in ID large end flange; several pockets show harder contact than others
38	VESPEL SP-21	STANDARD	BORKOTE
	Rib face pitted	Cage has marked roller spherical ends	Cage pockets show uneven wear; heavy toward large end
39	T-400	STANDARD	SILVER PLATED
	Undamaged	Undamaged	Silver plate peeled leaving flakes of silver in sides of pockets; some pockets show wear at small end
40	BORKOTE	BORKOTE	BORKOTE
	Undamaged	Undamaged	Gross wear 90% in ID large end flange

Vespel SP-21
Rib Insert
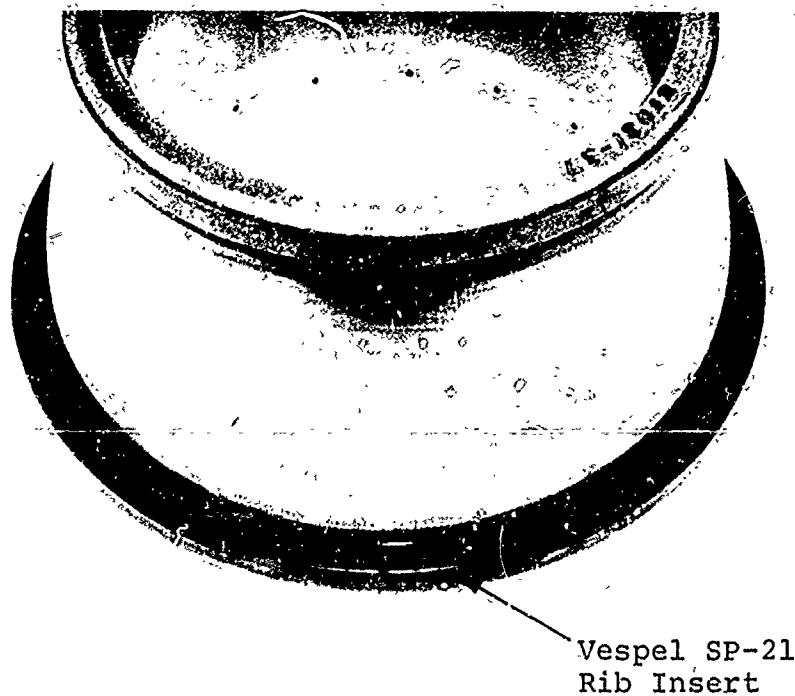
Bearing 83031-37, Test 19-20
Vespel SP-21 Rib Insert Broke Loose and Turned on Cone.
Bearing Ran for 15 Minutes at 9,000 rpm Before Bearing
    Damage Occurred.

Figure 48. Damaged Bearing After Test.

82

— Pitted
Area
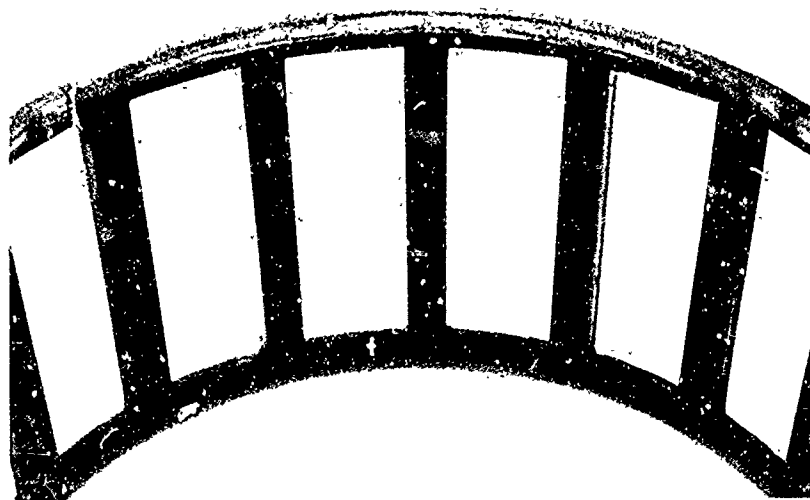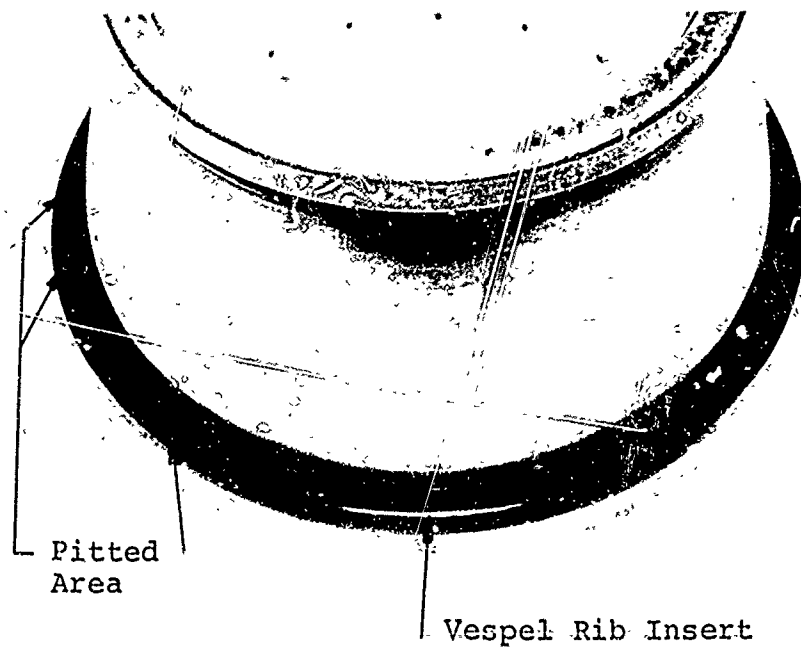
— Vespel Rib Insert

Bearing 83031-38, Test 19-20
Note Pitting of Vespel SP-21 Rib Insert; Cage is Borkote Treated.
Bearing Ran for 15 Minutes at 9,000 rpm Before Bearing Damage
        Occurred.

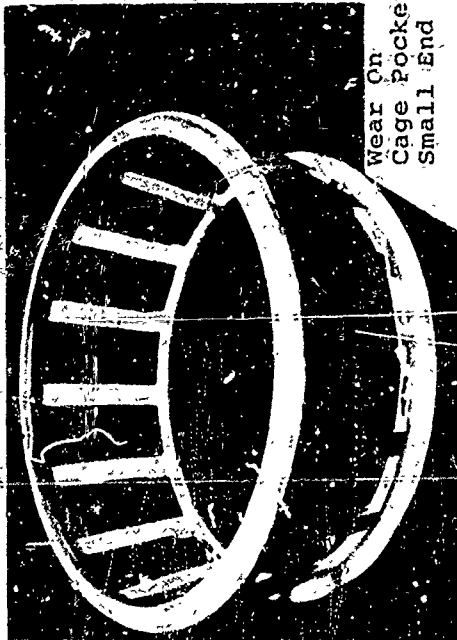Figure 49. Damaged Bearing After Test.

Wear On
Cage Pocket
Small End

Wear at Cage Small End Pockets

Roller Body
Cage Pocket
Contact Area

Silver Plating Flakes in Sides of Cage
Pockets

Slight Wear Path on Rib OD

Roller
Spherical
End Radius

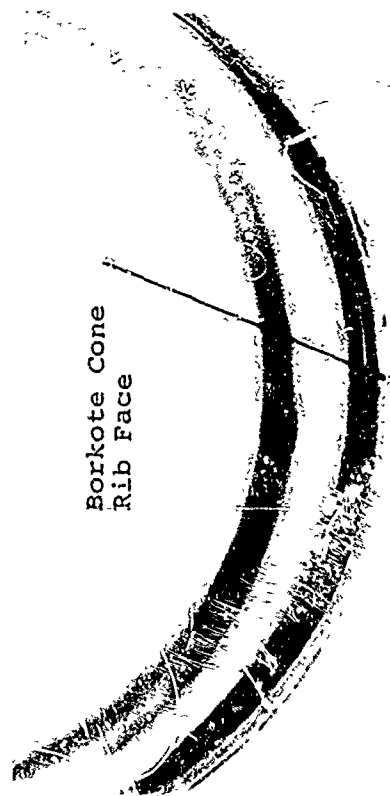Condition of Standard Roller Ends
After Running on T-400 Cone Rib

Figure 50. Bearing 83031-39 After Test 19-20.

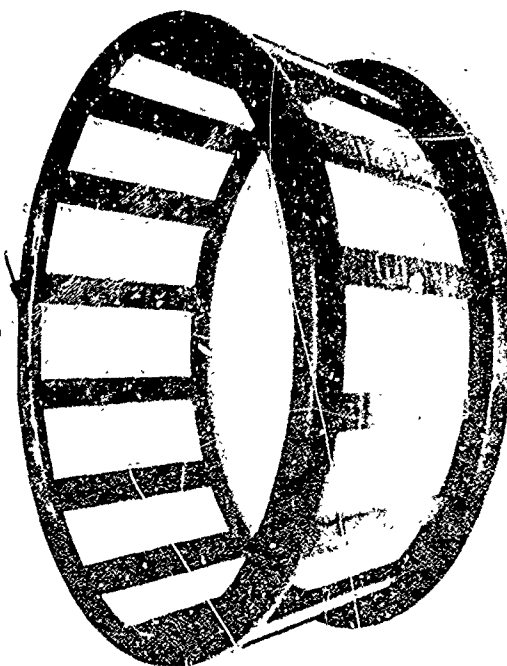84

Borkote Cone
Rib Face

Cone Rib After Test
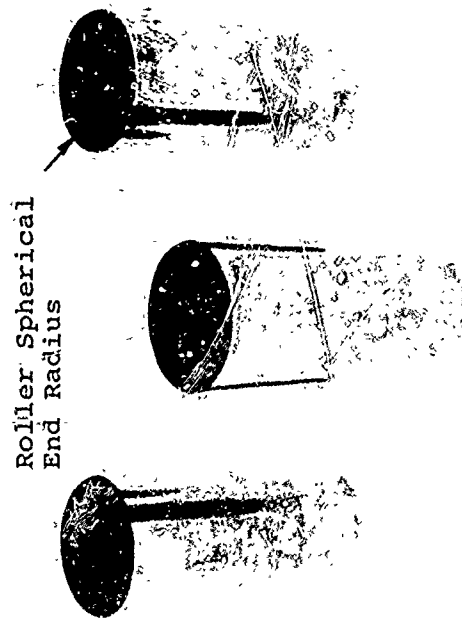
Roller Spherical
End Radius

Roller Ends After Test

Cone Rib Outside Diameter
Excessive Wear on the Cone Rib OD
Excessive Wear on Cage Inside Diameter

Excessive Wear on Cage ID

Figure 51.   Bearing 83031-40 After Test 19-20.

85
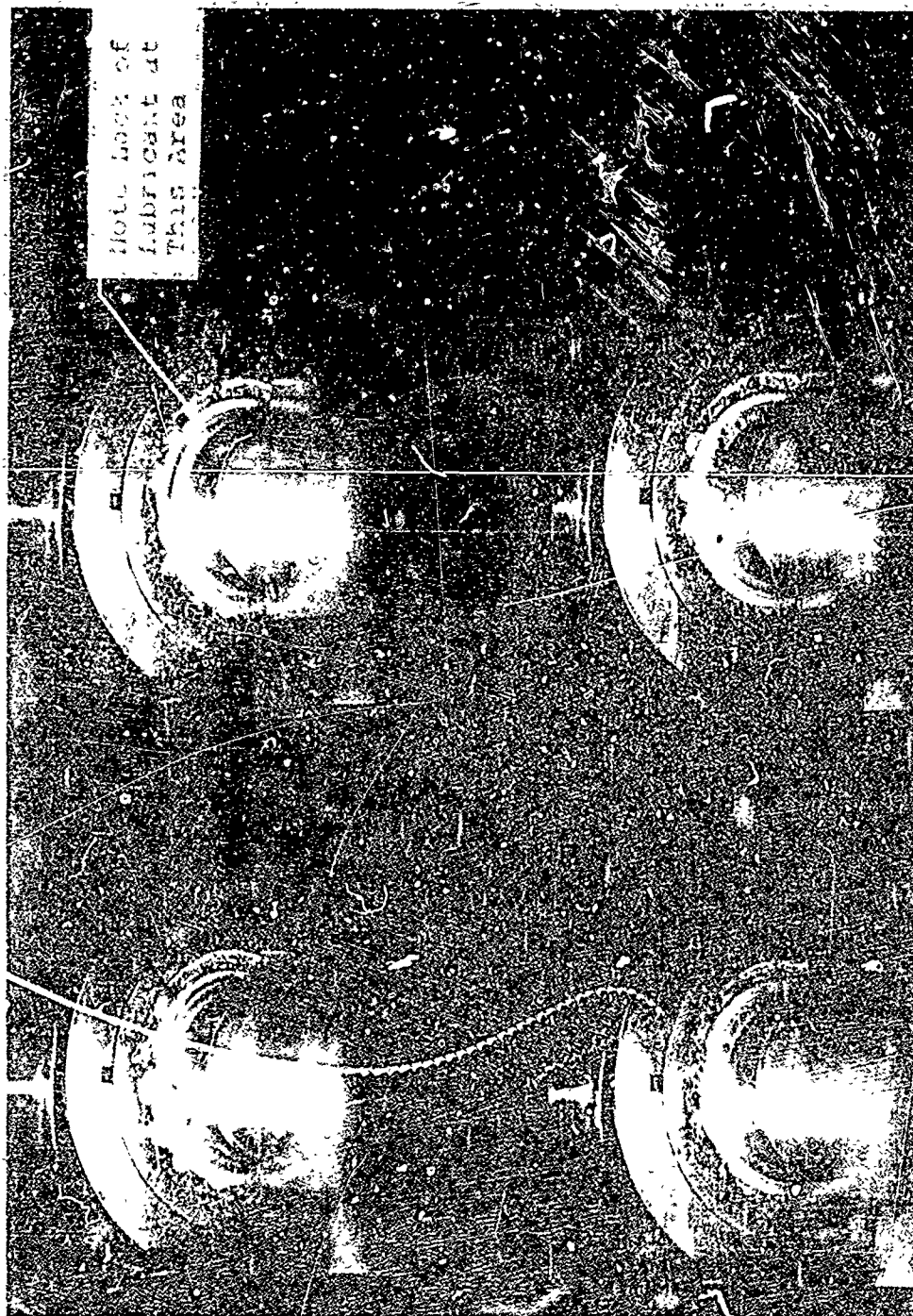
Figure 52. Bearing 83031-40 Running at 5000 rpm Showing the Absence of Lubricant Between the Cage ID and Cone Rib OD.

Four Additional Lube
Holes for Cage Riding
Land Lubrication

1/8-Inch Radius Notch
Filed in Cage Four Places
90° Apart

Slight Rib Scuffing

Figure 53. Bearing 83031-39 After Additional Fail-Safe
Testing to Provide Lubrication to Cage
Riding Land Surface.

this bearing had accumulated 149 hours at 16,000 rpm. Additional testing of bearing 83031-40 with the Borkote-treated rib, Borkote-treated roller spherical ends, and machined Borkoted cage was stopped because the Borkote-treated cage scored and pitted the roller ends.

ANALYTICAL AND EXPERIMENTAL RESULTS

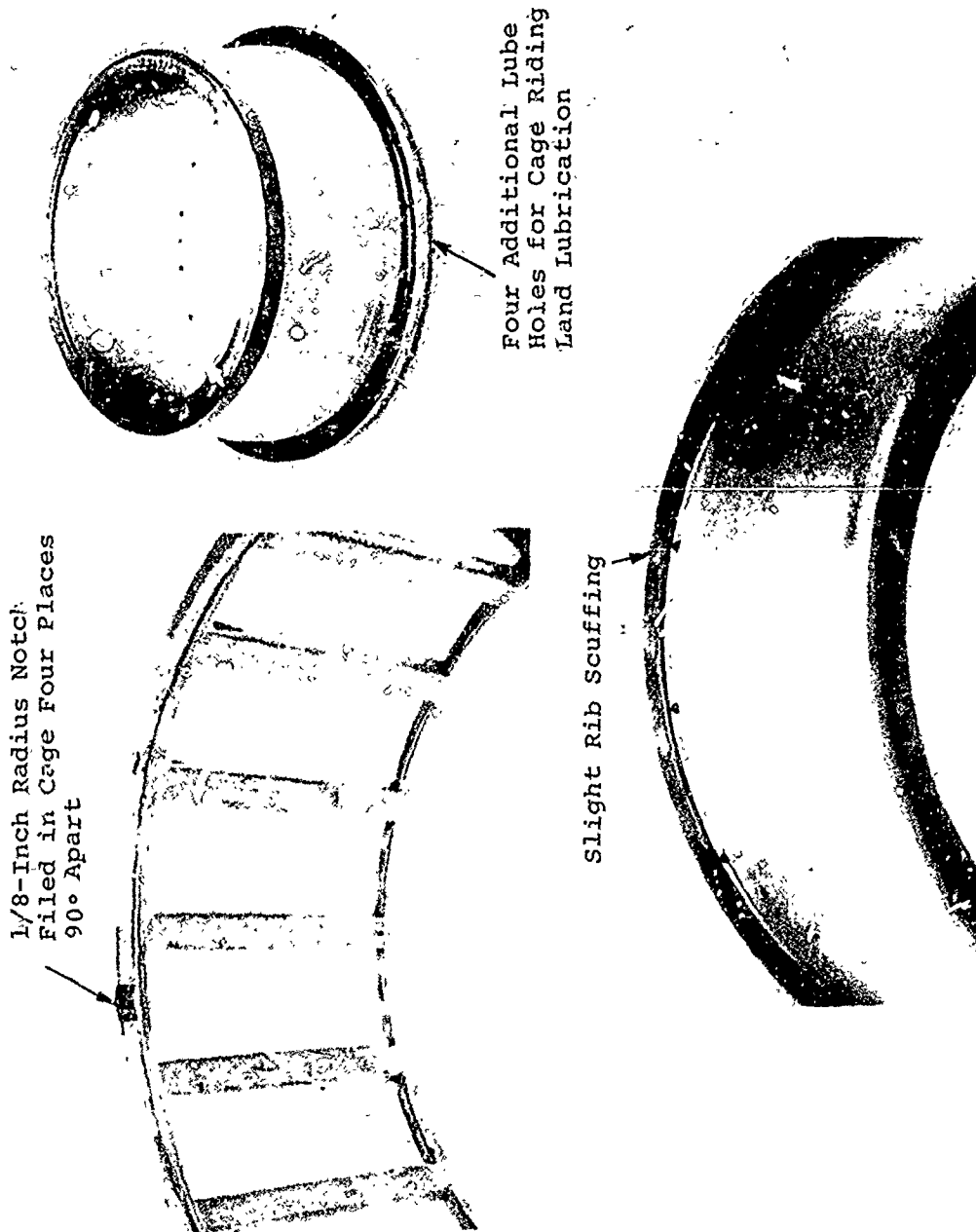Many of the experimental test results were predicted by the
analytical study conducted in conjunction with the experi-
mental investigation. Several parametric studies were
conducted and compared to the experimental data in order to
establish design criteria for future applications. The
various studies conducted during this program are summarized
below along with significant correlations.

The one geometric parameter that greatly influenced the oper-
ation of the tapered roller bearing was the spherical end
radius on the large end of the rollers. This spherical end
radius is generated by a vector which is less than the bear-
ing apex length. For standard bearings, this radius is
maintained at approximately 97 percent. Initial testing of
the bearings with the 97 percent radius showed that as speed
was increased, insufficient oil film was developed at the
roller-end/cone rib contact, resulting in scuffing failures.
Testing showed that by decreasing the spherical radius, a
wedge opening was obtained which permitted the development of
an oil film at the contact interface. The first phase of
this program was to experimentally and analytically evaluate
the effect of varying the spherical end radius on the perfor-
mance of a high-speed, tapered roller bearing. This series
of tests and past testing demonstrated that a spherical end
radius of 75-80 percent provided the best bearing performance.
Analytical parametric studies also showed that the optimum
spherical end radius for best film thickness generation is
80 percent of the apex length (Figure 54).

Decreasing the spherical end radius below 75 percent has
resulted in erratic bearing performance and cone rib scuffing.
In addition to reducing the film thickness, the contact stress
and the flash-temperature rise in this contact area increase
(Figures 55 and 56), which further increases the possibility
of failure. A further review of the analytical data indicated
that the film thickness at the roller-end contact should be
sufficient to ensure complete separation of the roller and
the rib; therefore, it is apparent that other factors are
influencing the performance.

Prior Boeing-Vertol development work in tapered roller
bearings demonstrated that the major cause of roller-end
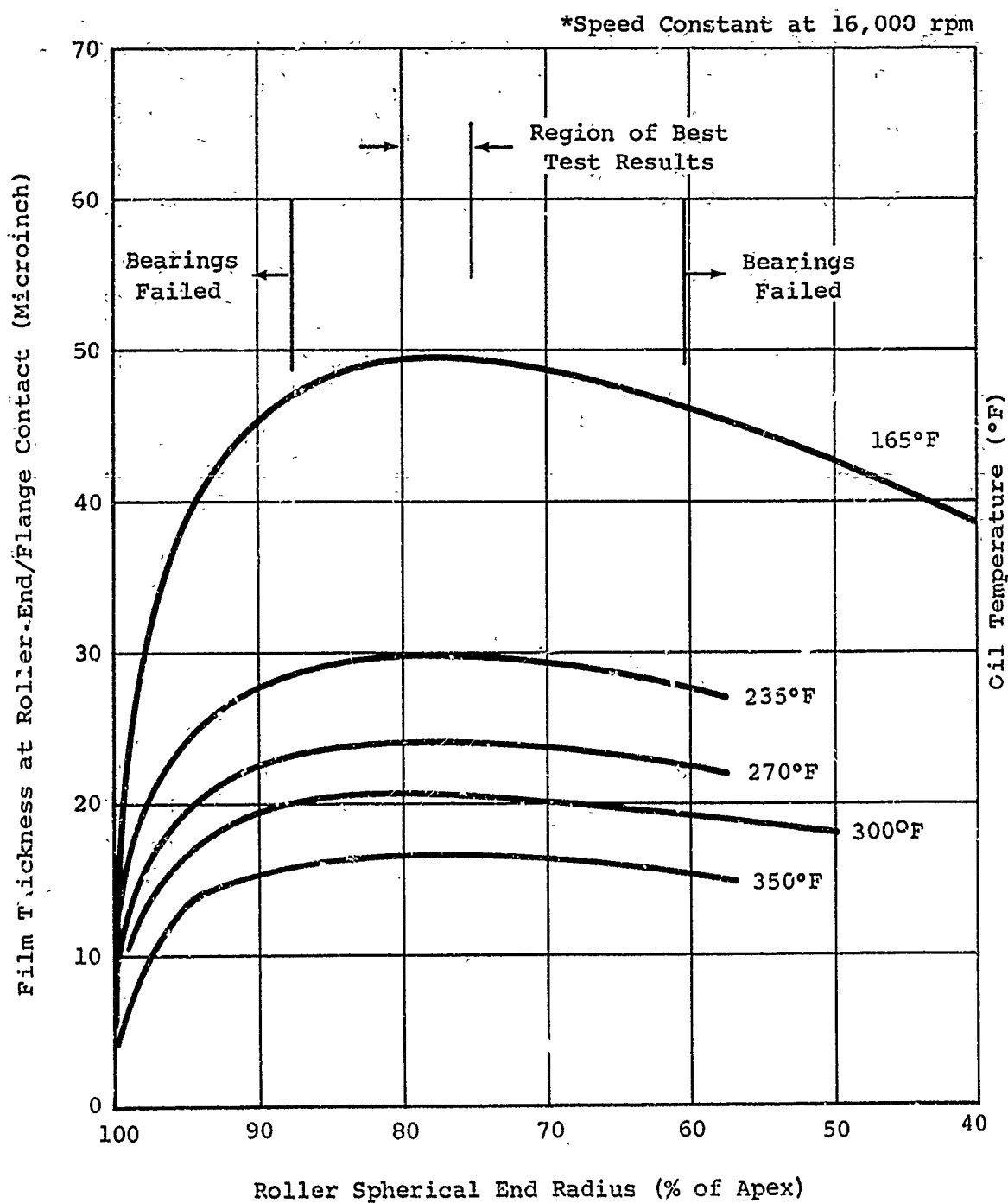scuffing was the result of not maintaining an adequate supply

89

Figure 54 . Film Thickness at Roller-End/Flange Contact
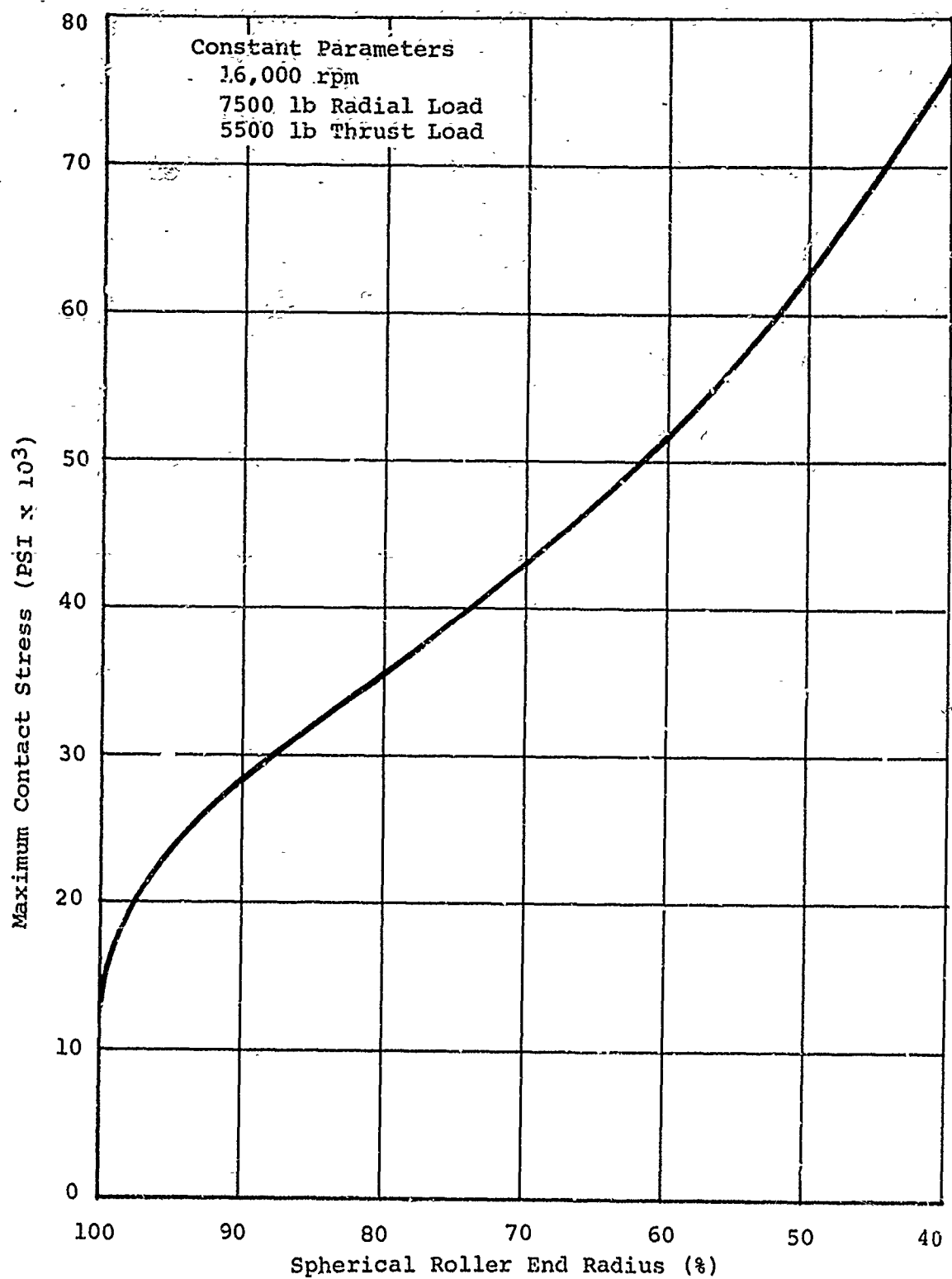Versus Roller Spherical End Radius and
Oil Temperature.

90

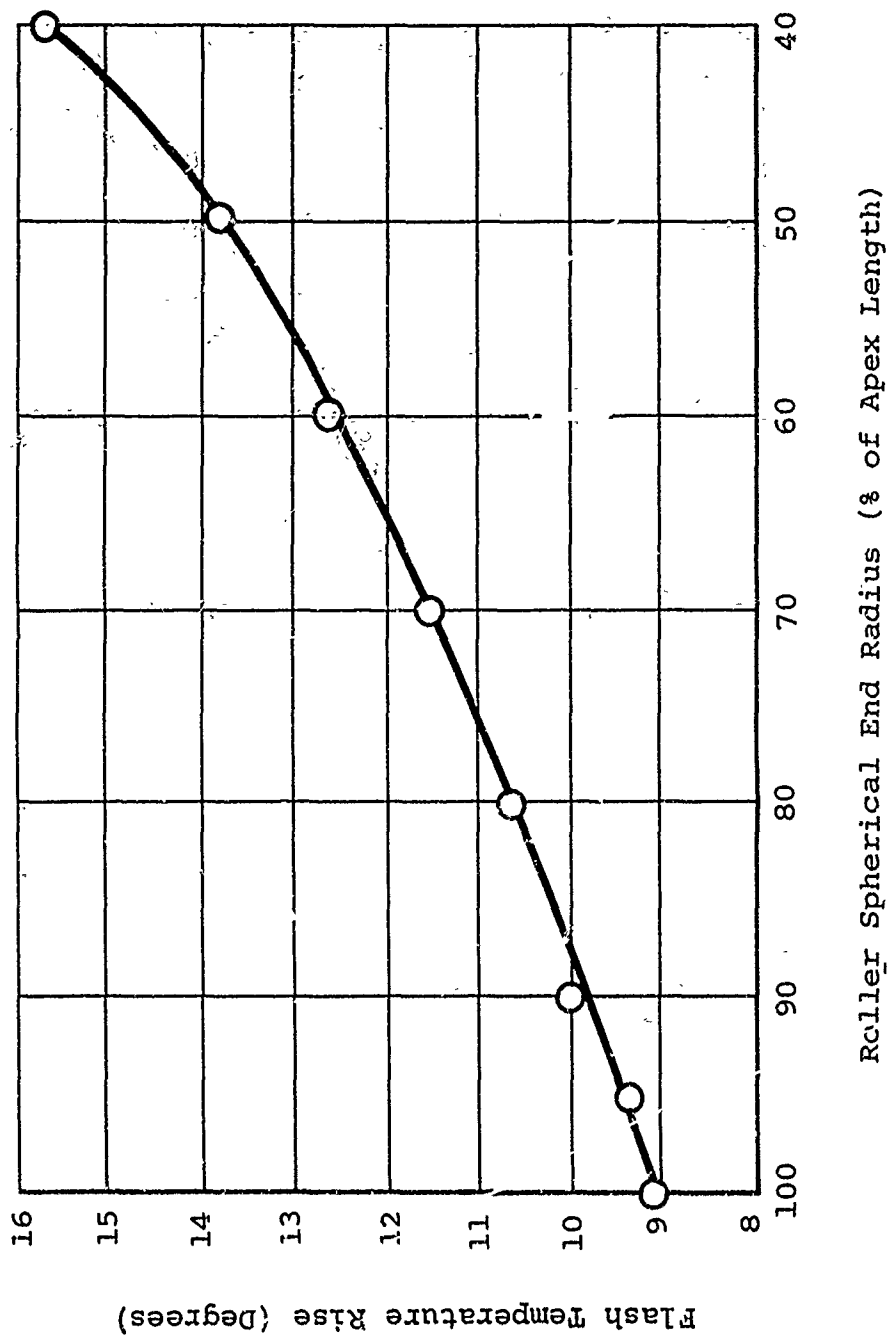Figure 55. Flange Contact Stress Versus
Roller Spherical End Radius.

Figure 56. Flash Temperature Rise Versus Roller Spherical-
End Radius.

92

of oil to the cone rib. Photographs shown in Figure 58
indicate that, beyond a velocity of 10,000 fpm (8000 rpm),
very little oil reaches this area by directing lubrication to
the small end of the bearing. As a result, a secondary source
of lubrication was developed which provided oil directly to
the cone rib area. Prior Boeing-Vertol tests were conducted
with three and six radial lube holes which showed an improve-
ment in the operating velocity attained (12,500 fpm). A
review of these prior failures showed a significant increase
in rib damage occurring away from each lubricant supply hole.
This data indicated that the spacing and oil distribution
obtained by the radial lube holes are very critical to the
performance of these bearings. An analysis was initiated to
determine the oil stream coverage on the cone-rib surface.

A ratio of flange coverage by the oil stream and hole spacing
appears to provide a good parameter for determining the
successful operation of high-speed, tapered roller bearings.
This parameter was plotted against the tangential velocity of
the cone rib contact point. The plot, Figure 57, shows that
a good correlation can determine the oil stream hole ratio
for satisfactory bearing operation. Further studies covering
other size bearings will be required to establish the appli-
cability of this method for all size bearings. High-speed,
strobe light photographs were taken of a cone spinning at
various speeds to show the oil stream leaving the radial lube
holes. These photographs, summarized in Figure 58, further
substantiate the accuracy of the analytical method which was
developed to predict the trajectory and coverage of the
lubricant on the cone rib.

The two series of photographs show the effect of varying speed
and the number of radial lubricant supply holes. Other
important features of these photographs are the balanced oil
flow at each radial hole location. This balanced oil distri-
bution is evidence that the type of oil manifold design used
for this bearing does, in fact, provide equal flow to each
radial hole. Figure 26 illustrates how the oil collects at
the upper end of the manifold before the oil feeds each radial
hole location. This method insures that only a few supply
holes in the shaft are required to provide an even distri-
bution of oil to the increased number of lube holes in the
bearing cone. This configuration also allows the oil to
have essentially zero velocity prior to entering the lube
hole. Also noted in these photographs is the minimum effect
of speed in providing changes in the oil stream path.

93
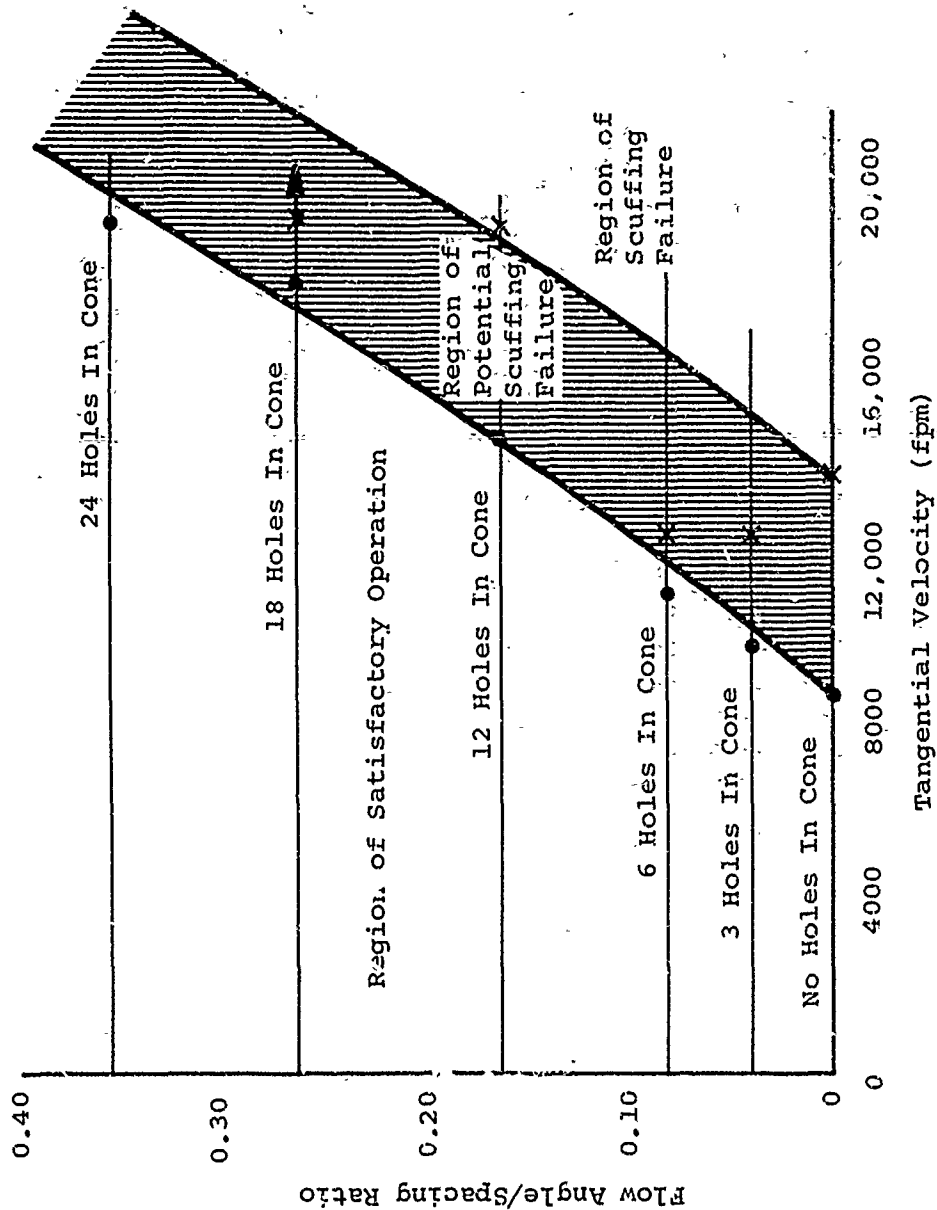
Figure 57. Effect of Increased Lubricant Coverage of the Large End Rib on Bearing Performance

• Maximum Speed Achieved Without Failure

x Maximum Speed Achieved Resulting in Failure

16,000 rpm

16,000 rpm

10,000 rpm

12 Holes in Cone, 6 Pints/Min Oil Flow Rate

10,000 rpm

24 Holes in Cone, 6 Pints/Min Oil Flow Rate

Oil
Stream   5000 rpm
Path
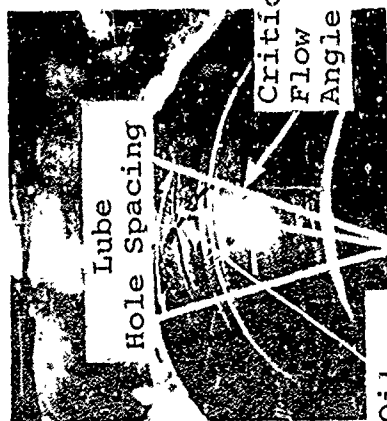
Lube
Hole Spacing

Critical
Flow
Angle (θ.)

5000 rpm

Figure 58.   6500 Series Bearing Oil Distribution Study.

Figure 59 plots shaft speed versus spacing ratio for the test
bearing used in this program. The plot shows a 6 percent
increase in spacing ratio occurring when the shaft speed is
increased from low rpm to 16,000 rpm. The above study
indicated that in order to increase the oil coverage on the
cone rib (flange), the number of holes had to be increased.
Therefore, other variables were investigated to determine
approaches for increasing the oil coverage and significantly
increasing the speed capability of the tapered roller bearing.

The following parametric study was conducted after all fabri-
cation of the test bearings was completed. Therefore, no
testing was conducted to verify the changes predicted by this
study. The summary of two parametric studies is shown in
Figure 60. These studies show that hole inclination angle
and lube hole length have a significant effect on the oil
distribution on the flange. Changes in these two variables
can greatly increase the flow angle/spacing ratio, but will
be limited by manufacturing and fabrication considerations.
Careful consideration must be given to both of these variables
in order to obtain the maximum benefit from increasing the
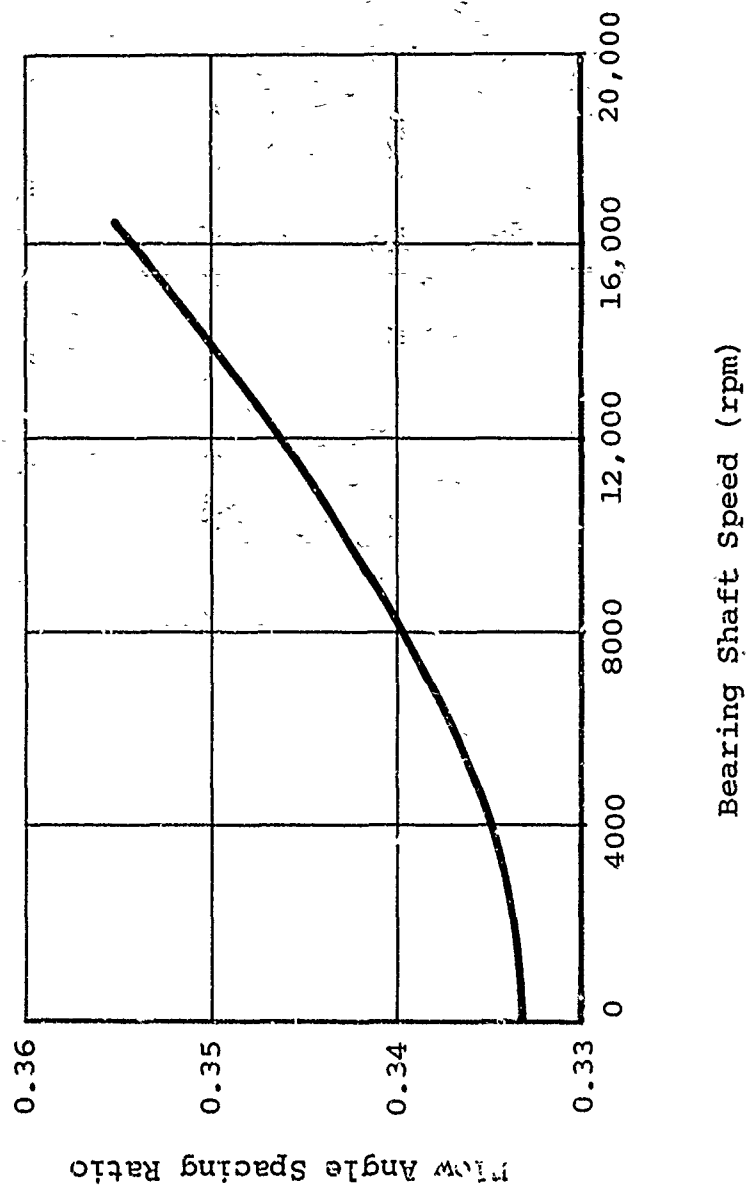oil ratio.

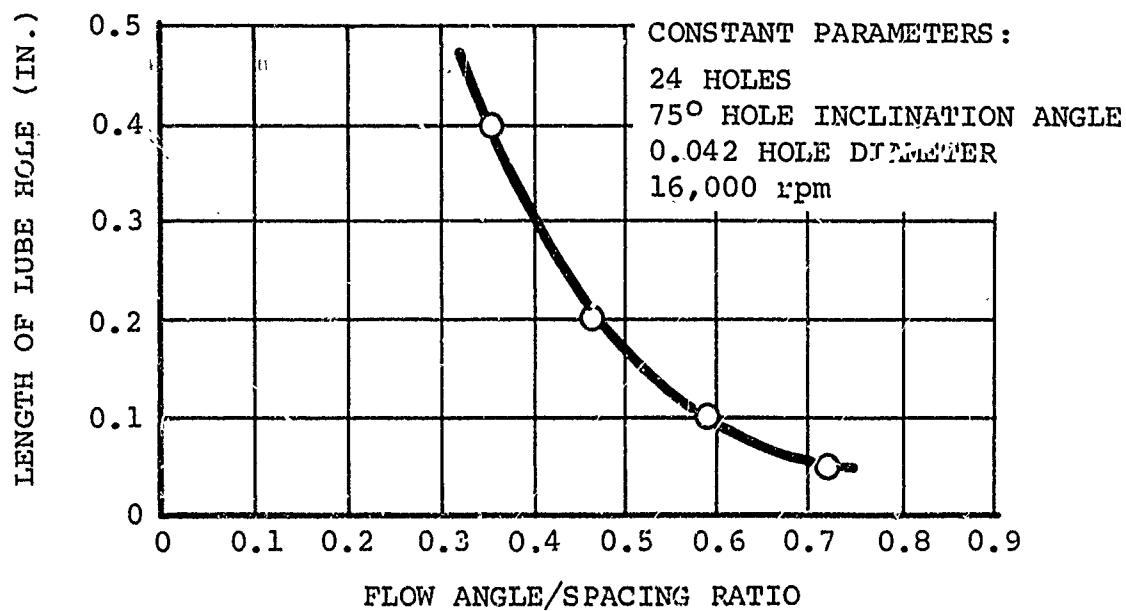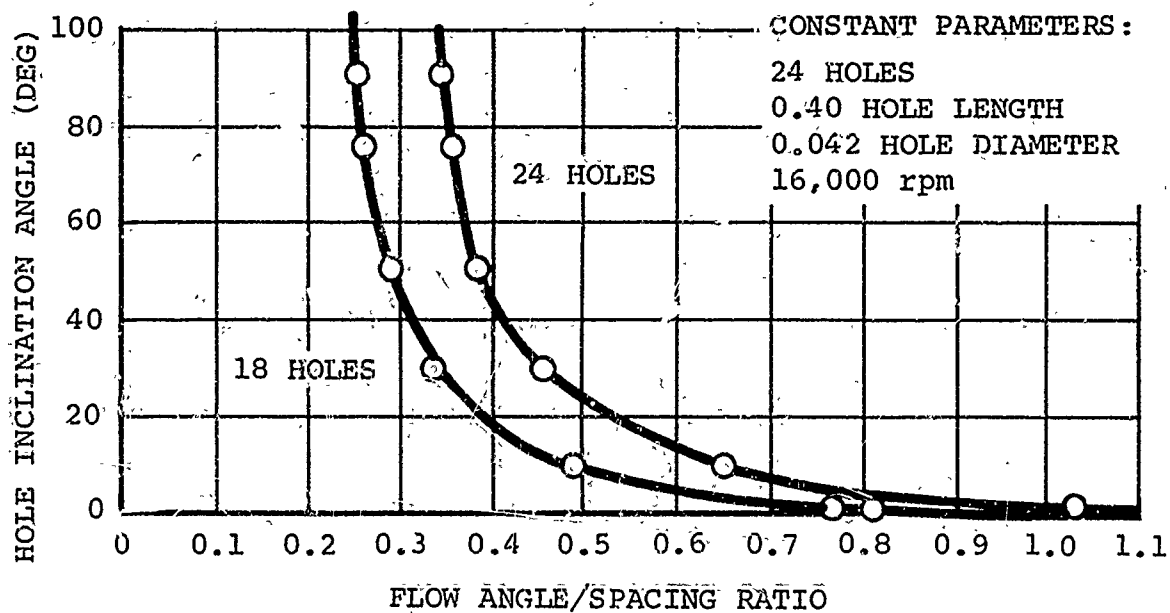Figure 59. Effect of Shaft Speed on Oil Flow Angle Spacing.

97

Figure 60. Flow Angle/Spacing Ratio Versus Lube Hole Length and Inclination Angle.

CONCLUSIONS

Based upon the results obtained from the experimental test program, the following conclusions were reached concerning the performance of the 6500-series high-speed, tapered roller bearings:

- ## Oil Flow Rates

  Oil flow rates of 2 pints/minute to the small end of the bearing and 4 pints/minute through the radial holes in the cone to the large end of the bearing are satisfactory for normal operation. The verification tests were all run with these oil flow rates. Oil flow rates as small as 2 pints/minute through the holes in the cone and no flow to the small end of the bearing appear feasible for fail-safe operation utilizing a small auxiliary lube system.

- ## Roller Spherical End Radii

  A roller spherical end radius equal to 75 percent to 80 percent of the apex length is optimum for the 6500-series bearing.

- ## Bearing Cage Plating and Coating

  There is no apparent difference in performance between the phosphate-coated and silver-plated flared cages as tested in this program; however, the silver-plated cage has an advantage over phosphate coating in a marginal lubrication situation. Cages that are silver plated should have a nickel strike and a silver strike before silver plating. While none of the bearings with brass-plated cages could be run at 16,000 fpm, there was no evidence that would indicate that brass plating was not a satisfactory plating material for high-speed operation. All tests with brass-plated cages were stopped because of roller-end/cone rib scuffing damage.

- ## Surface Finish

  There is no apparent difference in bearing performance with surface finishes on the cone rib face, cone race, roller body and roller spherical end radius in the range

99

of 4 to 13 microinches(AA). The range of finishes ob-
tained in this program is typical for standard production
lots. There was no apparent correlation between cone rib
scuffing and surface finish.

● Flared and Standard Cages

There is no apparent difference in performance between
cages that are flared to relieve roller body contact
(see Figure 13) and standard stamped-steel cages. Cages
that were phosphate coated, silver-plated and brass-
plated were tested in both the flared and standard stamped
steel configuration.

● Number of Holes through Cone

There was no measurable difference (temperature, torque,
etc.) between the bearings tested with eighteen and
24 radial holes from the bearing cone backface chamfer
(oil manifold) to the large end cone rib undercut. How-
ever, the occasional roller-end/cone rib damage experi-
enced with the bearings having 18 radial holes showed that
bearing cones with 24 holes were superior and were used in
the verification tests.

● Verification Tests

Results of the verification tests, eight bearings, showed
that the modified 6500-series bearing can be operated
at 16,000 rpm (20,000 fpm) for 24 hours with oil flow
rates of 2 pints/minute to the small end and 4 pints/
minute through the radial holes from the cone backface
(oil manifold) to the large end rib undercut. These
tests were run with 7500 pounds radial and 5500 pounds
thrust load. The bearings used had rollers with spherical
end radii equal to 80 percent of the apex length. Four
of these bearings had silver-plated, stamped-steel flared
cages and four had silver-plated, standard stamped-steel
cages.

● Reduced Radial and Thrust Load Tests

The two bearings tested under 80 percent of the 7500-
pound radial load and 5500-pound thrust load showed no
sign of bearing distress after running for 8 hours.

100

One of the two bearings tested was damaged when the load was reduced to 60 percent. This damage, due to the peculiarity of the test machine design, would not happen in a normal transmission application where the cups are fixed in a housing and the cones are fixed on the shaft.

- **Fail-Safe Bearing Tests**

Results of the fail-safe bearing test show that a DuPont Vespel SP-21 bearing rib insert is not satisfactory as a fail-safe material. The Vespel rib insert was pitted and broke loose from the bearing cone after running at 9000 rpm for 15 minutes, terminating the test. The cone with the DuPont T-400 alloy applied to the rib and the cone with Borkote applied to the rib, roller spherical ends and cages appeared satisfactory after this test.

The machined, race-guided centerline contact cages require radial lubrication holes from the cone backface chamfer (oil manifold) to the large rib outside diameter. This lubricates the area where the cage flange inside diameter contacts the rib outside diameter.

Bearing No. 83031-39 with the T-400 rib, standard rollers and a silver-plated, machined cage appeared in excellent condition after running 149 hours at 16,000 rpm in the center-radial-load-only position. The T-400 material appears to be a good material for future fail-safe evaluation.

TAPERED ROLLER BEARING APPLICATION

On the basis of the work performed under the contract, it is concluded that tapered roller bearings, utilized in a duplex-set arrangement for supporting spiral bevel gearing in helicopter transmissions, will provide improved performance over ball and cylindrical roller bearing systems. In addition, tapered roller bearing systems offer greater design flexibility than equivalent ball and roller bearing systems in helicopter transmissions.

RECOMMENDATIONS

Based upon the successful results obtained from this program, further work is recommended for the following areas:

1. Fatigue life testing is recommended for the 6500-series, high-speed tapered roller bearings. This additional testing is necessary to substantiate their use in supporting spiral bevel gears as required for advanced helicopter transmission applications.

2. Additional testing is recommended to determine the effect of increasing the ratio of oil coverage versus lube hole spacing (cone rib) on extending the operating range of tapered-roller, spiral-bevel support bearings. Testing in this program was limited to 20,000 fpm velocity and one size bearing. Testing additional size bearings at higher velocities and increased ratio values could substantiate the use of this parameter as a design tool.

3. Full-scale helicopter transmission tests are recommended to demonstrate the performance of high-speed, tapered-roller spiral bevel support bearings under typical operating conditions.

LITERATURE CITED

1. Harris, T. A., ROLLING BEARING ANALYSIS, New York, John Wiley and Sons, Inc., 1966.

2. Archard, J. F., and Cowking, E. W., ELASTOHYDRODYNAMIC LUBRICATION AT POINT CONTACTS, Procedures of the Institution of Mechanical Engineers, 1965-1966.

3. Dowson, D., and Higginson, G., ELASTOHYDRODYNAMIC LUBRICATION, London, England, Pergamon Press, 1966.

4. Rothbart, H. A., MECHANICAL DESIGN AND SYSTEMS HANDBOOK, New York, McGraw-Hill Book Company, 1964, pp. 13-3 to 13-9.

5. Blok, H., THE FLASH TEMPERATURE CONCEPT, Wear, Vol. 6, 1963, pp. 483-494.

6. Coleman, W., A SCORING FORMULA FOR BEVEL AND HYPOID GEAR TEETH, Transactions of American Society of Mechanical Engineers, April 1967.

7. Moyer, C., and Wren, F., UNDERSTANDING FRICTION AND EHL FILMS IN CONCENTRATED CONTACTS OF A TAPERED ROLLER BEARING, EHL Symposium, Leeds, England, 1972.

8. Marks, L., MECHANICAL ENGINEERS HANDBOOK, Fifth Edition, New York, McGraw-Hill Book Company, Inc., 1951, p. 181.

9. Lundberg, G., ELASTISCHE BERUHRUNG ZWEIER HALBRAUME HORSCHUNG, Vol. 10, N. 5, VDI Verlay, Berlin, 1939.

10. Lundberg, G., and Palmgren, A., DYNAMIC CAPACITY OF ROLLER BEARINGS, ACTA Polytechnica Mechanical Engineering Series, Vol. 2, N. 5, Stockholm, 1952.

DEVELOPMENT OF INTERNAL GEOMETRY OF TAPERED ROLLER
BEARINGS

The tapered roller bearing operates on the principle that the
rolling elements and raceways are constructed so that their
mating surfaces form cones which meet at a common point (i.e.,
the apex), on the axis of the bearing. This construction in-
sures true rolling motion at the mating surfaces (except at
the roller-end/flange contact) and also provides the capabil-
ity of reacting combined radial and thrust loads. The basic
construction and the identification of the various parts of a
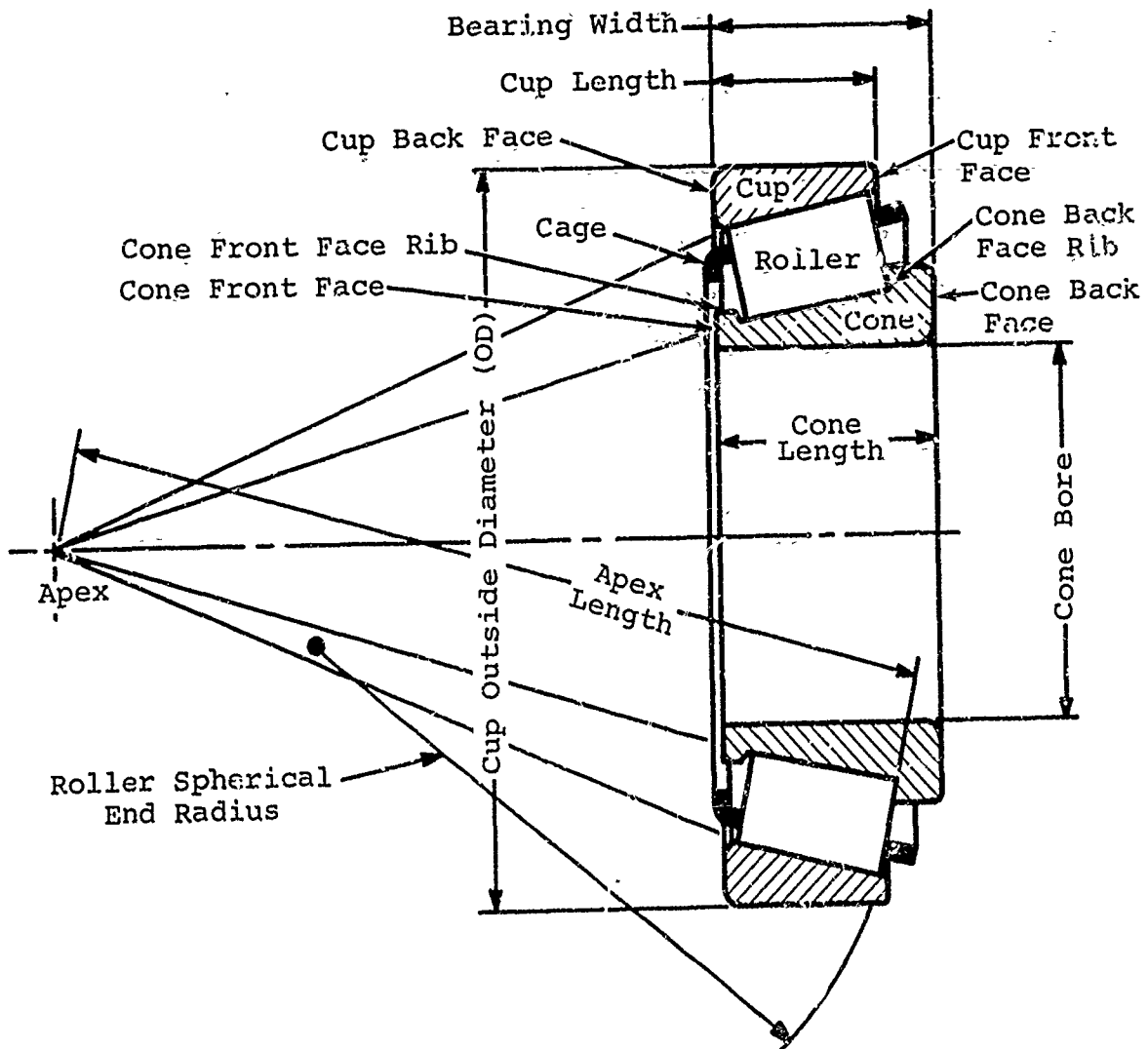tapered roller bearing are shown in Figure 61.

Figure 61. Tapered Roller Bearing Component Identification.

In order to understand the kinematics and internal loading of a tapered roller bearing, it will be necessary to define several basic geometry relationships. The following section defines the various angles and dimensional relationships which are essential in the development of other analyses such as contact stresses, oil film thickness, and kinematics.

Figure 62 defines the basic angles and dimensions necessary to develop a proper analysis of the operation of a high-speed tapered roller bearing. Based on these dimensions, the following relationships can be developed to define all parameters necessary to evaluate tapered roller bearings.

For reasons which will become obvious later, the following quantities will be defined:

$$\nu_R = (1 - m_R^2)/(\pi E_R) \tag{1}$$

$$\nu_E = (1 - m_E^2)/(\pi E_E) \tag{2}$$

$$\gamma_G = D \cos(\gamma)/E \tag{3}$$

The angle from the centerline of the roller to the radius through the flange/roller-end contact point (see Figure 62) can be shown to be

$$\theta = \gamma + \gamma_B - 90° \tag{4}$$

The coordinates of the contact point with respect to the roller center are

$$r = R_E \sin(\theta) \tag{5}$$

$$\theta' = \sin^{-1}\left[\frac{d + \ell \tan(\psi/2)}{2R_E}\right] \tag{6}$$

$$t = R_E \left(\cos(\theta) - \cos(\theta')\right) + \ell/2 \tag{7}$$

The perpendicular distance from the point of contact to the bearing axis is

$$R_p = E/2 + t \sin(\gamma) - r \cos(\gamma) \tag{8}$$

The perpendicular distance from the intersection point of the flange and cone and the contact point of the flange and the roller end is found as follows (see Figure 62):

$$E_{TT} = \gamma - \theta \tag{9}$$
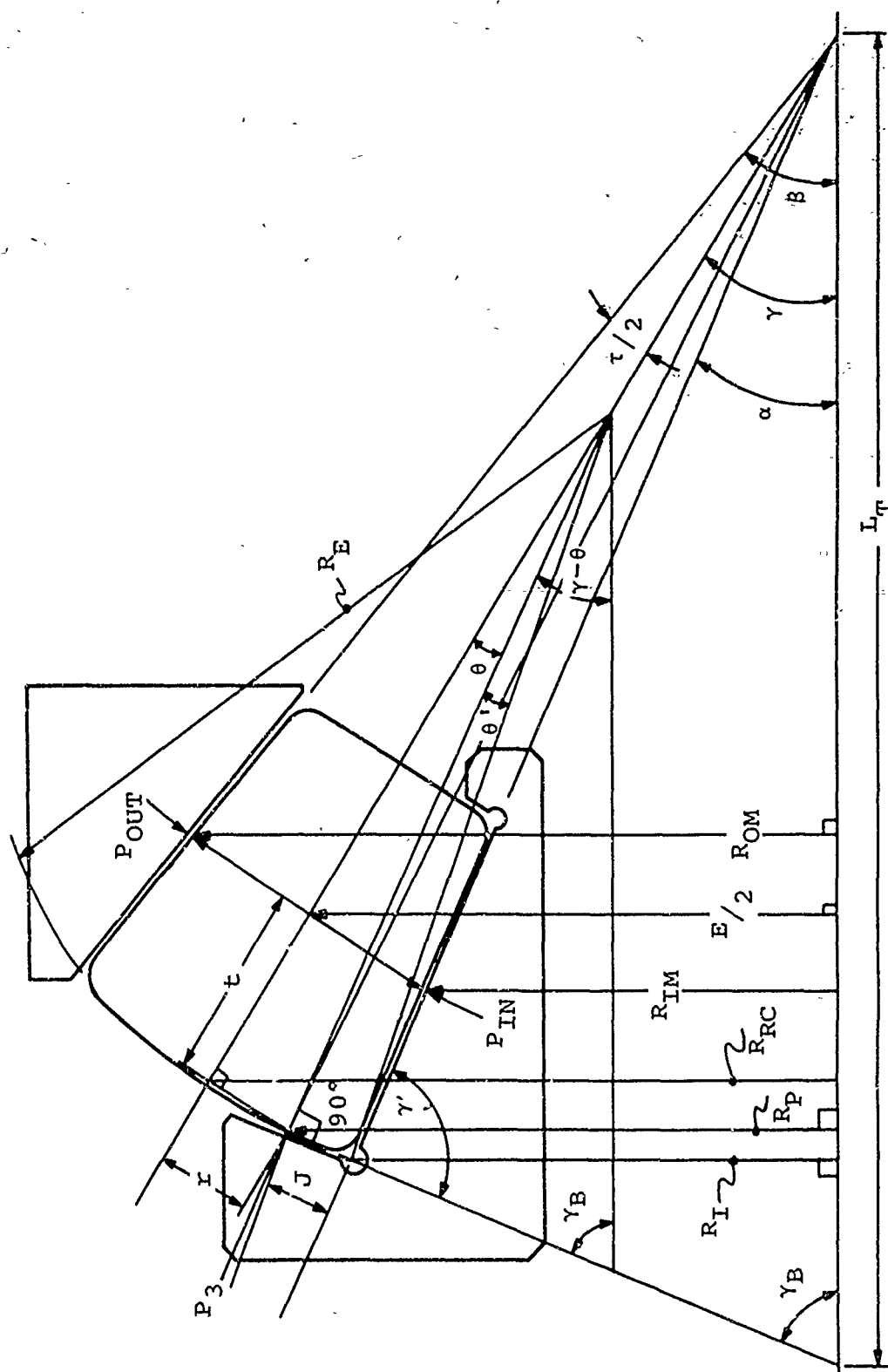
$$\gamma' = 180° - \gamma_B - \alpha \tag{10}$$

105

Figure 62. Basic Angles and Dimensions of Tapered Roller Bearing.

106

$$L_T = \frac{R_E}{\cos (B_{TT})} + \frac{R_P}{\tan (\gamma_B)} + \frac{R_P - R_E \sin (B_{TT})}{\tan (\gamma)} \qquad (11)$$

R_I may now be found from the law of sines

$$R_I = \frac{L_T \sin (\alpha) \sin (\gamma_B)}{\sin (\gamma')} \qquad (12)$$

Finally,

$$J = \frac{R_P - R_I}{\sin (\gamma_B)} \qquad (13)$$

At this point, some interesting geometric observations are worthy of note.

If B_{TT} is positive:

- The minor axis of the pressure ellipse will be in a plane containing the bearing axis.

- The flange curvature radius will be negative (i.e., the flange will be concave with respect to the roller end).

- The flange inclination angle will be less than 90°.

If B_{TT} is negative:

- The major axis of the pressure ellipse will be in a plane containing the bearing axis.

- The flange curvature radius will be positive (i.e., the flange will be convex with respect to the roller end).

- The flange inclination angle will be greater than 90°.

If B_{TT} is zero:

- The pressure ellipse will be a circle.

- The flange curvature radius will be infinite (i.e., the flange will be a flat plate perpendicular to the bearing axis).

- The flange inclination angle will be = 90°.

If θ is positive:

- The contact point will be on the cone side of the roller centerline.

- The Y dimension will be positive.

If θ is negative:

- The contact point will be on the cup side of the roller centerline.

- The Y dimension will be negative.

If θ is zero:

- The contact point will be on the roller centerline.

- The Y dimension will be zero.

The flange curvature radius in the direction of roller precession is

$$R_F = - R_p/\sin (B_{TT}) \tag{14}$$

ROLLING ELEMENT KINEMATIC ANALYSIS

The kinematic relationships of a tapered roller bearing are very important in understanding the critical velocities and motion necessary for determining oil film thickness, fatigue life, and speed effects. The analysis developed will assume sufficient load applied to the bearing to insure rolling motion. At this time dynamic effects such as sliding, gyroscopic pivotal motions, and EHD effects will be neglected. Review of the test conditions in this program shows that these assumptions are valid.

In general, both inner and outer races are considered to be rotating, with the inner race speed always positive and the outer race speed considered positive if it rotates in the same direction and negative if it rotates in the opposite direction.

The orbital speed (cage speed) of a nonslipping roller can be determined as follows (see Figure 63).

Note that

$$D_I = E - d \cos (\gamma) \tag{15}$$

$$D_O = E + d \cos (\gamma) \tag{16}$$

108

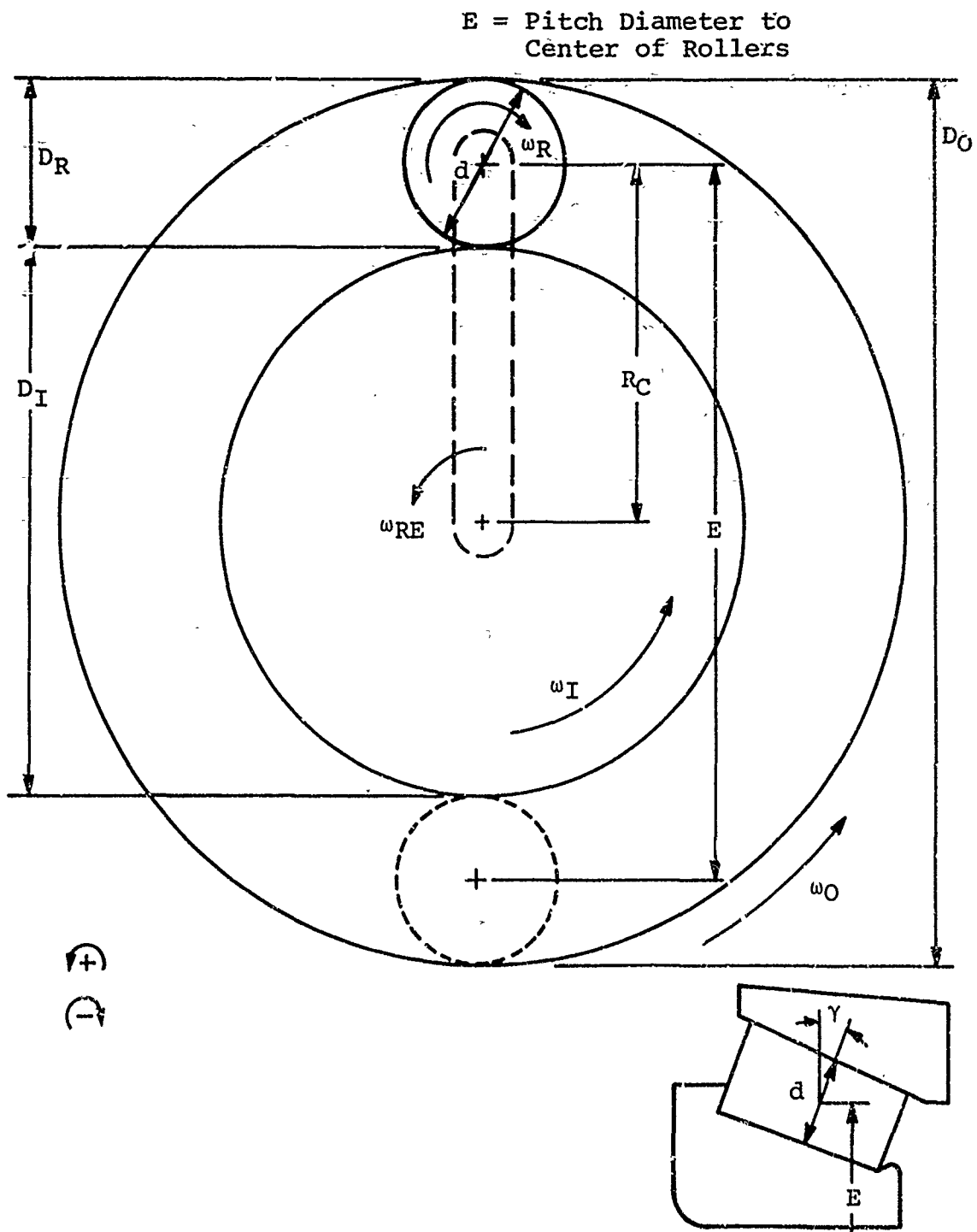E = Pitch Diameter to
Center of Rollers

Figure 63.   Two-Dimensional Schematic of Tapered Roller
             Bearing Kinematics.

For convenience in future calculations, we define

$$\gamma_G = \frac{d \cos (\gamma)}{E} \qquad (17)$$

The angular velocity of the outer race with respect to the roller center is

$$\omega_{O/RE} = \omega_O - \omega_{RE} \qquad (18)$$

Similarly, for the inner race

$$\omega_{I/RE} = \omega_I - \omega_{RE} \qquad (19)$$

The angular velocity of the roller about its own axis is

$$\omega_{R/RE} = \omega_{O/RE} \, D_O/d \qquad (20)$$

or

$$\omega_{R/RE} = - \omega_{I/RE} \, D_I/d \qquad (21)$$

If the above equations are solved for ω_{RE}, we have

$$\omega_{RE} = \omega_O \left[\frac{D_O}{D_I + D_O} \right] + \omega_I \left[\frac{D_I}{D_I + D_O} \right] \qquad (22)$$

Combining equations (17), (18), (19), and (24) yields

$$\omega_{RE} = 1/2 \left[\omega_O (1 + \gamma_G) + \omega_I (1 - \gamma_G) \right] \qquad (23)$$

Note that

$$D_O/D_R = \frac{E + d \cos \gamma}{d} \qquad (24)$$

and

$$\frac{E + d \cos \gamma}{d} = \frac{E}{d} (1 + \gamma_G) \qquad (25)$$

If we may combine equations (18), (20), and (23), we find that

$$\omega_{R/RE} = \frac{E}{2d} (1 - \gamma_G^2) (\omega_O - \omega_I) \qquad (26)$$

110

Utilizing vector notation, the absolute angular velocity of the roller is

$$\vec{\omega}_R = \vec{\omega}_{R/RE} + \vec{\omega}_{RE} \tag{27}$$

Since $\vec{\omega}_{R/RE}$ and $\vec{\omega}_{RE}$ are vectors, we must add them vectorially (see Figure 64).

$$\vec{\omega}_R = \left((\omega_{R/RE} \cos(\gamma) + \omega_{RE}) \, \vec{i} + (\omega_{R/RE} \sin(\gamma)) \, \vec{j} \right) \tag{28}$$

$$\omega_R = \left((\omega_{R/RE} \cos(\gamma) + \omega_{RE})^2 + \left(\omega_{R/RE} \sin(\gamma)\right)^2 \right)^{1/2} \tag{29}$$

$$\gamma_R = \tan^{-1} \left[\frac{\omega_{R/RE} \sin(\gamma)}{\omega_{R/RE} \cos(\gamma) + \omega_{RE}} \right] \tag{30}$$

The sliding velocity at the point of contact between the roller end and the rib flange can be found by subtracting the absolute linear velocities of the flange and the roller end at the contact point.

The linear velocity of the flange at the contact point is obviously dependent upon which race the flange is attached to as well as its angular velocity. Therefore, when it is attached to the inner race,

$$\vec{V}_F = \vec{\omega}_I \times \vec{R}_p \tag{31}$$

and when it is attached to the outer race,

$$\vec{V}_F = \vec{\omega}_O \times \vec{R}_p \tag{32}$$

The linear velocity of the roller at the contact point may be found as follows:

$$\vec{V}_{RP} = \vec{V}_{RP/RE} + \vec{V}_{RE} \tag{33}$$

That is, the velocity of the roller contact point is equal to the vectorial sum of its velocity with respect to the roller centerline ($\vec{V}_{RP/RE}$) and the velocity of the roller centerline ($\vec{V}_{RE}$).

$$\vec{V}_{RP/RE} = \vec{\omega}_R \times \vec{r} \tag{34}$$

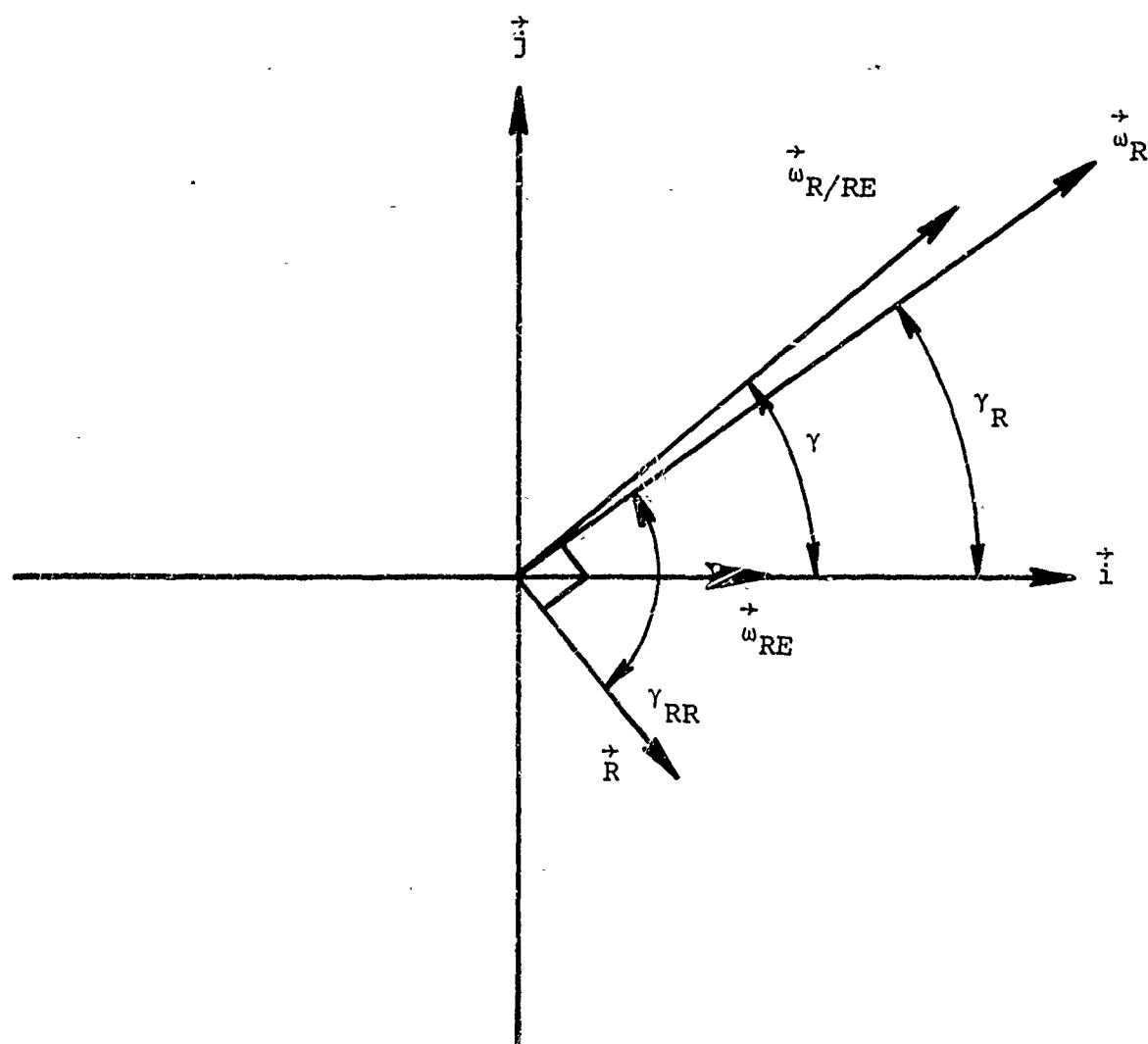$$\vec{V}_{RE} = \vec{\omega}_{RE} \times \vec{R}_{RC} \tag{35}$$

Figure 64.   Vector Representation of Roller Angular
            Velocities.

112

where (see Figure 62)

$$R_{RC} = E/2 + t \sin (\gamma)$$ (36)

And, from Figure 64,

$$\gamma_{RR} = 90 - \gamma + \gamma_R$$ (37)

Therefore,

$$V_{RP} = \omega_{RE} (E/2 + t \sin (\gamma))) + \omega_R r \sin (\gamma_{RR})$$ (38)

The sliding velocity at the flange/roller-end contact is

$$\vec{V}_S = \vec{V}_F - \vec{V}_{RP}$$ (39)

In order to determine the lubricant film thickness, we must first find the mean surface velocity at the roller-end contact point with respect to the velocity of the contact point. In the case of two cylinders on fixed centers, this velocity is simply the average of their surface velocities at the contact point, since the contact point is stationary. In a bearing, however, the roller system is undergoing epicyclic motion, so that the conjunction point itself has some motion. Therefore,

Flange
On Inner $$\vec{V}_{F/CP} = \vec{R}_P \times (\vec{\omega}_I - \vec{\omega}_{RE})$$ (40)
Race

Flange
On Outer $$\vec{V}_{F/} = \vec{R}_P \times (\vec{\omega}_O - \vec{\omega}_{RE})$$ (41)
Race

where $V_{F/CP}$ is the velocity of the contact point on the flange with respect to the flange/roller-end contact point.

Note that ω_I, ω_{RE}, and ω_O are all parallel to each other and perpendicular to R_P

$$\vec{V}_{RP/CP} = (\vec{\omega}_{R/RE} + \vec{\omega}_{RE} - \vec{\omega}_{RE}) \times \vec{r}$$ (42)

where $V_{RP/CP}$ is the velocity of the contact point on the roller-end with respect to the flange/roller-end contact point.

Equation (42) reduces to

$$\vec{V}_{RP/CP} = \vec{\omega}_{R/RE} \times \vec{r}$$ (43)

113

Note that $\vec{\omega}_{R/RE}$ and $\vec{R}$ are perpendicular.

Therefore, the mean surface velocity at the roller-end/flange contact point may be written as

Flange
On Inner $U_P = 1/2 \left[\vec{R}_P \ (\vec{\omega}_I - \vec{\omega}_{RE}) + \vec{r} \ (\vec{\omega}_{R/RE}) \right]$ (44)
Race

Flange
On Outer $U_P = 1/2 \left[\vec{R}_P \ (\vec{\omega}_O - \vec{\omega}_{RE}) + \vec{r} \ (\vec{\omega}_{R/RE}) \right]$ (45)
Race

It is interesting to note the following special cases for sliding velocity:

Flange
On Inner $V_S = \vec{r} \ \vec{\omega}_{R/RE} - (\vec{\omega}_I - \vec{\omega}_{RE}) \ \vec{R}_P$ (46)
Race

Flange
On Outer $V_S = \vec{r} \ \vec{\omega}_{R/RE} - (\vec{\omega}_O - \vec{\omega}_{RE}) \ \vec{R}_P$ (47)
Race

For the special case of a flange attached to a rotating inner race, equation (46) reduces to

$$V_S = \vec{r} \ \vec{\omega}_{R/RE} - (\vec{\omega}_I - 1/2 \ \vec{\omega}_I \ (1 - \gamma_G) \ (E/2$$

$$+ \ t \ \sin(\gamma) - r \ \cos(\gamma))$$ (48)

Thus, the R vector is negative when the contact is below roller centerline, so

$$V_S = - \ r \ \omega_{R/RE} - \frac{1}{2} \ \omega_I \ (1 + \gamma_G) \ (E/2 + t \ \sin(\gamma)$$

$$- \ r \ \cos(\gamma))$$ (49)

For convenience in analysis, we will define the following:

$\xi = + 1$ Flange on Inner Race

$\xi = - 1$ Flange on Outer Race

Using this method, the equation may be written as follows (note that the direction is negative when 0 is positive):

$$U_P = 1/2 \left[R_P \left((\omega_I \ (1 + \xi) + \omega_O \ (1 - \xi)) \ /2 - \omega_{RE} \right) \right.$$

$$\left. - \ r \ \omega_{R/RE} \right]$$ (50)

114

where U_P is the entraining velocity at the roller-end/flange contact point for any condition of flange attachment or race rotation.

Similarly,

$$V_S = -r\,\omega_{R/RE} - R_P\left(\left(\omega_i\,(1+\xi) + \omega_O\,(1-\xi)\right)/2 - \omega_{RE}\right) \quad (51)$$

where V_S is the sliding velocity at the roller-end/flange contact point for any condition of flange attachment or race rotation.

Therefore, Equations (50) and (51) are valid for any combination of race rotation and flange attachment.

Similar reasoning may be used to find the entraining velocities at the outer and inner race mean contact points.

We must first find the radii to the inner and outer race mean contact points, R_{IM} and R_{OM}, respectively.

Recalling Equation (17) and referring to Figure 62 we may write

$$R_{IM} = (E/2)\,(1 - \gamma_G) \quad (52)$$

$$R_{OM} = (E/2)\,(1 - \gamma_G) \quad (53)$$

Thus

$$U_I = 1/2\,\left(R_{IM}\,(\omega_I - \omega_{RE}) + R_{RI}\,\omega_{R/RE}\right) \quad (54)$$

where U_I = entraining velocity at inner race mean contact point

$$U_O = 1/2\,\left(R_{OM}\,(\omega_O - \omega_{RE}) + R_{RO}\,\omega_{R/RE}\right) \quad (55)$$

where U_O = entraining velocity at outer race mean contact point. Vector equations are not required since all radii and angular velocity vector combinations are mutually perpendicular.

The angular velocity of the rollers with respect to the flange is

$$\vec{\omega}_{R/F} = \vec{\omega}_R - \vec{\omega}_F \quad (56)$$

From equation (28) we have

$$\vec{\omega}_{R/F} = \vec{\omega}_{R/RE} + \vec{\omega}_{RE} - \vec{\omega}_F \quad (57)$$

115

We note that the vectors $\vec{\omega}_{RE}$ and $\vec{\omega}_F$ are parallel, while $\vec{\omega}_{R/RE}$ acts at an angle γ with the former. Therefore, the magnitude of $\vec{\omega}_{R/F}$ is

$$\vec{\omega}_{R/F} = \left((\omega_{R/RE} \sin(\gamma))^2 + (\omega_{R/RE} \cos(\gamma) + \omega_{RE} - \omega_F)^2 \right)^{1/2} \quad (58)$$

acting at an angle of γ_{RF} with the bearing centerline,

$$\gamma_{RF} = \tan^{-1}\left(\frac{\omega_{R/RE} \cos(\gamma) + \omega_{RE} - \omega_F}{\omega_{R/RE} \sin(\gamma)} \right) \quad (59)$$

Utilizing the parameter ξ, ω_F can be expressed as

$$\vec{\omega}_F = (\omega_I (1 + \xi) + \omega_O (1 - \xi))/2 \quad (60)$$

Similarly, the angular velocity of the roller centerline with respect to the flange is

$$\vec{\omega}_{RE/F} = \vec{\omega}_{RE} - \vec{\omega}_F \quad (61)$$

Note that $\vec{\omega}_{RE}$ and $\vec{\omega}_F$ are coplaner, so the vector signs may be dropped.

Since we know the kinematics of the three major contact points, we may now turn our attention to the detailed analysis of the loads on a single rolling element.

ROLLING ELEMENT LOAD ANALYSIS

For the roller shown in Figure 65, the curvature radius is related to the mean roller diameter and the roller taper half-angle by

$$R_{ROL} = \frac{d}{2 \cos(\tau/2)} \quad (62)$$

Figure 66 shows a schematic representation of the outer and inner race contacts at the mean diameter. R_{IM} and R_{OM} are defined in Equations (52) and (53), respectively. The race curvature radii are given by

$$R_{IMP} = R_{IM}/\sin(90 - \alpha) \quad (63)$$
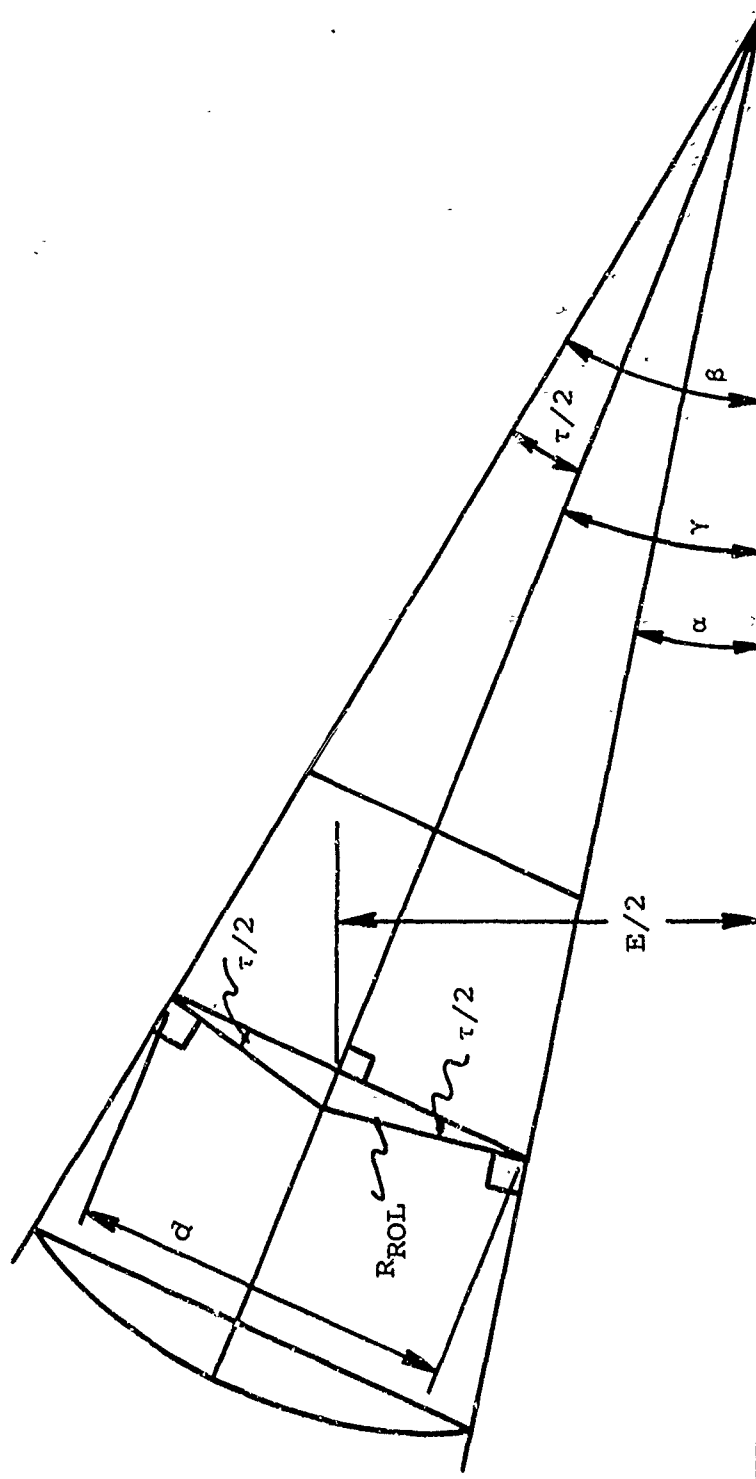
$$R_{OMP} = -R_{OM}/\sin(90 - \beta) \quad (64)$$

116

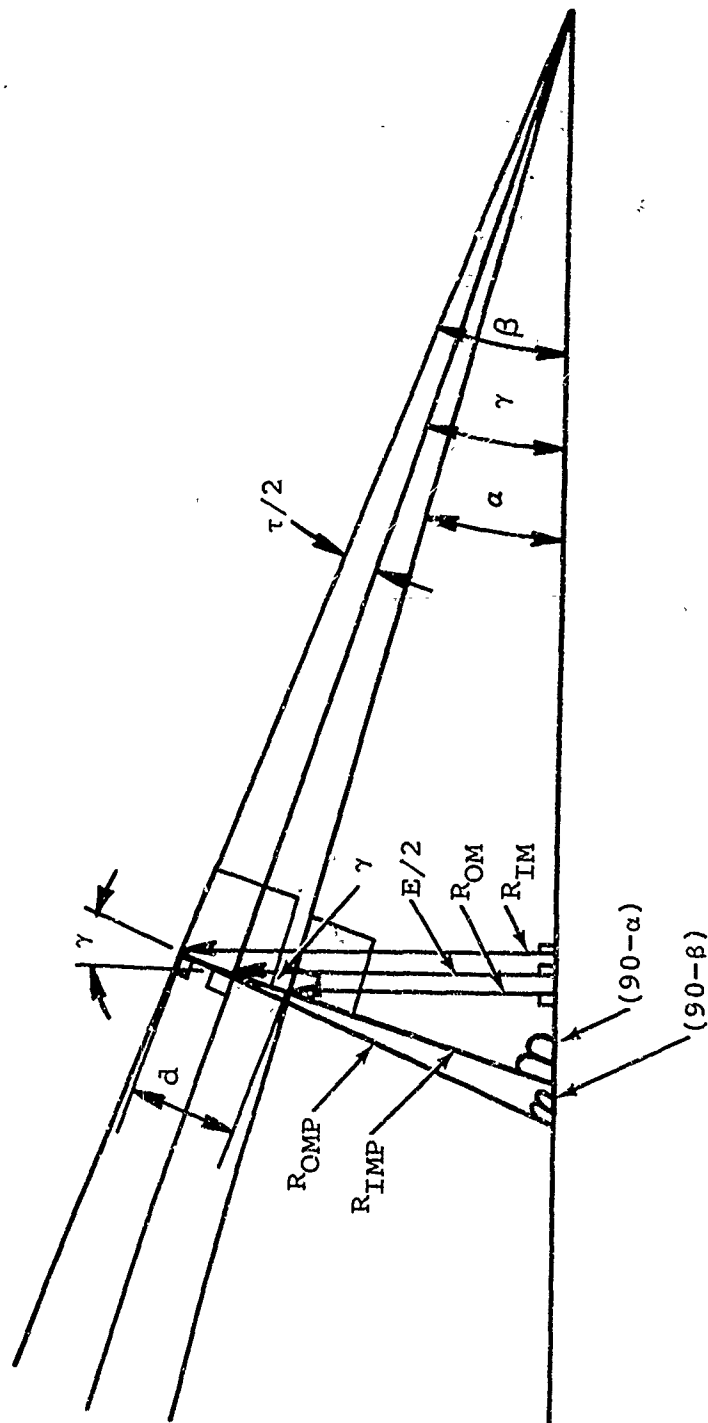Figure 65. Roll Mid-Diameter Curvature Radius Derivation.

Figure 66. Derivation of Race Curvature Radii.

But we know that sin $(90-X) = \cos (X)$, so Equations (63) and (64) may be rewritten as

$$R_{IMP} = R_{IM}/\cos (\alpha) \tag{65}$$

$$R_{OMP} = - R_{OM}/\cos (\beta) \tag{66}$$

Note that the negative sign is used in Equations (64) and (66) because the outer race is concave with respect to the roll.

The load at the inner race mean point is assumed to be known; thus the reaction forces at the outer race and the roller-end/flange may be calculated. An additional complication becomes apparent when one considers the two body forces, namely centrifugal force due to the rotation of the roller about the bearing axis and the gyroscopic moment due to $\omega R/RE$ and ωRE being noncolinear. Both of these vectors act through to the roller center of gravity. Prior to calculating these forces, the mass, mass moment of inertia, and the center of gravity of a roller must be defined. Since the spherical area at the end of the roller is quite small in comparison with the main body of the roller, we will neglect it in the calculation of the center of gravity.
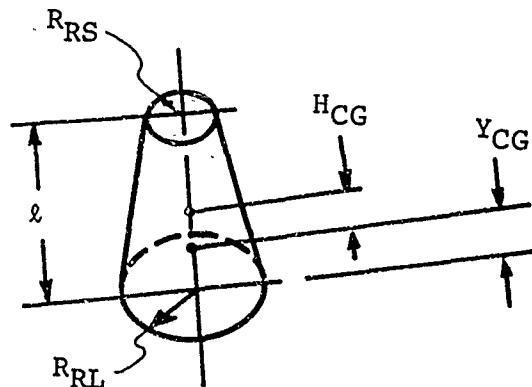

Figure 67. Truncated Circular Cone.

A tapered roller is simply a truncated circular cone (i.e., Figure 67). The distance from its large end to the center of gravity is given by

$$Y_{CG} = \frac{\ell\ (R_{RL}^2 + 2R_{RL}\ R_{RS} + 3R_{RS}^2)}{4\ (R_{RL}^2 + R_{RL}\ R_{RS} + R_{RS}^2)} \tag{67}$$

119

where R_{RS} and R_{RL} are as shown in Figure 68.
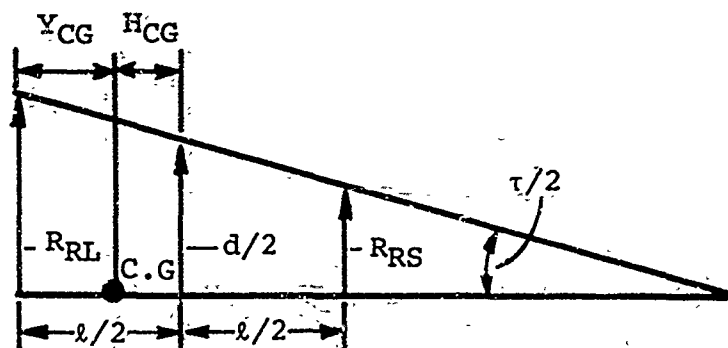
Figure 68.   Schematic for Deriving Roller Center of Gravity.

$$R_{RS} = \frac{(d - \ell \tan (\tau/2))}{2} \tag{68}$$

$$R_{RL} = \frac{(d + \ell \tan (\tau/2))}{2} \tag{69}$$

Thus, the distance from the mean section to the center of gravity is given by

$$H_{CG} = \frac{\ell}{2} \left(1 - \frac{(R_{RL}^2 + 2R_{RL} R_{RS} + 3R_{RS}^2)}{2 (R_{RL}^2 + R_{RL} R_{RS} + R_{RS}^2)} \right) \tag{70}$$

The radius (perpendicular to the bearing centerline) to the center of gravity of the roller from the bearing centerline is

$$R_{CG} = E/2 + H_{CG} \sin (\tau/2) \tag{71}$$

The volume of the roller may now be found (again referring to Figure 67) by

$$V_{ROL} = \left(\pi R_{RS}^2 + \pi R_{RL}^2 + \left(\pi R_{RS}^2 \; \pi R_{RL}^2 \right)^{1/2} \right) \frac{\ell}{3} \tag{72}$$

or

$$V_{ROL} = \frac{\pi \ell}{3} (R_{RS}^2 + R_{RL}^2 + R_{RS} R_{RL}) \tag{73}$$

The mass of the roller is then

$$M_{ROL} = \frac{\rho_{ROL} \, V_{ROL}}{g} \tag{74}$$

where ρ_{ROL} = the weight density of the roller
g = the acceleration due to gravity

The centrifugal acceleration of the roller is

$$\vec{a}_{CROLL} = R_{CG} \, \vec{\omega}_{RE}^2 \tag{75}$$

Finally, the centrifugal force on each roller is

$$\vec{CF} = M_{ROL} \, \vec{a}_{CROLL} \tag{76}$$

$\vec{CF}$ is a vector quantity whose direction is always perpendicular to the bearing centerline acting through the roller center of gravity.

All rolling-element bearings are, to some degree, gyroscopes (with extremely limited freedom). Thus, if the axis of roller rotation (about its own centerline) and the axis of roller precession (rotation of cage about bearing centerline) are not coincident, a restorative torque, the gyroscopic moment (1) will occur. This occurs in angular-contact ball bearings and tapered roller bearings but not in perfect cylindrical roller bearings. The effect of this gyroscopic moment must be added to the centrifugal force and the applied load to obtain accurate values for the flange end load and the outer race load.

The gyroscopic moment is given by

$$\vec{GM} = I_{ROL} \, (\vec{\omega}_{R/RE} \times \vec{\omega}_{RE}) \tag{77}$$

where $\vec{\omega}_{R/RE}$ = the roller's angular velocity about its own axis

$\vec{\omega}_{RE}$ = the roller's angular velocity about the bearing centerline

I_{ROL} = the mass moment of inertia of the roller

Since Equation (77) involves a cross product, it is obvious that, if $\vec{\omega}_{RE}$ and $\vec{\omega}_R$ are parallel, then GM will be zero. For the case of a tapered roller bearing, Equation (77) may be reduced (see Figure 64) to

$$GM = I_{ROL} \, \omega_{R/RE} \, \omega_{RE} \sin(\gamma) \tag{78}$$

121

At this point, some comments as to the direction of the gryo-scopic moment seem appropriate.

If the inner race is rotating while the outer race is station-ary, the direction of the gryoscopic moment may be determined from Figure 69 (viewing direction of rotation from the bear-ings large end).

Inner Race - CCW
Outer Race - Stationary

Inner Race - CW
Outer Race - Stationary
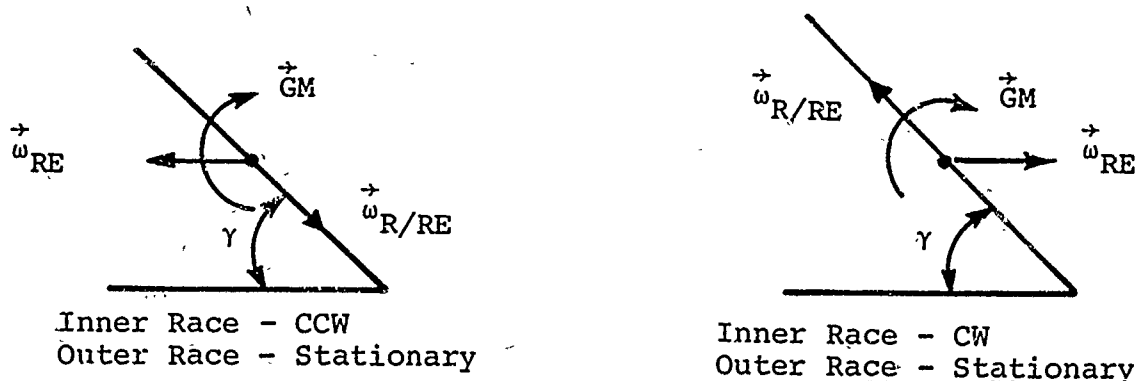
Figure 69. Direction of Gyroscopic Moment as a Function of Race Rotation Combinations.

Similarly if the inner race is stationary while the outer race rotates (same direction conventions), the direction of the gyroscopic moment may be determined from Figure 70.

Inner Race - Stationary
Outer Race - CCW

Inner Race - Stationary
Outer Race - CW

Figure 70. Direction of Gyroscopic Moment as a Function of Race Rotation Combinations.

Two additional possible cases are shown in Figure 71; that is, both races rotating in the same direction.

Both Races - CCW   Both Races - CW

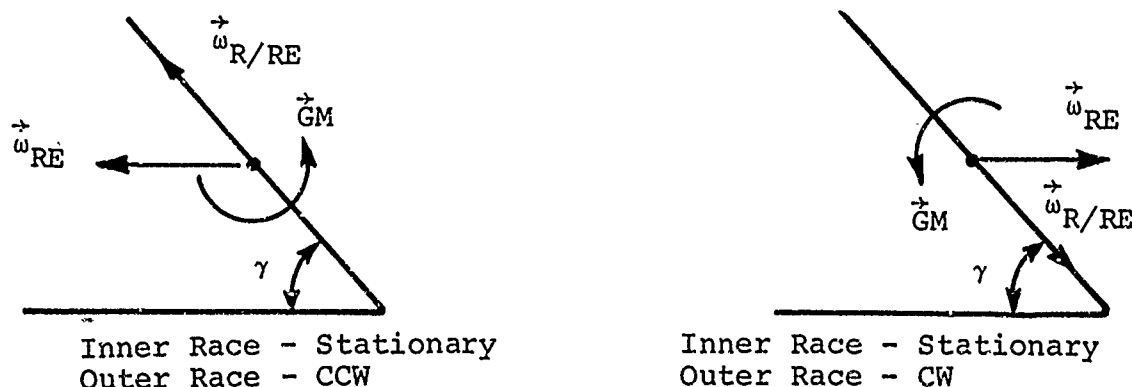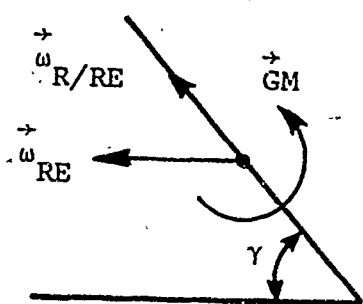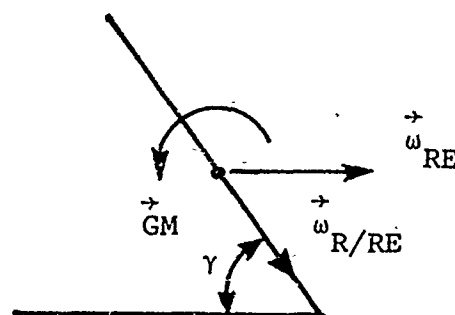Figure 71. Direction of Gyroscopic Moment as a Function of
            Race Rotation Combinations.

All other cases or race rotation combinations fit one of the
above situations. Thus, the scaler signs of the angular
velocities are sufficient to determine the direction of GM.

In some cases, GM tends to increase the flange load (e.g.,
Figures 70 and 71) and in some cases it tends to relieve the
flange load (e.g., Figure 69).

We may consider the roller as part of a full cone and simply
subtract the moment of inertia of the truncated part (see
Figure 66); that is,

$$I_{ROL} = \frac{3M_{ROL}}{10} (R_{RL}^2 - R_{RS}^2) \tag{79}$$

We will now consider the roller shown in Figure 72. P_I is ap-
plied load at the inner race midpoint, M_I is a moment at inner
race midpoint to account for any misalignment which may be
present, P_3 is the flange reaction load, P_O is the outer race
load, M_O is the outer race moment, and CF and MG are the cen-
trifugal force and gyroscopic moments.

The roller must be in equilibrium in the plane of the paper
so that

$$\sum F_Y = 0 = - P_O \cos (\beta) + P_I \cos (\alpha) - P_3 \sin (\gamma - \theta) + CF \tag{80}$$

$$\sum F_X = 0 = - P_O \sin (\beta) + P_I \sin (\alpha) + P_3 \cos (\gamma - \theta) \tag{81}$$

$$\sum M_O = 0 = (CF) \, H_{CG} \cos (\gamma) - GM - M_O + M_I$$

$$- (P_O - P_I) \frac{d}{2} \sin (\tau/2)$$

$$- P_3 (r \cos (\theta) - t \sin \theta) \tag{82}$$
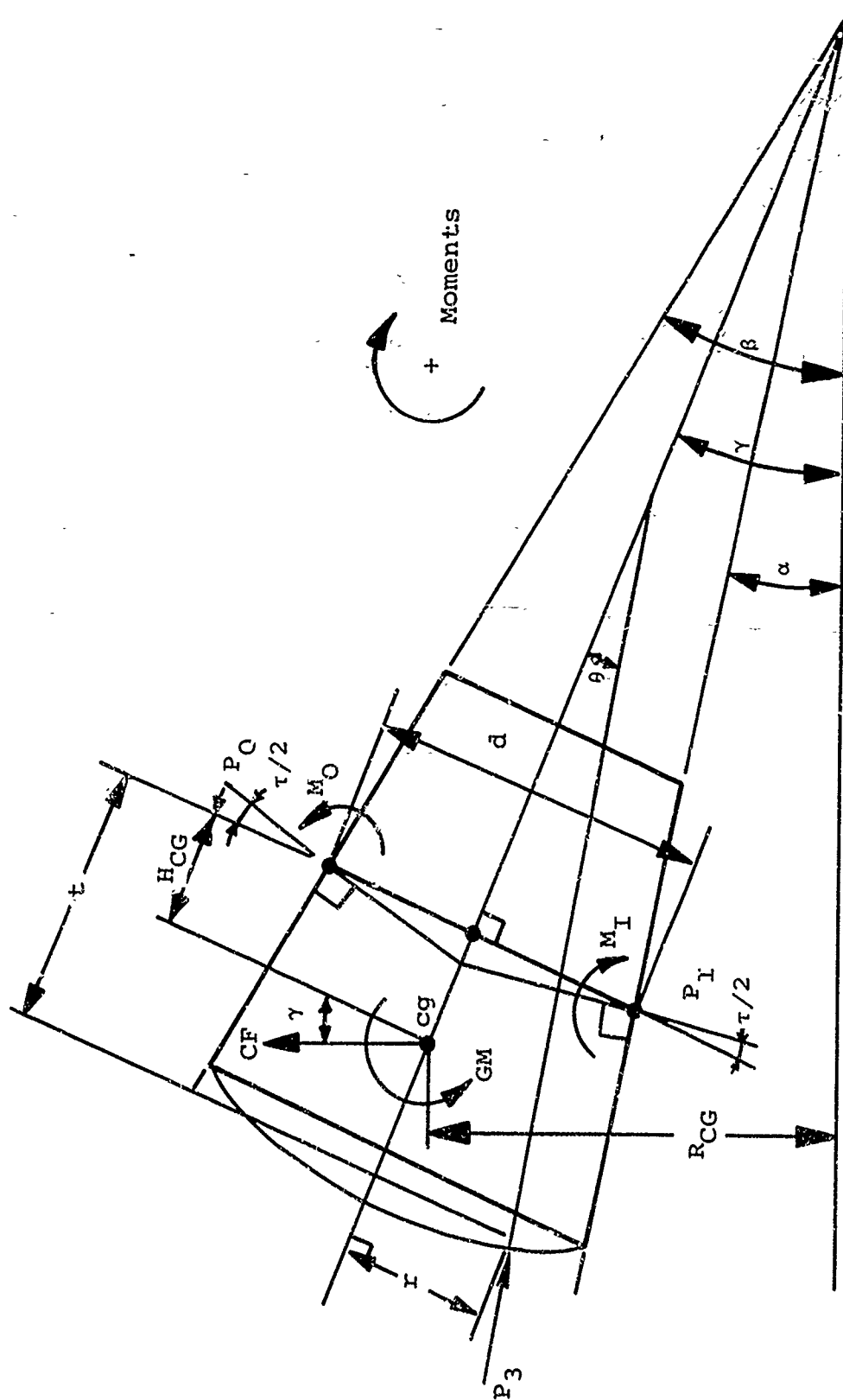
123

Figure 72. Schematic of Roiler Loads.

Equations (80) and (81) can now be rewritten as

$$P_3 = P_I \frac{\cos(\alpha)}{\sin(\gamma - \theta)} + \frac{CF}{\sin(\gamma - \theta)} - P_O \frac{\cos(\beta)}{\sin(\gamma - \theta)} \qquad (83)$$

$$P_3 = P_O \frac{\sin(\beta)}{\cos(\gamma - \theta)} - P_I \frac{\sin(\alpha)}{\cos(\gamma - \theta)} \qquad (84)$$

Eliminating P_3 and solving for P_O, we have

$$P_O = \frac{P_I \left(\dfrac{\cos(\alpha)}{\sin(\gamma - \theta)} + \dfrac{\sin(\alpha)}{\cos(\gamma - \theta)} \right) + \dfrac{CF}{\sin(\gamma - \theta)}}{\dfrac{\sin(\beta)}{\cos(\gamma - \theta)} + \dfrac{\cos(\beta)}{\sin(\gamma - \theta)}} \qquad (85)$$

Utilizing Equation (85) we can solve for P_O and by substituting this value into Equation (83) or (84) we can then find P_3. The only remaining unknown is M_O. It should be noted that, if both M_I and GM are zero, M_O will also be zero.

Rearranging Equation (91) yields

$$M_O = M_I - GM + (CF) H_{CG} \cos(\gamma) - (P_O - P_I) \frac{d}{2} \sin(\tau/2)$$

$$- P_3 (r \cos\theta - t \sin\theta) \qquad (86)$$

M_O may be found by substituting the appropriate parameters into Equation (86).

We now consider a tapered roller bearing rotating under no applied load. The centrifugal force of the rollers will give rise to a hoop stress in the outer race as it restrains them from further motion radially. However, due to the tapered nature of the bearing, a thrust load must be applied to the bearing to keep the cup and cone from separating axially due to the roller centrifugal force.

This thrust load may be considered as the declutching thrust, and if the applied thrust load is not equal to or greater than this value, the cup and cone will separate axially, and the bearing will be rapidly destroyed.

To find the value of this declutching thrust, we must simply solve Equations (83) and (84) simultaneously for P_3 with P_I set equal to zero. The resulting value obtained for P_3 is then multiplied by the cosine of the angle θ (to yield its axial component) and the number of rollers (to yield the total thrust force). Thus Equation (85) becomes

125

$$P_0' = \frac{CF}{\sin(\gamma - \theta)\left(\dfrac{\sin(\beta)}{\cos(\gamma - \theta)} + \dfrac{\cos(\beta)}{\sin(\gamma - \theta)}\right)} \qquad (87)$$

Substituting into (84) with $P_I = 0$ and simplifying yields

$$P_3' = \frac{CF \sin(\beta)}{\sin(\beta)\sin(\gamma - \theta) + \cos(\beta)\cos(\gamma - \theta)} \qquad (88)$$

Finally, the declutching thrust is

$$T_{DC} = Z \, P_3' \cos(\gamma - \theta) \qquad (89)$$
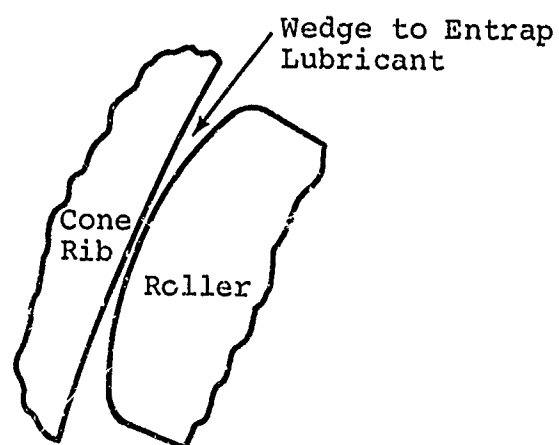
where Z is the number of rollers.

LUBRICANT FILM THICKNESS ANALYSIS

Previous sections have established mathematical relationships for roller loads, kinematics, and geometry for a tapered roller bearing. Knowing these relationships, the oil film thickness can be derived for the inner and outer race-roller contact and the roller-end/flange contact.

The roller-end/flange contact (see Figure 73) is the most critical contact in high speed tapered roller bearings. This contact between the roller end and cone flange is one of mixed rolling and sliding, and its geometry must be designed to generate an adequate oil film. To accomplish this, the large roller end is made spherical and the cone flange is made in the shape of a cone whose apex is on the cone center-line of the bearing. The roller-end spherical radius is generally smaller than the roller apex length. The contact area of the roller and flange is a point under no load, and becomes an ellipse under load.

The above design also provides a wedge-shaped opening in all directions from the contact point to entrap lubricant and enable the generation of an oil film. Archard and Cowking[2] have proposed the following equation to calculate the oil film thickness at a concentrated point load contact:

$$h = 2.04 \left(1 + \frac{2R_y}{3R_X}\right)^{-.74} (\mu_0 \, U \, \alpha')^{.74} (R)^{.41} \left(\frac{E_P}{W}\right)^{.074} \qquad (90)$$

Contact Changes to an
Ellipse Under Load

Roller Spherical
End Radius
(Apex Length)

Roller

Cone
Rib

A

A

No Load Contact
Point

Cone

Wedge to Entrap
Lubricant
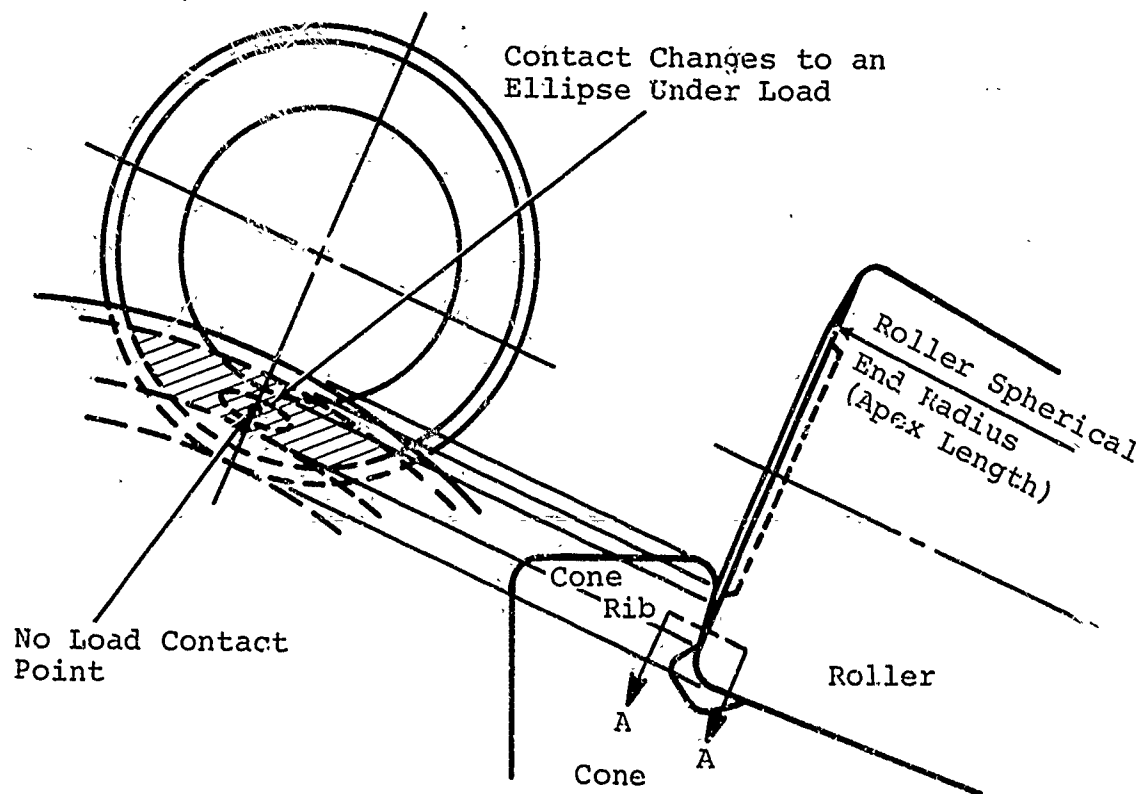
Cone
Rib

Roller

Section A-A

Figure 73.   Roller-End/Cone Rib (Flange) Contact.

where h = oil film thickness in inches

R_X, R_Y = effective curvature radii in the X and Y directions, respectively

μ_0 = absolute viscosity in reyns (lb-sec/in.^{2})

α' = pressure viscosity exponent in in.^{2}/lb

R = effective curvature radius in the direction of motion $\frac{1}{R} = \frac{1}{R_1} + \frac{1}{R_2}$

E_P = reduced modulus of elasticity, psi

W = load in pounds

U = entraining velocity, in./sec

The reduced modulus is defined as

$$E_P = \frac{1}{2}\left(\frac{1 - m_E^2}{E_E} + \frac{1 - m_R^2}{E_R}\right) \tag{91}$$

where E_E, E_R = the modulii of elasticity for the roller and race respectively

m_E, m_R = Poisson's ratio for the roller and race respectively

The theory of point contacts has been derived from the theory of line contacts modified by side leakage effects. The amount of leakage is determined by the ellipticity of the contact, which is expressed by the $\left(1 + \frac{2R_Y}{3R_X}\right)^{-.74}$ factor in equation (90).

In terms of the parameters already identified for the flange/roller-end contact, we have

$$R_Y = \frac{1}{\frac{1}{R_F} + \frac{1}{R_E}} \tag{92}$$

$$R_X = RE \tag{93}$$

$$W = P_3 \tag{94}$$

$$U = U_P \tag{95}$$

128

μ_0 and α' are dependent on the lubricant used and the conditions of pressure and temperature around the contact.

In a similar manner, the film thickness at the inner and outer race contacts may be approximated by the use of an equation proposed by Dowson[3]. The equation is valid for theoretical line contact between two cylinders whose curvature radii, at the contact line, are constant over their length, with a uniform load applied along their entire contact length. For the present, we will represent the tapered roller by a straight roller and race combination whose curvature radii are those of the tapered roller at the mean section.

Dowson's equation is

$$h = 2.65 \ (\alpha')^{.54} (\mu_0 \ U)^{.70} (E_P)^{-.03} (R)^{.43} (W')^{-.13} \tag{96}$$

where h, α', μ_0, E_P, and R are as defined previously

$$W' = \text{load per inch of contact length}$$

For the above equation to be useful, each parameter must be expressed in terms of known quantities. α', U, and E_P have the same values as they did when applied to Archard and Cowking's equation for both inner and outer race contacts.

The effective curvature radius R, the load W', and the entraining velocity U may be calculated as follows:

Outer Race Contact

$$R_O = \frac{1}{\dfrac{1}{R_{ROL}} + \dfrac{1}{R_{OMP}}} \tag{97}$$

$$W_O' = P_O/L_E \tag{98}$$

(neglecting the moment load)

where L_E = effective roller length

$$L_E = \ell - 2 \ (C_{RAD})$$

$$C_{RAD} = \text{roller corner radius}$$

$$\ell = \text{total roller length}$$

See Equation (55) for U_O.

129

Inner Race Contact

$$R_I = \frac{1}{\dfrac{1}{R_{ROL}} + \dfrac{1}{R_{IMP}}}$$

(99)

$$W_I{}' = P_I/L_E$$

(100)

See Equation (54) for U_I.

The above equations have been substantiated by work done by T. Wren and C. Moyer.[7] This analysis will be used later in this report to analyze and optimize the geometry of the roller-end/flange contact area for maximum film generation. The film thickness at the inner and outer race contact is dictated by the basic size and operating speed of the bearing.

CONE RIB (FLANGE) CONTACT STRESS

In addition to being a very critical area for film generation, the roller-end/flange contact must also be analyzed for contact stress. Under no load, the contact of the roller end and the cone rib flange is a point. However, this contact point spreads out into the form of an ellipse as load is applied to the bearing (see Figure 73). The performance of this contact can be drastically modified by changing the roller spherical end radius. Increasing this radius should provide a better path for the lubricant to reach the contact area, but at the same time increase the contact stress. As the spherical radius approaches the apex length of the tapered roller bearing, the contact ellipse may become larger than the available flange contact area, resulting in a truncated ellipse which will have an effect of scrapping away oil from the contact area. Therefore, the shape and the stress of the contact must be evaluated along with the oil film thickness in order to properly evaluate the roller-end/flange contact area.

The roller-end/flange contact can be represented by two general solid bodies in contact (4), as shown in Figure 74. If these two bodies are brought into contact at points O_1 and O_2 with X axes at an angle of ι. as shown in Figure 75, the orientation of the pressure area (which will be an ellipse as shown in Figure 76) is given by

$$\tan (2\omega_1) = \frac{-\left(\dfrac{1}{R_{X2}} - \dfrac{1}{R_{Y2}} \sin (2\omega)\right)}{\left(\dfrac{1}{R_{X1}} - \dfrac{1}{R_{Y1}}\right) + \left(\dfrac{1}{R_{X2}} - \dfrac{1}{R_{Y2}}\right) \cos (2\omega)}$$

(101)

130

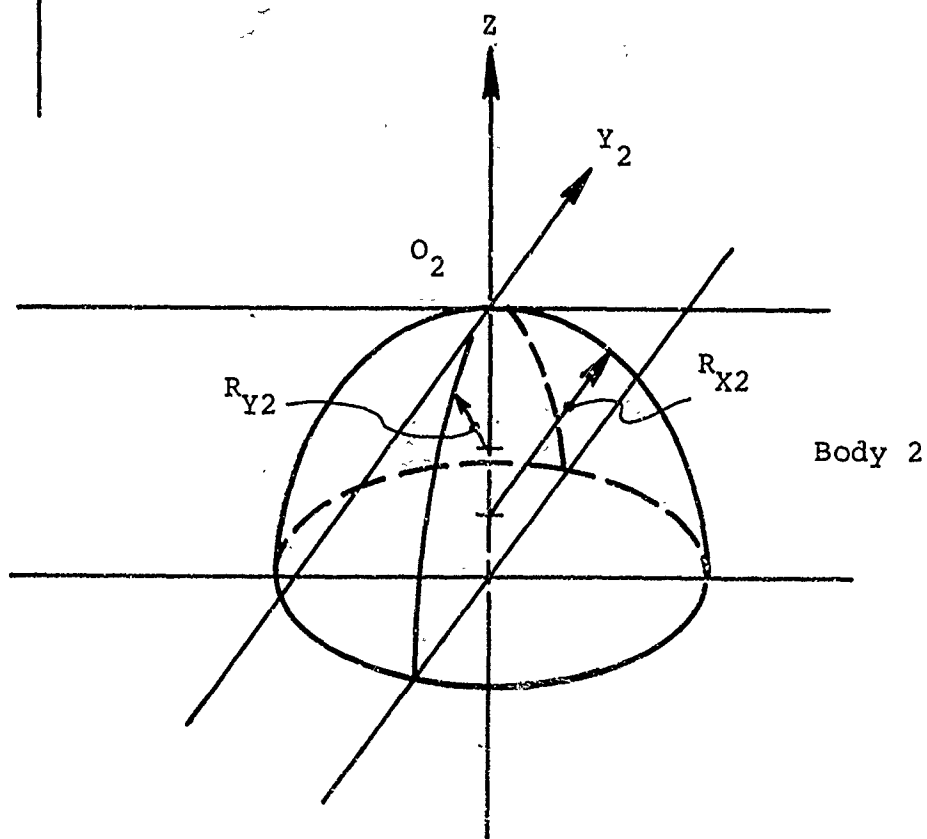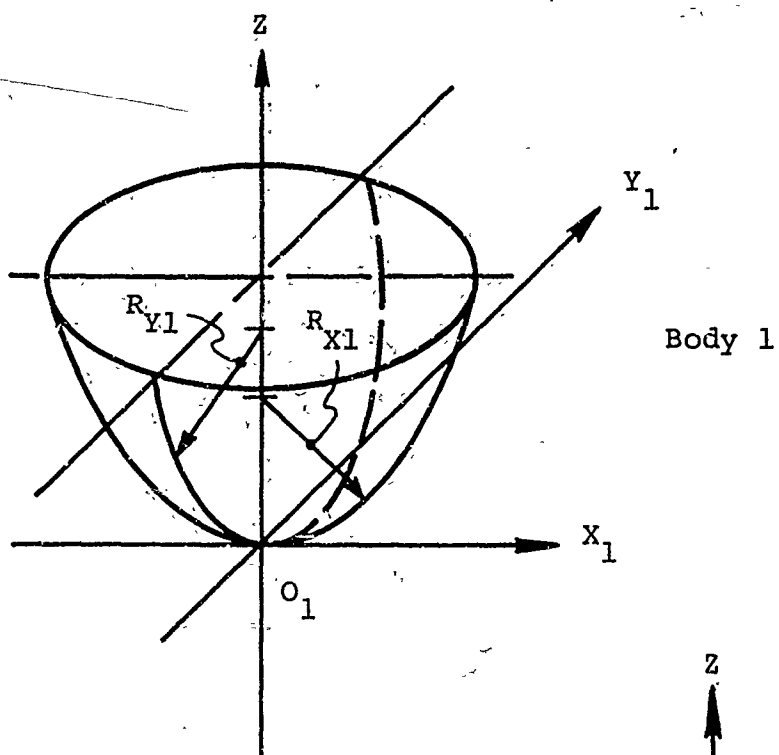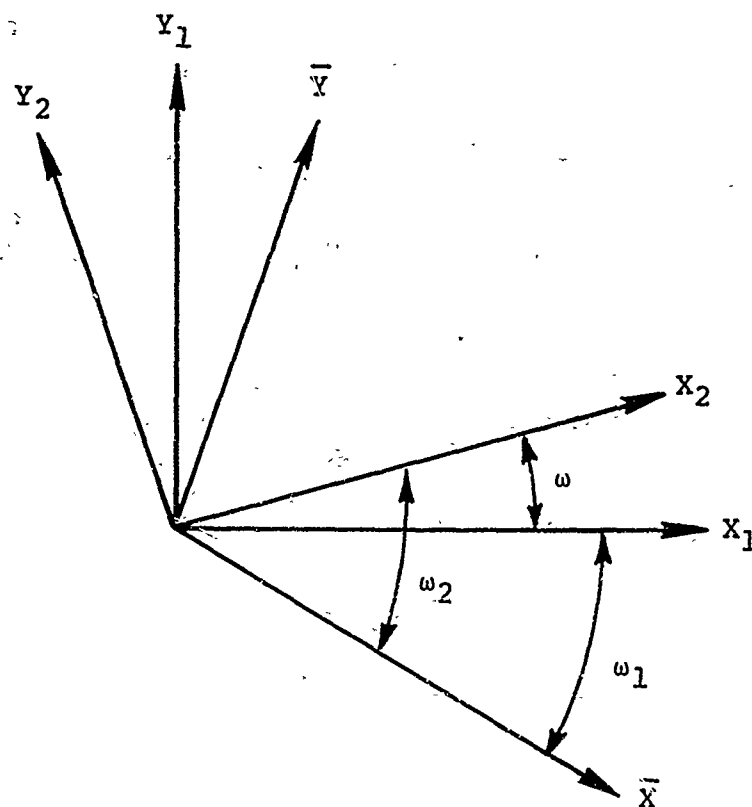Figure 74.   Two General Elastic Solids.

131

Figure 75.   Relationship of Pressure Area Axis
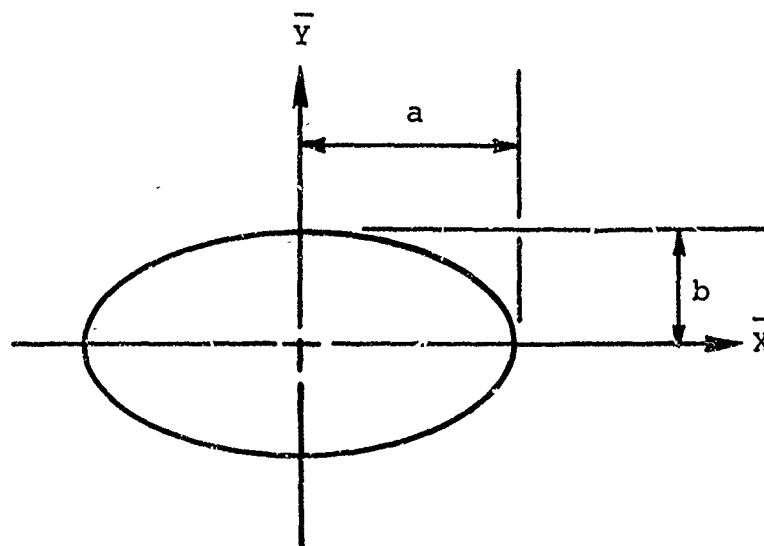and Body Axis.

Figure 76 .   Pressure Area Dimensions.

132

From Figure 75, we have

$$\omega_2 = \omega_1 + \omega \tag{102}$$

Let

$$A = \frac{1}{2}\left(\frac{1}{R_{X1}}\cos^2(\omega_1) + \frac{1}{R_{Y1}}\sin^2(\omega_1) + \frac{1}{R_{X2}}\cos^2(\omega_2)\right.$$

$$\left. + \frac{1}{R_{Y2}}\sin^2\omega_2\right) \tag{103}$$

$$B = \frac{1}{2}\left(\frac{1}{R_{X1}}\sin^2(\omega_1) + \frac{1}{R_{Y1}}\cos^2(\omega_1) + \frac{1}{R_{X2}}\sin^2(\omega_2)\right.$$

$$\left. + \frac{1}{R_{Y2}}\sin^2(\omega_2)\right) \tag{104}$$

Note that a convex curvature (with respect to the mating body) carries a positive sign and a concave curvature carries a negative sign.

For the flange/roller-end contact, the X_1 and X_2 axes are co-incident; therefore, the angle ω is zero, and Equations (103) and (104) can be reduced to

$$A = \frac{1}{2}\left(\frac{1}{R_{X1}} + \frac{1}{R_{X2}}\right) \tag{105}$$

$$B = \frac{1}{2}\left(\frac{1}{R_{Y1}} + \frac{1}{R_{Y2}}\right) \tag{106}$$

If the original choice of X and Y axis was correct, A will be less than B. If A is greater than B, the X and Y axis should be switched, and Equations (105) and (106) should be recalculated to be consistent with the following analysis.

The eccentricity of the contact ellipse, e, may be computed from

$$\frac{A}{B} = \frac{(1 - e^2)\ (\overline{K} - \overline{E})}{\overline{E} - (1 - e^2)\ \overline{K}} \tag{107}$$

133

$\overline{K}$ and $\overline{E}$ are the complete elliptic integrals of the first and second kinds, respectively:

$$\overline{K} = \frac{\pi}{2}\left(1 + \left(\frac{1}{2}\right)^2 e^2 + \left(\frac{1\cdot3}{2\cdot4}\right)^2 e^4 + \left(\frac{1\cdot3\cdot5}{2\cdot4\cdot6}\right)^2 e^6 + \ldots\right) \tag{108}$$

$$\overline{E} = \frac{\pi}{2}\left(1 + \left(\frac{1}{2}\right)^2 e^2 + \left(\frac{1\cdot3}{2\cdot4}\right)^2 e^4 + \left(\frac{1\cdot3\cdot5}{2\cdot4\cdot6}\right)^2 e^6 - \ldots\right) \tag{109}$$

For both Equations (108) and (109), $e^2 < 1$.

The value of e may be found by applying the Newton-Rhapson technique to Equation (108), which yields

$$e_i+1 = e_i + \frac{\left(A/B\ \left(\overline{E}_i-(1-e_i^2)\overline{K}_i\right)-(1-e_i^2)(\overline{K}_i-\overline{E}_i)\left(\overline{E}_i-(1-e_i^2)\overline{K}_i\right)\right)}{e_i\left(3\overline{E}_i^2-2(2-e_i^2)\overline{E}_i\overline{K}_i + (1-e_i^2)\overline{K}_i^2\right)} \tag{110}$$

Equation (111) may be solved iteratively to the desired accuracy. Starting values for Equation (110) may be chosen from the following table:

e	0.0	0.1	0.2	0.3	0.4	0.5	0.6	0.7	0.8	0.9	1.0
A/B	1.0	0.9	0.82	0.75	0.69	0.60	0.51	0.40	0.29	0.20	0.0

The dimensions of the pressure ellipse are

$$a = \left(\frac{3\ P_3\ (\overline{K}-\overline{E})}{2Ae^2}\left(\nu_R + \nu_E\right)\right)^{1/3} \tag{111}$$

$$b = a\ \sqrt{1-e^2} \tag{112}$$

The elastic approach (total combined deflection) along the Z axis for the roller-end/flange contact is

$$\delta_{RE} = \left(\frac{3\ P_3}{2a}\right)\left(\nu_E + \nu_R\right)\overline{K} \tag{113}$$

Finally, the maximum compressive stress is

$$S_{CRE} = \frac{-3\ P_3}{2\ \pi ab} \tag{114}$$

CONE RIB (FLANGE) SCORING FORMULA

The predominant mode of failure of high-speed tapered roller bearings is scoring at the roller-end/flange contact. This failure mode is very similar in appearance to scoring failures experienced in heavily loaded high-speed gears. Scoring failure is the momentary welding, tearing apart, and smearing of the contacting surfaces due to a breakdown of the lubricant film. The breakdown of lubricant film can be the result of insufficient oil supply or of the heat generated by the pressure and sliding occurring in the contact area.

High-capacity high-speed gearing which exhibits this mode of failure is analyzed for a flash temperature criterion. This concept has been applied to spur, helical, bevel, and hypoid gearing with encouraging results. This theory states that there exists, for each lubricant or family of lubricants, a critical instantaneous (flash) temperature beyond which the lubricant is no longer able to maintain a film separating the contacting surfaces. The calculation of this flash temperature is predicated upon certain basic assumptions:

- All heat flow is in a direction perpendicular to the plane of sliding.

- The thermal effect of the lubricant film itself is negligible.

- The elastic limit is not exceeded on either member.

- Neither contacting surface exhibits macroscopic irregularities.

- Both bodies are homogenious and isotropic.

- Both bodies have the same surface temperature at the contact point.

- Lubricant supply to the contact point is adequate.

The first item to be considered is the frictional heating generated between two semi-infinite bodies in contact. If we assume that the semi-infinite body 1 slides over body 2 with a velocity V_S while exerting a pressure P, and that a coefficient of friction f exists between them, the heat flux at the junction surfaces will be

$$q = P\ V_S\ f \tag{115}$$

If it is assumed that both bodies are at the same initial temperature and that the heat is distributed evenly between them, then the temperature rise on each body will be the same.

Bolk[5] has suggested the following formula for the temperature rise:

$$T = \frac{2}{\sqrt{\pi}} \frac{q\sqrt{t}}{C} \qquad (116)$$

where ΔT = temperature rise, °F
t = time of contact, sec
c = a thermal constant, in.-lb (in.^{2} °F sec$^{1/2}$)

and

$$C = C_P \, C_K \, \gamma_D \qquad (117)$$

C_P = specific heat, $\frac{\text{in.-lb}}{\text{lb °F}}$

C_K = thermal conductivity, $\frac{\text{in.-lb}}{\text{in. °F sec}}$

γ_D = weight density, lb/in.^{3}

For the temperature rise to be the same on body 1 and body 2, we have

$$\frac{2}{\sqrt{\pi}} \frac{q_1 \sqrt{t}}{C_1} = \Delta T = \frac{2}{\sqrt{\pi}} \frac{q_2 \sqrt{t}}{C_2} \qquad (118)$$

The total heat flux is

$$q_T = q_1 + q_2 \qquad (119)$$

Thus

$$q_1 = \frac{C_1}{C_1 + C_2} q_T \qquad (120)$$

$$q_2 = \frac{C_2}{C_1 + C_2} q_T \qquad (121)$$

which is an approximation of the heat flux distribution to each body.

Now consider two bodies[6] which are rolling and sliding on one another. It will be assumed that the temperature distributions on each body are identical at the contact point. The contact time is no longer the same for each body, and Equation (118) becomes

$$\frac{2}{\sqrt{\pi}} \, q_1 \, \frac{\sqrt{t_1}}{c_1} = \frac{2}{\sqrt{\pi}} \, q_2 \, \frac{\sqrt{t_2}}{c_2} \tag{122}$$

Now if d' is the width of the contact band in the direction of travel, and V_1 and V_2 are the linear velocities of bodies 1 and 2 respectively, we have

$$q_1 \, \frac{\sqrt{V_1/d'}}{c_1} = q_2 \, \frac{\sqrt{V_2/d'}}{c_2} \tag{123}$$

where V_1 and V_2 have the same sense and

where d' is the dimension of the pressure ellipse in the direction of travel.

Thus Equations (120) and (121) become

$$q_1 = \frac{c_1 \, \sqrt{V_1}}{c_1 \, \sqrt{V_1} + c_2 \, \sqrt{V_2}} \, q_T \tag{124}$$

$$q_2 = \frac{c_2 \, \sqrt{V_2}}{c_1 \, \sqrt{V_1} + c_2 \, \sqrt{V_2}} \, q_T \tag{125}$$

And the total heat generated is

$$\int_{A_c} q \, dA_c = \int_{A_c} P \, f \, V_S \, dA_c \approx \frac{\pi}{4} P_O \, f \, V_S \tag{126}$$

where P_O = maximum contact stress

Therefore, the flash temperature of the roller-end/flange contact is

$$\Delta T = \frac{\sqrt{\pi} \, P_O \, f \, V_S \, \sqrt{d}}{2 \left(c_1 \, \sqrt{V_1} + c_2 \, \sqrt{V_2} \right)} \tag{127}$$

The only parameter of the above equation which cannot be adequately defined at this time is the coefficient of friction between the roller end and the cone rib flange. Work published by Wren and Moyer[7] of Timken has shown that a coefficient of friction value of 0.005 has been established for this area of contact. Therefore, unti` additional data is generated for high-speed tapered roller bearings, the value of 0.005 will be used for calculating the flash temperature of the roller-end/ flange contact area.

137

CONE RIB LUBRICANT TRAJECTORY ANALYSIS

As the operating speed of a tapered roller bearing increases, the effects of centrifugal force on the oil passing through the bearing make it very difficult to maintain an adequate supply of oil at the roller-end/flange contact. High-speed photographs show that centrifugal force starves this area of lubricant when operating speeds exceed 10,000 fpm, as shown schematically in Figure 77. The most successful way to provide additional oil flow to this area is that of a secondary source of lubricant brought in through a hollow shaft, then out through radial holes into the shaft, and then into a manifold machined into the bore of the bearing. The manifold distributes the oil around the circumference of the shaft and then out through a number of radial holes in the cone, which provide oil to the undercut area of the cone rib flange.

In order to provide an even and adequate distribution of oil along the cone rib flange, the number, size, angle, and length of the holes machined into the cone must be carefully chosen. Inadequate design of these holes will limit the operating speed of the bearing because the oil will be dissipated away from the roller-end/flange contact before the roller reaches the next oil supply hole.

To insure that the oil lubrication holes are adequate in size and number, an anlaysis has been developed to determine the trajectory of the oil upon leaving the rib undercut area.

In cases to be considered in this analysis, the rib flange is attached to the inner race with small holes drilled from the manifold through the undercut between the flange and the inner race in order to provide lubricant flow to the roller-end/flange contact point by means of centrifugal pumping (i.e., Figure 78). Of particular interest is the calculation of the angle θ_0. This is the angle between the point at which the theoretical oil stream enters the flange area and the point at which it leaves the flange area. If this angle is small when compared with the angular spacing α_0 of the holes, the oil flow will essentially bypass the flange/roller-end contact and thus provide inadequate lubricant distribution in this area, which will be conducive to a scoring or starvation type failure. Adequate distribution is essential since much of our preceding analysis was based on the presence of sufficient lubricant in the area of contact.

The flow analysis of the oil in this area is very complex. Basically, three conditions are possible. If the flow rate possible through the flange holes is substantially higher than that possible through the shaft holes, then either a partially developed oil flow or an oil-air mixture flow will result (see Figure 79). If, as the oil passes through the shaft holes
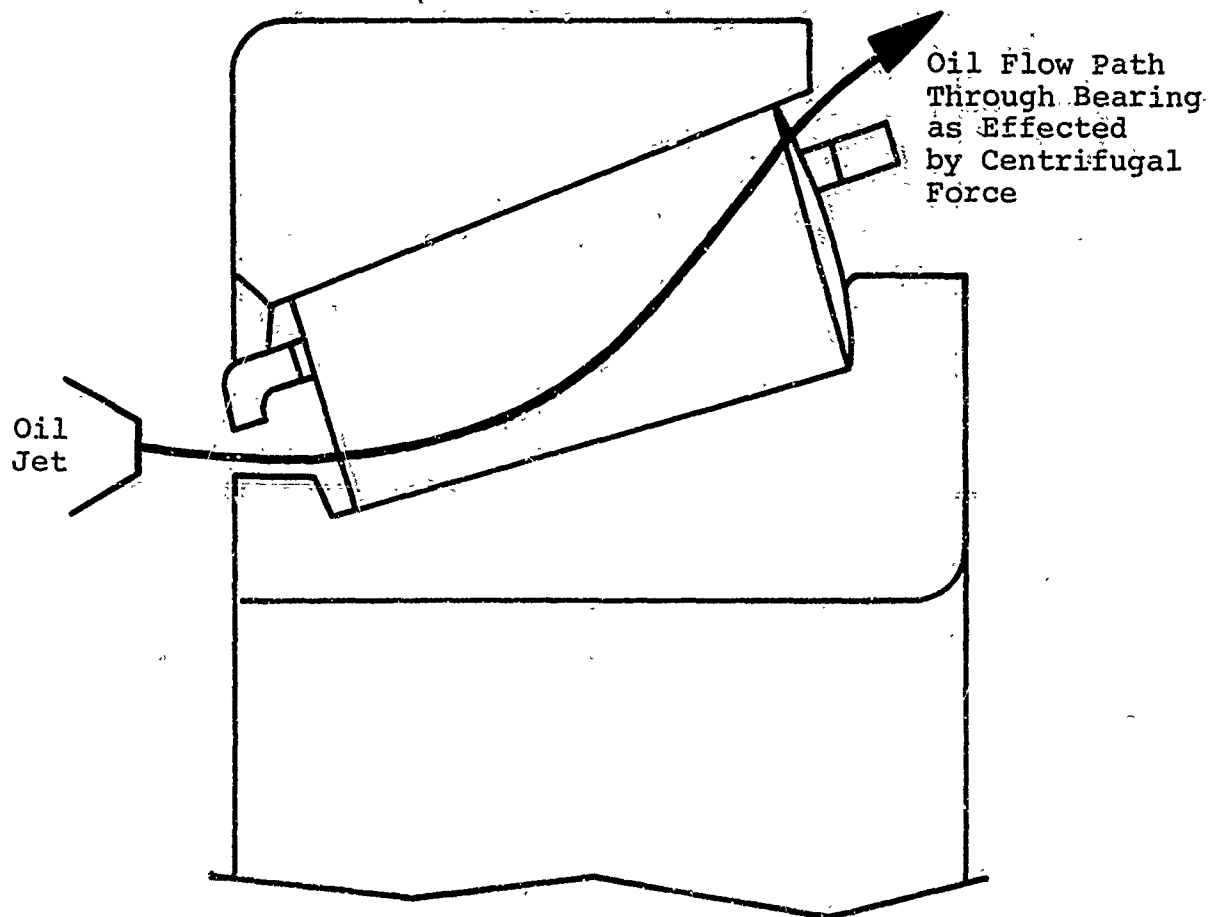
138

Figure 77. Oil Flow Path Within High-Speed Tapered Roller
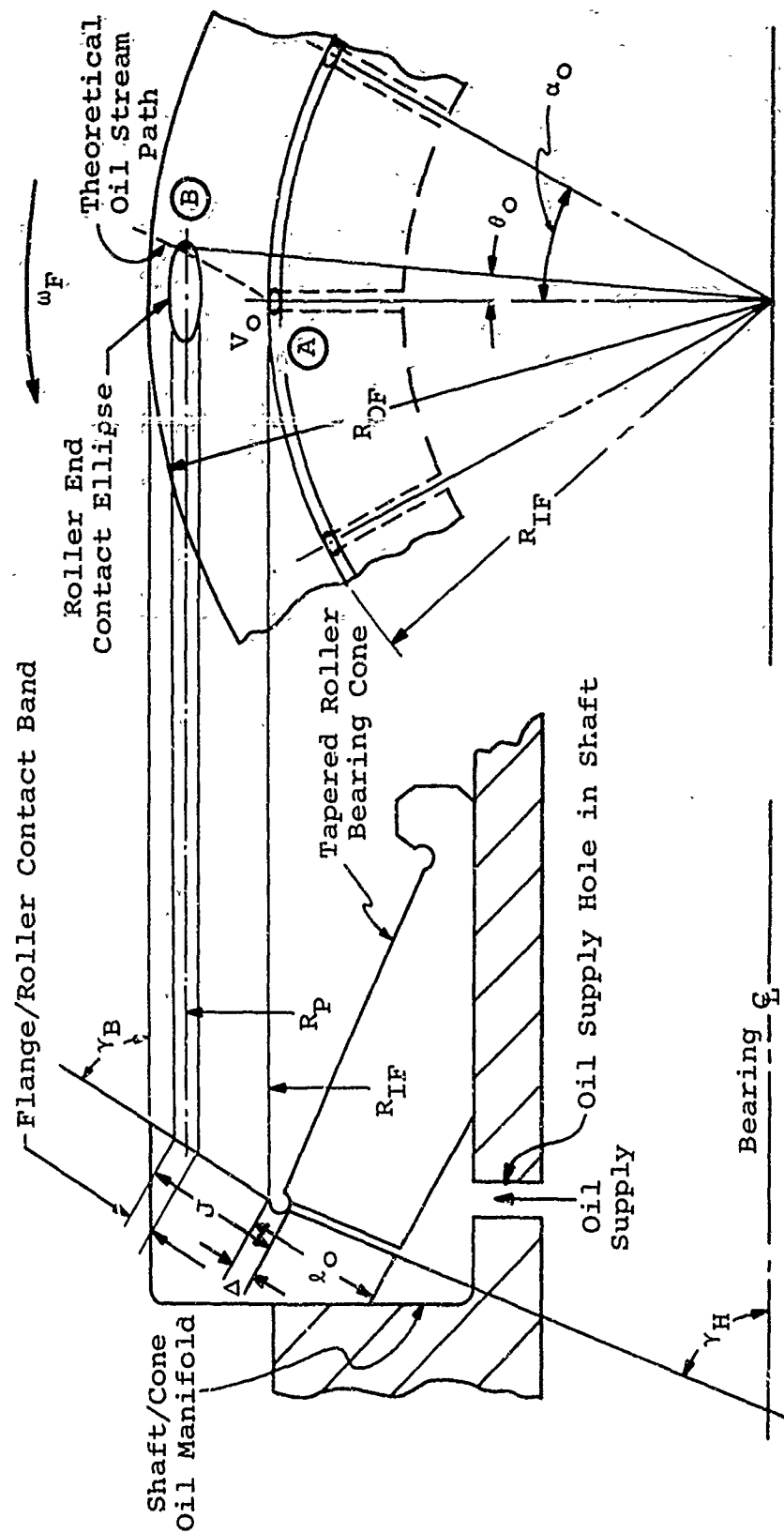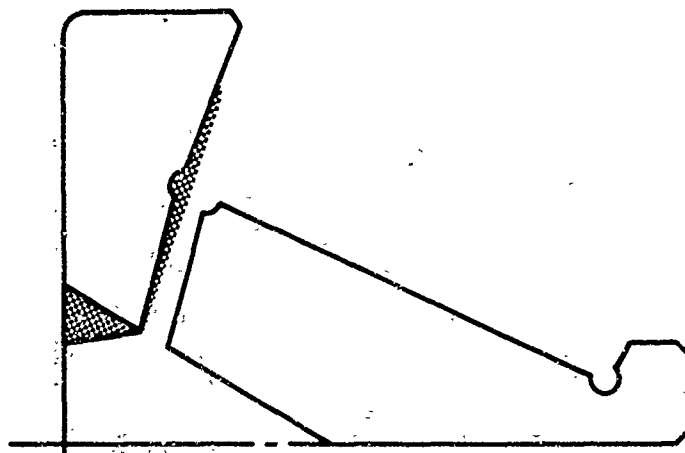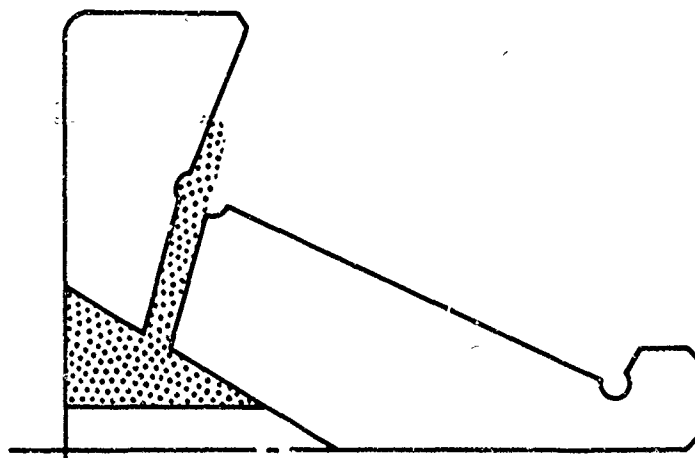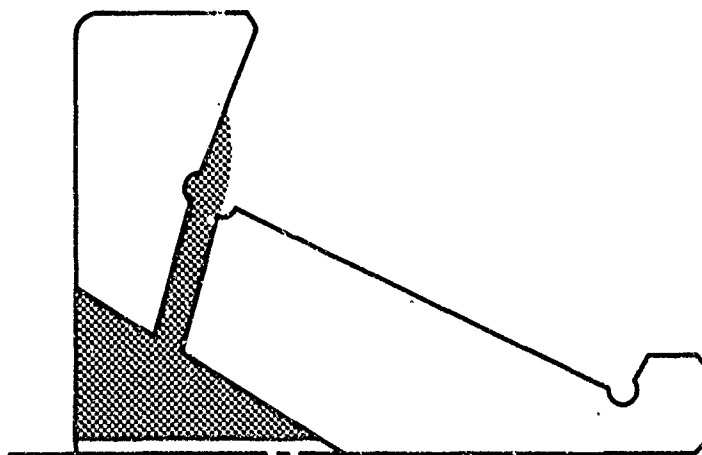Bearing Lubricated at Cone Small End Only.

Figure 78. Schematic of Second Source Lubrication System.

140

Partially Developed Oil Flow

Oil-Air Mixture Flow

Full Oil Flow

Figure 79.   Various Oil Flow Conditions to Cone Flange.

141

into the shaft-race cavity, the oil is not mixed with the air into an oil-air suspension, then the flow will be as shown in the upper drawing in Figure 79 with the only force acting on the fluid being the centrifugal force due to race rotation. If the oil and air are thoroughly mixed, then a condition similar to that shown in the center drawing in Figure 79 will exist. Finally, if the flow rate possible through the flange holes is less than or equal to that possible through the shaft holes, then a lubricant head will build up as shown in the lower drawing in Figure 79.

The velocity of the oil stream as it leaves the hole in the flange race undercut is dependent upon the conditions within the shaft-race cavity; however, once this velocity is known, the problem is identical regardless of the conditions in the cavity.

At the junction point of the inner race and the flange (see Figure 80) the oil stream has, in general, a velocity V_A which may be expressed as

$$V_A = \left(V_{AX}^2 + V_{AY}^2\right)^{1/2} \tag{128}$$

$$\gamma_O = \tan^{-1}\left(\frac{V_{AY}}{V_{AX}}\right) \tag{129}$$

where V_{AX} = the tangential velocity of the race at point A

V_{AY} = the velocity of the oil stream due to the action of centrifugal force as the oil moves up the inlet tube from point D to point A .

If we assume that the velocity V_A remains constant over the distance ℓ_F, we may easily calculate the time t_F required for a particle of oil to traverse this distance,

$$t_F = \ell_F/V_A \tag{130}$$

Knowing the time t_F we may now calculate the angle through which point C rotates during the time t_F,

$$\theta_O = \omega_I t_F \tag{131}$$

Referring to Figure 81, we will assume that the oil builds up in the cavity only to point D . It then spills over into the channel between points D and A . At point D it has
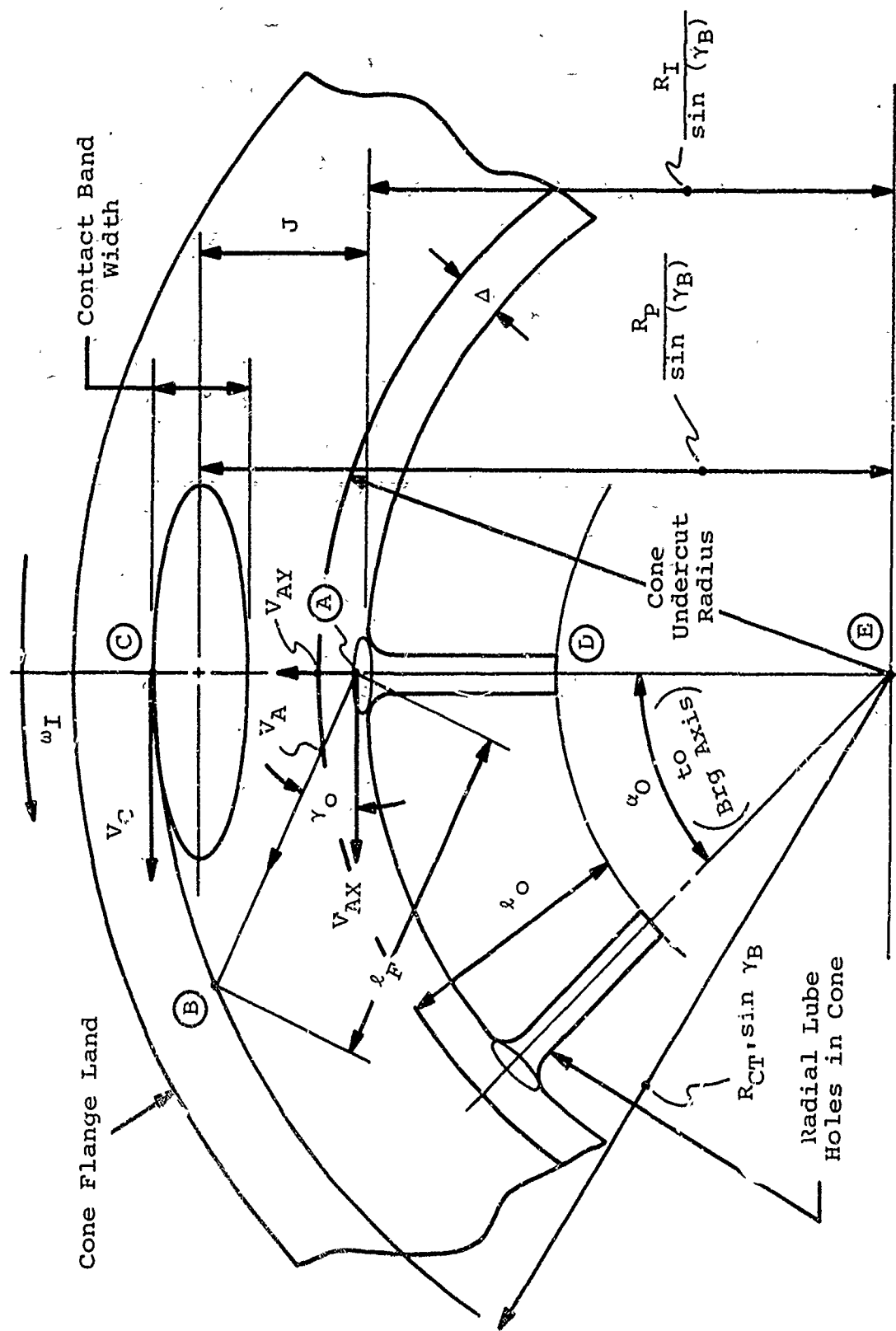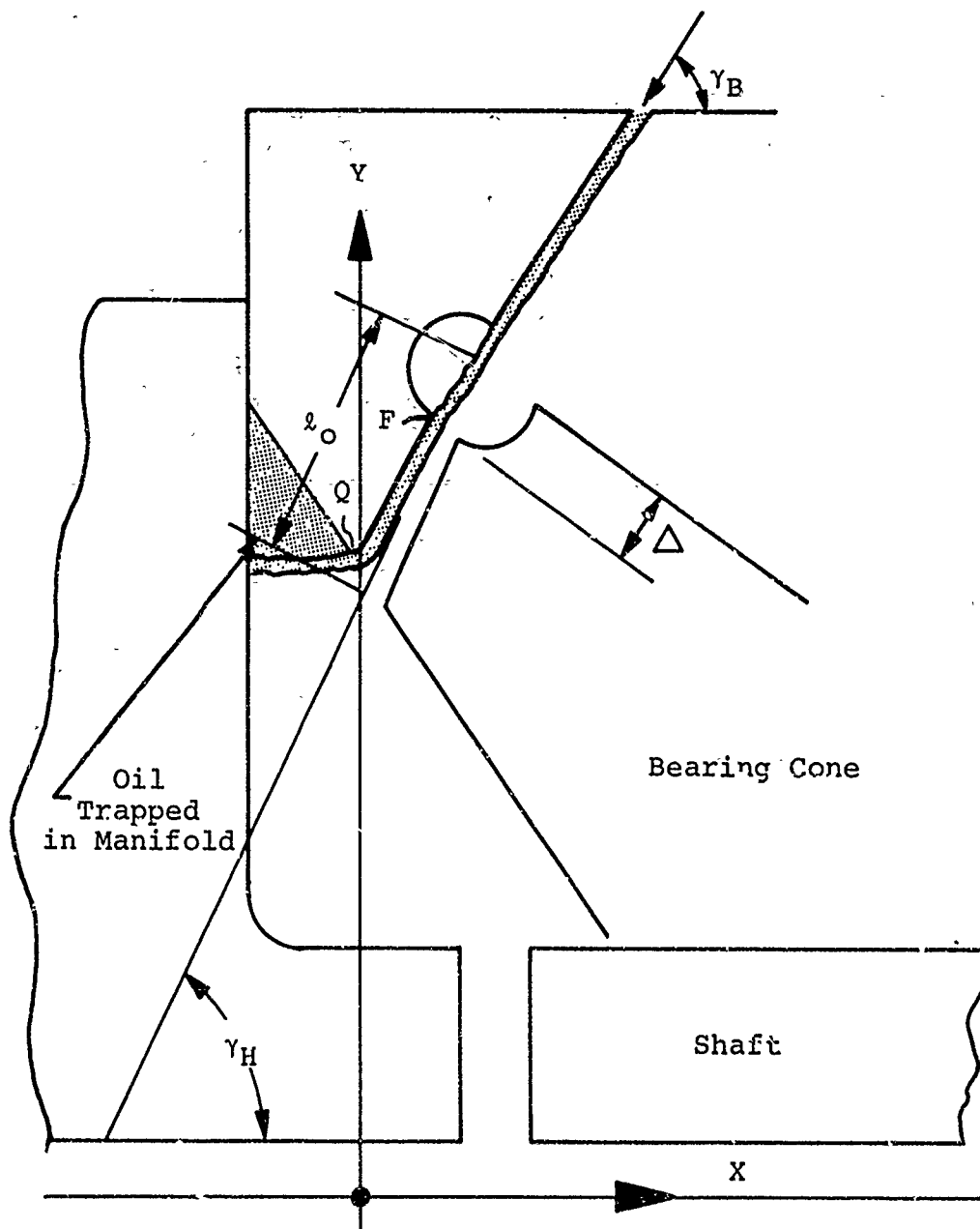
Figure 80. Oil Stream Velocity Diagram.

143

Figure 81. Oil Manifold Geometry.

144

essentially zero velocity in the Y direction. Along the distance ℓ_0 it is accelerated at a rate which is proportional to the square of its distance from the bearing centerline.

If the acceleration is a function of path distance ℓ, we have

$$V = (V_0^2 + 2 \int_{y_0}^{y} a \, dy)^{1/2} \tag{132}$$

where a = acceleration

V = velocity

y = distance

Integrating Equation (132) yields

$$V_{AY} = (V_0^2 + \omega_I^2 (y^2 - y_0^2))^{1/2} \tag{133}$$

where y_0 is the distance from the bearing centerline to the point D measured perpendicular to the bearing centerline; y is the distance to the point A ; and the velocity at point D is essentially zero so V_0 is zero.

$$y_0 = R_I - \ell_0 \sin(\gamma_H) \tag{134}$$

$$y = R_I - \Delta \tag{135}$$

where ℓ_0 is the overall length of the oil hole as shown in Figure 81 and Δ is the amount of undercut present.

The point of maximum usefulness of the oil for lubricating the roller-end contact is the point C . The point C is that point beyond which the lubricant stream is in the process of escaping from the roller-end/flange contact area. Depending on the orientation of the contact band, the radius to point C is calculated as follows:

$$R_{CT} = R_p + b \sin(\gamma_B); \quad (\gamma - \theta) > 0 \tag{136}$$

> (Pressure ellipse minor axis is in plane containing bearing axis.)

145

$$R_{CT} = R_P + a \sin(\gamma_B); \quad (\gamma - \theta) < 0 \tag{137}$$

(Pressure ellipse major axis is in plane containing bearing axis.)

If $(\gamma - \theta) = 0$, the pressure ellipse is a circle ($a = b$).

R_{CT} is perpendicular to the bearing axis.

Consider the triangle defined by points A, B, and E shown in Figure 80 and expanded in Figure 82; then

$$\theta_1 = \gamma_O + 90 \tag{138}$$

The X component of the velocity V_A is simply the tangential velocity of the flange at point A.

$$V_{AX} = \omega_I R_I \tag{139}$$

We may now turn our attention to the determin   of the oil stream velocity in the Y direction at point   . As stated earlier, the Y component of velocity at his point is a function of the conditions within the cavit . The most likely condition is that shown in Figure 7° top). In any event, it is unlikely that sufficient oil w   uild up in the cavity to enable us to consider the flow a   nating from a pressurized orifice. We will, therefore, analyze the flow as occurring purely as a result of centrifugal force.

The distance ℓ_F may be found by successive applications of the law of sines to the triangle shown in Figure 82:

$$\frac{R_{CT}}{\sin(\gamma_B)\sin(\theta_1)} = \frac{(R_I - \Delta)}{\sin(\gamma_B)\sin(\theta_3)} \tag{140}$$

Solving for θ_3 yields

$$\theta_3 = \sin^{-1}\left(\frac{R_F \sin(\theta_1)}{R_C}\right) \tag{141}$$

$$\theta_2 = \pi - \theta_1 - \theta_3 \tag{142}$$

$$\ell_F = \frac{R_{CT} \sin(\theta_2)}{\sin(\gamma_B)\sin(\theta_1)} \tag{143}$$
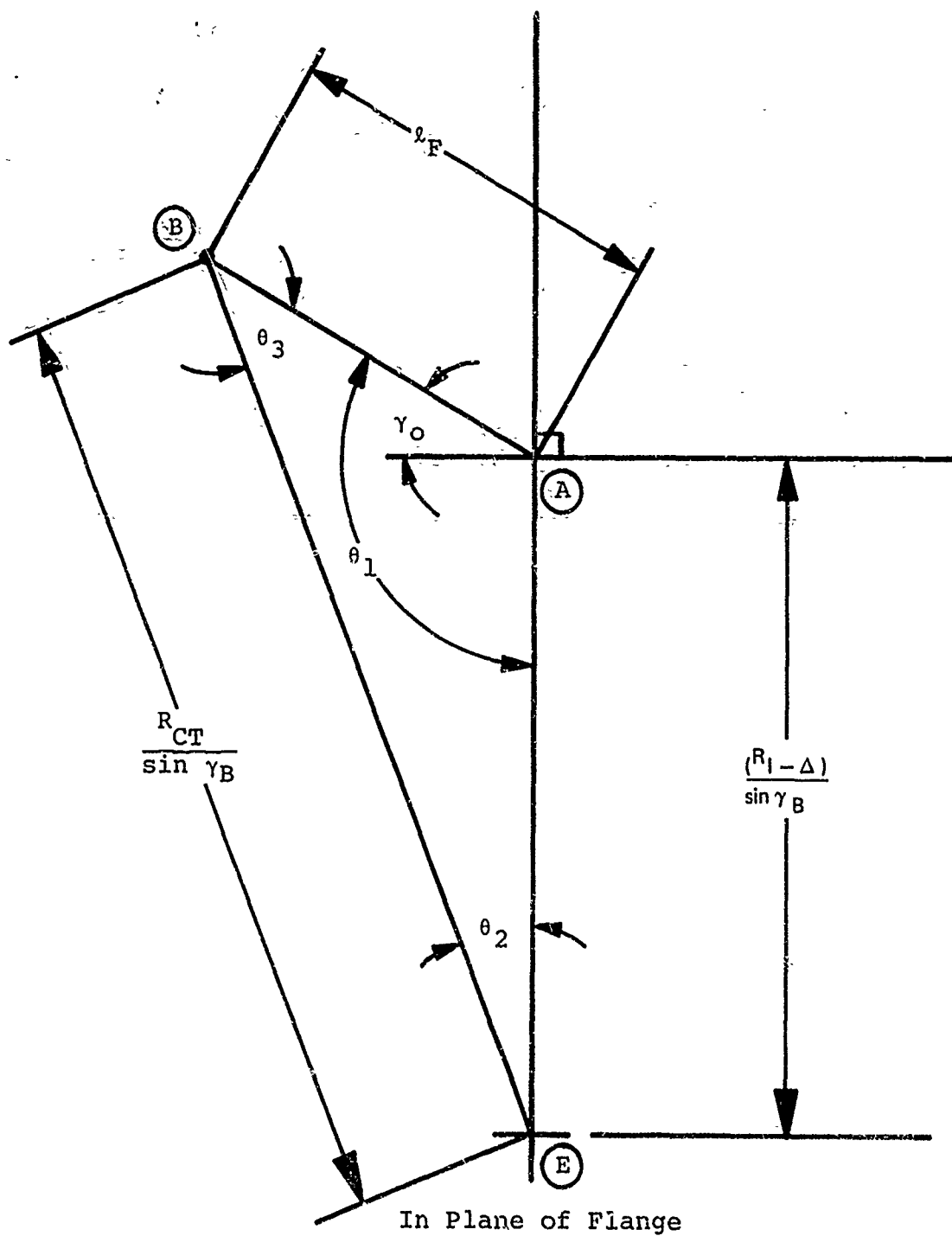
Figure 82. Diagram of Oil Path.

147

The velocity V_{AY} can be broken down into its radial and axial components,

$$V_{AXL} = V_{AY} \cos (\gamma_H) \tag{144}$$

and

$$V_{RADL} = V_{AY} \sin (\gamma_H) \tag{145}$$

where, as noted earlier, V_{AY} is the stream velocity along the flange and γ_H is the hole angle with respect to bearing center-line.

The ratio of the angle θ_O to the angular spacing of the second-source lubricant holes is of interest in evaluating the effectiveness of the second lube source in providing adequate lubrication coverage of the cove flange. This ratio is

$$R_O' = \frac{\theta_O}{\alpha_O} \tag{146}$$

where α_O = angular spacing of the holes

Of considerable interest and value in appraising the accuracy of the foregoing section is a knowledge of the full oil flow capability of the holes in the bearing race flange intersection. A first approximation of this flow may be obtained by calculating the flow through the hole by utilizing the velocity of the stream at the outlet point as calculated by Equation (133).

The product of area and velocity yields volume flow

$$Q_H = N_H A_H V_{AY} C_{DH} \tag{147}$$

where N_H = number of second-source lube holes

C_{DH} = discharge coefficient of the hole

A_H = cross-sectional area of second-source lube holes

The flow may be expressed in gallons per minute by utilizing appropriate conversion factors, so if A_H is in in.^{3} and V_{AY} is in in./sec we have

$$Q_{HT} = N_H A_H V_{AY} C_{DH} \frac{(60 \text{ sec})}{\text{min}} \frac{(1 \text{ gal})}{231 \text{ in.}^3} \tag{148}$$

148

The total flow is then given by

$$Q_{HT} = 0.204 \; N_H \; C_{DH} \; V_{AY} \; D_H^2 \quad \text{(GPM)} \tag{149}$$

where D_H = diameter of second-source lube holes

In general, the flange surface and the centerline of the oil holes at the junction of the inner race and the flange will not be at the same angle with respect to the bearing axis; thus the oil stream from these holes will not necessarily hit the contact point exactly. A second measure of the effectiveness of the oil stream in providing lubrication to the roller-end/flange contact may be obtained by forming the ratio of ℓ_m to ℓ_m' as shown in Figure 83. If this ratio is zero, the stream is aimed directly at the contact point. If this ratio is greater than 0.0, the stream is aimed at some point on the roller end curvature between the contact point and the inner race. If this ratio is less than 0.0, the stream is aimed at the flange between the inner race and the contact point.

From Figure 83, we have

$$\ell_m' = R_E \; [1 - \cos(\theta'')/\cos(\theta)] \tag{150}$$

The cone distance is

$$C_E = E/(2 \sin(\gamma)) + \ell/2 \tag{151}$$

therefore,

$$R_I' = [C_E - R_E \cos(\theta'')] \sin(\gamma) \tag{152}$$

But

$$L_T' = R_I/\tan(\alpha) - R_I'/\tan(\gamma) + (R_I - R_I')/\tan(\gamma_H) \tag{153}$$

Employing the law of sines yields

$$\ell_m = R_E - \frac{L_T' \sin(\gamma_H)}{\sin(180 - \gamma_H + \theta)} \tag{154}$$

The desired ratio is then

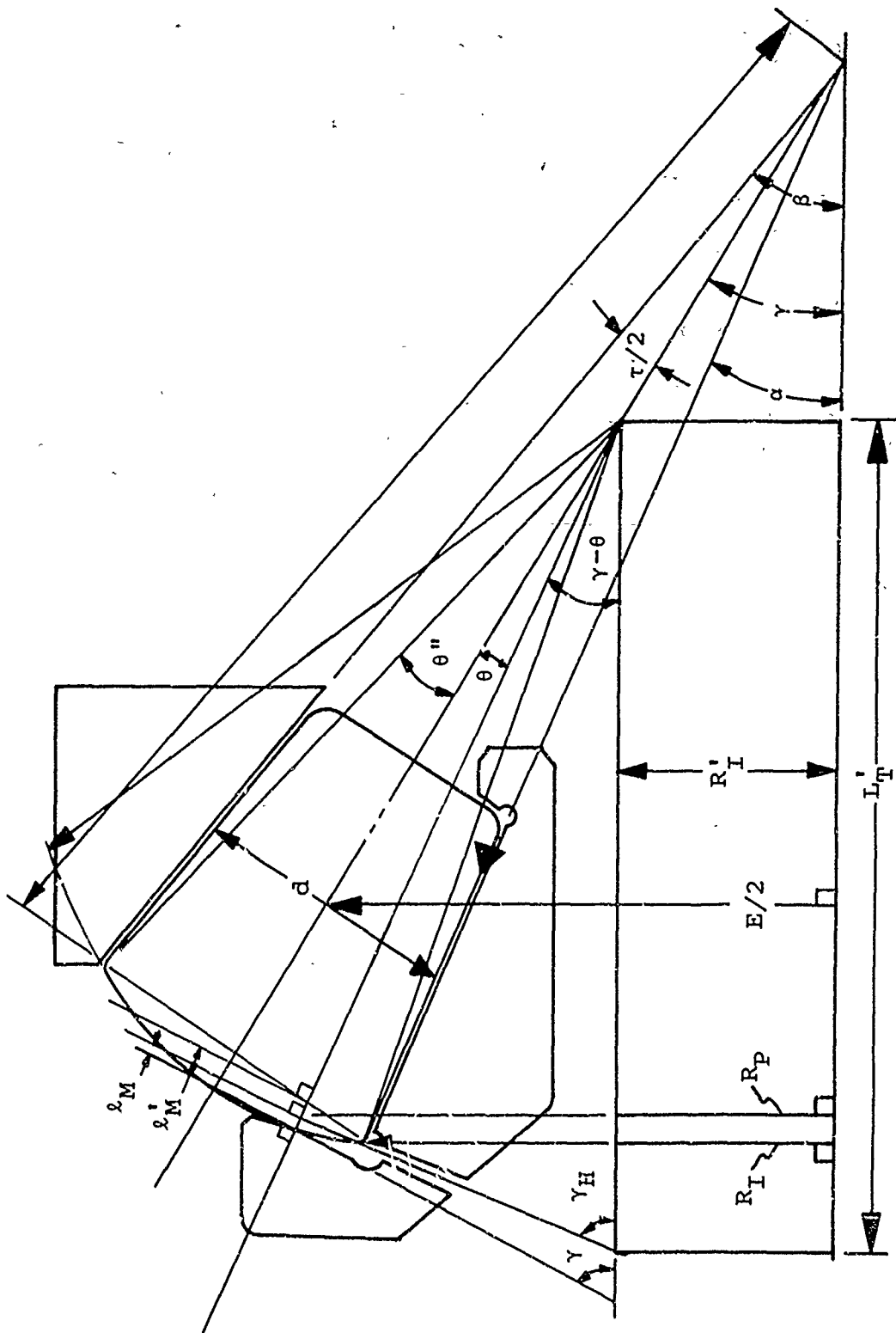$$R_\ell = \ell_m/\ell_m' \tag{155}$$

149

Figure 83. Basic Angle and Dimension of Oil Manifold.

150

HIGH-SPEED TAPERED ROLLER BEARING FATIGUE LIFE ANALYSIS

Figure 82 illustrates a tapered roller bearing and defines some of the nomenclature.

In conventional tapered roller bearings the large end is spherical with the center of the sphere on the roller axis. In Figure 84 the center of the roll-end arc is not on the axis of the roller in order to allow for variation in the angle θ.

P_1 and P_2 are the outer and inner race contact forces. M_1 and M_2 are contact moments resulting from misalignments of roller and raceways. P_3 is the reaction from the guide flange. F_C and M_G are the centrifugal force and gyroscopic moment acting on the roller at the mass center.

Figure 85 shows the five displacements that the inner ring may have with respect to the outer. The sixth degree of freedom is the rotation of the inner ring about its axis.

Looking along X from right to left the rollers are numbered sequentially clockwise with No. 1 roller at the top. Then the azimuth of the qth roller is

$$\psi_q = \frac{2\pi\ (q-1)}{n} \tag{156}$$

The approach of inner race to the outer is evaluated along the roller's mid-diameter and is

$$\Delta_q = \left[\delta_1' + \frac{E}{2}\ (\delta_4'\ \cos(\phi_q) + \delta_5'\ \sin(\phi_q)\right] \sin\ (\beta - \frac{\tau}{2}) +$$

$$\left[\delta_2'\ \sin(\phi) + \delta_3'\ \cos(\phi) - \frac{P_D}{2}\right] \cos\ (\beta - \frac{\tau}{2}) \tag{157}$$

The relative misalignment of outer and inner races is

$$\alpha_q = \delta_4'\ \cos(\phi_q) + \delta_5'\ \sin\ (\phi_q) \tag{158}$$

In order to determine the equilibrium position of the roller between the races, assumptions of the roller's approach to the outer race Δ_1 and its misalignment α_1 with respect to the outer race are made. Then

$$\Delta_1\ \cos(\frac{\tau}{2}) + \Delta_2\ \cos\ (\frac{\tau}{2}) = \Delta_q \tag{159}$$

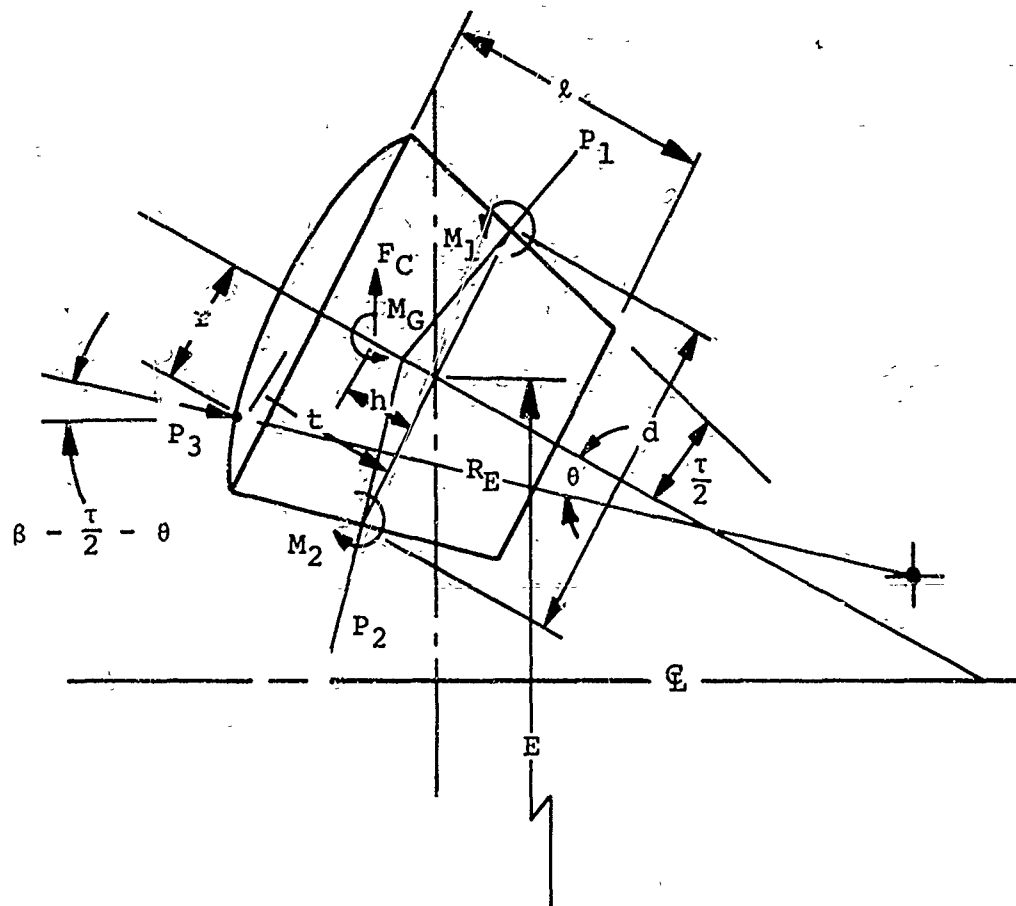$$\alpha_1 + \alpha_2 = \alpha_q \tag{160}$$
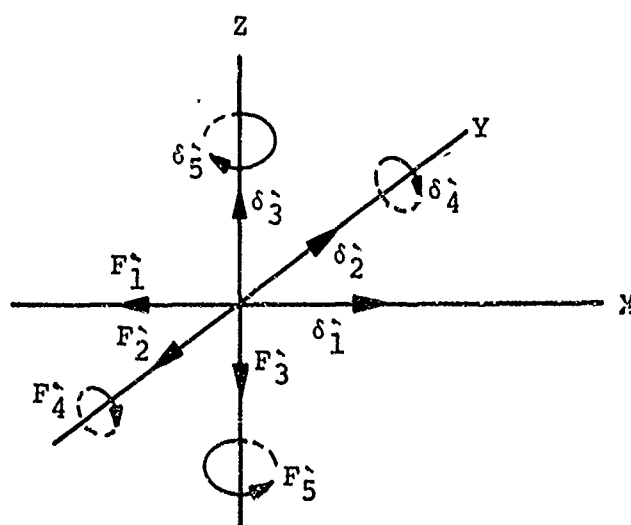
Figure 84.   Tapered Roller Loading Diagram.

Figure 85.   Force - Displacement Diagram.

152

For purposes of determining the length of the contact pattern between roller and race, the geometric intersections of roller and race shapes are needed.

The distance from the midpoint of the roller to a contact extremity measured along the element of the cone is

$$Y_i = \alpha_j \left(R_C^2 - \left(\frac{\ell_F}{2}\right)^2\right)^{1/2} \pm \left(R_C^2 - \left(\left(R_C^2 - \left(\frac{\ell_F}{2}\right)^2\right)^{1/2} - \Delta_j\right)^2\right)^{1/2} \quad J=1,2 \quad (161)$$

Y_1 is the left-most extremity and takes the positive sign of the radical. ℓ_F is the flat length and may be zero. R_C is the roller crown radius.

If $\quad |Y_i| > (\frac{\ell}{2} - C_{RAD})$

$$Y_i = \pm (\frac{\ell}{2} - C_{RAD}) \qquad (162)$$

If the roller has a flat length and the intersection falls within the flat

$$Y_i = - \frac{\Delta_j}{\alpha_j} \qquad J=1,2 \qquad (163)$$

The approach of the roll body to the race at a distance X from the midpoint of the roller is

$$\Delta_X = \Delta_j + X\alpha_j \qquad (164)$$

If $|X| > \dfrac{\ell_F}{2}$ the approach is

$$\Delta_X = \Delta_j + \left(R_C^2 - \left(X - \alpha_j \left(R_C^2 - \left(\frac{\ell_F}{2}\right)^2\right)^{1/2}\right)^2\right)^{1/2} - \left(R_C^2 - \left(\frac{\ell_F}{2}\right)^2\right)^{1/2} \quad (165)$$

Lundberg[9] gives the approach Δ_X as a function of the load per unit length P_X as

$$\Delta_X = \frac{(\nu_R + \nu_E)}{2\pi} P_X \left(1.8864 + \text{Log}_e \left(\frac{(Y_1 - Y_2)}{2\,b_X}\right)\right) \qquad (166)$$

b_X is the semiwidth of the pattern at point X

$$b_X = \left(\frac{(\nu_R + \nu_E)}{2\pi} P_X (1 + C_j\, \gamma_X)\, d_X\right)^{1/2} \qquad (167)$$

$$C_1 = +1 \tag{168}$$

$$C_2 = -1 \tag{169}$$

$$\gamma_{X_1} = \frac{d_X \cos(\beta)}{E_{X_1}} \quad \text{for outer race} \tag{170}$$

$$\gamma_{X_2} = \frac{d_X \cos(\beta-\tau)}{E_{X_2}} \quad \text{for inner race} \tag{171}$$

E_X is the pitch diameter at location X and d_X the roll diameter for elastic calculations at that point.

$$d_X = \frac{d + 2X \sin\left(\frac{\tau}{2}\right)}{\cos\left(\frac{\tau}{2}\right)} \tag{172}$$

$$E_{X_1} = \frac{E + 2X \sin\left(\frac{\tau}{2}\right)\tan\left(\beta-\frac{\tau}{2}\right)}{\cos(\beta)} \quad \text{for outer} \tag{173}$$

$$E_{X_2} = \frac{E + 2X \sin\left(\frac{\tau}{2}\right)\tan\left(\beta-\frac{\tau}{2}\right)}{\cos(\beta-\tau)} \quad \text{for inner} \tag{174}$$

The loading P_X is obtained by iteration of Equation (175):

$$pX_n = pX_{n-1} - \frac{\left(\Delta X_{n-1} - \Delta \overset{*}{X}\right)}{\left.\frac{dp_X}{d\Delta_X}\right|_{n-1}} \tag{175}$$

where $\Delta_X^* = $ the given value of deflection at X

From Equation (166), we see that

$$\frac{dp_X}{d\Delta_X} = \frac{2\pi}{(\nu_R + \nu_E)\left(1.3864 + \text{Log}_e\left(\frac{(Y_1 - Y_2)}{2b_X}\right)\right)} \tag{176}$$

The total contact load P and the moment M are

$$P = \int_{Y_2}^{Y_1} p_X dX \tag{177}$$

$$M = \int_{Y_2}^{Y_1} P_X \, X \, dX \tag{178}$$

The derivatives of P and M with respect to Δ_j and α_j are required:

$$\frac{dP_j}{d\Delta_j} = \int_{Y_2}^{Y_1} \frac{dP_X}{d\Delta_X} \, dX \tag{179}$$

$$\frac{dP_j}{d\alpha_j} = \int_{Y_2}^{Y_1} \frac{dP_X}{d\Delta_X} \frac{d\Delta_X}{d\alpha_j} \, dX \tag{180}$$

$$\frac{dM_j}{d\Delta_j} = \int_{Y_2}^{Y_1} \frac{dP_X}{d\Delta_X} \, X \, dX \tag{181}$$

$$\frac{dM_j}{d\alpha_j} = \int_{Y_2}^{Y_1} \frac{dP_X}{d\Delta_X} \frac{d\Delta_X}{d\alpha_j} \, X \, dX \tag{182}$$

From Equation (164), when $|X| \leq \frac{\ell_F}{2}$, we find that

$$\frac{d\Delta_X}{d\alpha_j} = X \tag{183}$$

and from Equation (165), when $|X| > \frac{\ell_F}{2}$, we see

$$\frac{d\Delta_X}{d\alpha_j} = \frac{\left(X - \alpha_j \left(R_C^2 - \left(\frac{\ell_F}{2}\right)^2\right)^{1/2}\right)\left(R_C^2 - \left(\frac{\ell_F}{2}\right)^2\right)^{1/2}}{\left(R_C^2 - \left(X - \alpha_j \left(R_C^2 - \left(\frac{\ell_F}{2}\right)^2\right)^{1/2}\right)^2\right)^{1/2}} \tag{184}$$

From Figure 84, we obtain

$$-P_1 \cos(\beta) + P_2 \cos(\beta - \tau) - P_3 \sin\left(\beta - \frac{\tau}{2} - \theta\right) + CF = \psi_1 \doteq 0 \tag{185}$$

$$-P_1 \sin(\beta) + P_2 \sin(\beta - \tau) + P_3 \cos\left(\beta - \frac{\tau}{2} - \theta\right) = \psi_2 \doteq 0 \tag{186}$$

Taking moments about the roll center yields

$$P_3 = \frac{CF\ h\ \cos(\beta - \frac{\tau}{2}) - GM - M_1 + M_2 - \frac{(P_1 - P_2)d\ \sin(\frac{\tau}{2})}{2}}{r\ \cos(\theta) - t\ \sin(C)} \tag{187}$$

Equations (185) and (186) comprise a set of nonlinear simultaneous equations in which the variables are Δ_1 and α_1. They can be linearized and solved by iteration of

$$\Delta_{1_n} = \Delta_{1_{n=1}} - \frac{\begin{vmatrix} \psi_1 & \dfrac{d\psi_1}{d\alpha_1} \\[3mm] \psi_2 & \dfrac{d\psi_2}{d\alpha_1} \end{vmatrix}_{n-1}}{D_{n-1}} \tag{188}$$

$$\alpha_{1_n} = \alpha_{1_{n-1}} - \frac{\begin{vmatrix} \dfrac{d\psi_1}{d\Delta_1} & \psi_1 \\[3mm] \dfrac{d\psi_2}{d\Delta_1} & \psi_2 \end{vmatrix}_{n-1}}{D_{n-1}} \tag{189}$$

D is the determination of the coefficient matrix

$$D = \begin{vmatrix} \dfrac{d\psi_1}{d\Delta_1} & \dfrac{d\psi_1}{d\alpha_1} \\[3mm] \dfrac{d\psi_2}{d\Delta_1} & \dfrac{d\psi_2}{d\alpha_1} \end{vmatrix} \tag{190}$$

From Equations (185) and (186), we have

$$\frac{d\psi_1}{d(\Delta_1, \alpha_1)} = \frac{-dP_1}{d(\Delta_1, \alpha_1)}\ \cos(\beta) - \frac{dP_2}{d(\Delta_2, \alpha_2)}\ \cos(\beta - \tau)$$

$$- \frac{dP_3}{d(\Delta_1, \alpha_1)}\ \sin\left(\beta - \frac{\tau}{2} - \theta\right) \tag{191}$$

156

$$\frac{d\psi_2}{d(\Delta_1, \alpha_1)} = -\frac{dP_1}{d(\Delta_1, \alpha_1)} \sin(\beta) - \frac{dP_2}{d(\Delta_2, \alpha_2)} \sin(\beta - \tau)$$

$$+ \frac{dP_3}{d(\Delta_1, \alpha_1)} \cos(\beta - \frac{\tau}{2} - \theta) \tag{192}$$

And from Equation (187)

$$\frac{dP_3}{d(\Delta_1, \alpha_1)} = \frac{-\frac{dM_1}{d(\Delta_1, \alpha_1)} - \frac{dM_2}{d(\Delta_2, \alpha_2)} - \frac{1}{2}\left(\frac{dP_1}{d(\Delta_1, \alpha_1)} + \frac{dP_2}{d(\Delta_2, \alpha_2)}\right) d \sin(\frac{\tau}{2})}{r \cos(\theta) - t \sin(\theta)}$$

$$\tag{193}$$

The reactions of the bearing on the shaft in the plane of the rollers' midlengths are shown in Figure 85 and are

$$F_1' = \sin \beta \sum_{q=1}^{n} P_{1_q} \tag{194}$$

$$F_2' = \cos \beta \sum_{q=1}^{n} P_{1_q} \sin\left(\frac{2\pi}{n}(q-1)\right) \tag{195}$$

$$F_3' = \cos \beta \sum_{q=1}^{n} P_{1_q} \cos\left(\frac{2\pi}{n}(q-1)\right) \tag{196}$$

$$F_4' = \sum_{q=1}^{n} \left(\frac{P_{1q}}{2}(E \sin \beta) + d \sin(\frac{\tau}{2}) + M_{1_q}\right)\cos\left(\frac{2\pi}{n}(q-1)\right) \tag{197}$$

$$F_5' = \sum_{q=1}^{n} \left(\frac{P_{1q}}{2}(E \sin \beta + d \sin(\frac{\tau}{2}) + M_{1_q}\right) \sin\left(\frac{2\pi}{n}(q-1)\right) \tag{198}$$

The derivatives of the F_j' with respect to the displacements at the bearing center are required. However, it is necessary to first find $\frac{d\alpha_1}{d(\Delta, \alpha)}$ and $\frac{d\Delta_1}{d(\Delta, \alpha)}$.

157

Differentiating Equations (185), (186), (159), and (160) with
respect to Δ and α gives four simultaneous equations which are
linear in the desired derivatives and from which the following
may be obtained.

The elements of the coefficient matrix are

$$a_{11} = -\frac{dP_1}{d\Delta_1} \cos(\beta) - \frac{\partial P_3}{\partial \Delta_1} \sin\left(\beta - \frac{\tau}{2} - \theta\right) \tag{199}$$

$$a_{12} = \frac{dP_2}{d\Delta_2} \cos(\beta - \tau) - \frac{\partial \bar{P}_3}{\partial \Delta_2} \sin\left(\beta - \frac{\tau}{2} - \theta\right) \tag{200}$$

$$a_{13} = -\frac{dP_1}{d\alpha_1} \cos(\beta) - \frac{\partial P_3}{\partial \alpha_1} \sin\left(\beta - \frac{\tau}{2} - \theta\right) \tag{201}$$

$$a_{14} = \frac{dP_2}{d\alpha_2} \cos(\beta - \tau) - \frac{\partial P_3}{\partial \alpha_2} \sin\left(\beta - \frac{\tau}{2} - \theta\right) \tag{202}$$

$$a_{21} = -\frac{dP_1}{d\Delta_1} \sin(\beta) + \frac{\partial P_3}{\partial \Delta_1} \cos\left(\beta - \frac{\tau}{2} - \theta\right) \tag{203}$$

$$a_{22} = \frac{dP_2}{d\Delta_2} \sin(\beta - \tau) + \frac{\partial P_3}{\partial \Delta_2} \cos\left(\beta - \frac{\tau}{2} - \theta\right) \tag{204}$$

$$a_{23} = -\frac{dP_1}{d\alpha_1} \sin(\beta) + \frac{\partial P_3}{\partial \alpha_1} \cos\left(\beta - \frac{\tau}{2} - \theta\right) \tag{205}$$

$$a_{24} = \frac{dP_2}{d\alpha_2} \sin(\beta - \tau) \quad \frac{\partial P_3}{\partial \alpha_2} \cos\left(\beta - \frac{\tau}{2} - \theta\right) \tag{206}$$

$$a_{31} = 1 \tag{207}$$

$$a_{32} = 1 \tag{208}$$

$$a_{33} = 0 \tag{209}$$

$$a_{34} = 0 \tag{210}$$

$$a_{41} = 0 \tag{211}$$

$$a_{42} = 0 \tag{212}$$

$$a_{43} = 1 \tag{213}$$

$a_{44} = 1$ (214)

The partial derivatives of P_3 required above are

$$\frac{\partial P_3}{\partial \alpha_1} = \frac{-\frac{dM_1}{d\Delta_1} - \frac{1}{2}\frac{dP_1}{d\Delta_1} d \sin\left(\frac{\tau}{2}\right)}{r \cos(\theta) - t \sin(\theta)}$$ (215)

$$\frac{\partial P_3}{\partial \Delta_1} = \frac{-\frac{dM_1}{d\alpha_1} - \frac{1}{2}\frac{dP_1}{d\alpha_1} d \sin\left(\frac{\tau}{2}\right)}{r \cos(\theta) - t \sin(\theta)}$$ (216)

$$\frac{\partial P_3}{\partial \alpha_2} = \frac{\frac{dM_2}{d\Delta_2} + \frac{1}{2}\frac{dP_2}{d\Delta_2} d \sin\left(\frac{\tau}{2}\right)}{r \cos(\theta) - t \sin(\theta)}$$ (217)

$$\frac{\partial P_3}{\partial \Delta_2} = \frac{\frac{dM_2}{d\alpha_2} + \frac{1}{2}\frac{dP_2}{d\alpha_2} d \sin\left(\frac{\tau}{2}\right)}{r \cos(\theta) - t \sin(\theta)}$$ (218)

The vector of constants when differentiating with respect to Δ is

$V_1 = 0$ (219)

$V_2 = 0$ (220)

$V_3 = \frac{1}{\cos\left(\frac{\tau}{2}\right)}$ (221)

$V_4 = 0$ (222)

The vector of the unknowns is

$$\{X_i\} = [a_{ij}]^{-1}\{V_j\}$$ (223)

X_1 is $\frac{d\Delta_1}{d\Delta}$ and X_3 is $\frac{d\alpha_1}{d\Delta}$

If the vector of constants is changed to

$V_1 = 0$ (224)

$V_2 = 0$ (225)

159

$$V_3 = 0 \tag{226}$$

$$V_4 = \frac{1}{\cos\left(\frac{\tau}{2}\right)} \tag{227}$$

and Equation (223) solved again, X_1 is $\frac{d\Delta_1}{d\alpha}$ and X_3 is $\frac{d\Delta_1}{d\alpha}$

Differentiating Equations (156) and (157) with respect to the δ_j' gives for Δ and α at azimuth ϕ

$$\frac{d\Delta}{d\delta_1'} = \sin(\phi) \tag{228}$$

$$\frac{d\Delta}{d\delta_2'} = \cos(\beta)\sin(\phi) \tag{229}$$

$$\frac{d\Delta}{d\delta_3'} = \cos(\beta)\cos(\phi) \tag{230}$$

$$\frac{d\Delta}{d\delta_4'} = \frac{E}{2}\sin(\beta)\cos(\phi) \tag{231}$$

$$\frac{d\Delta}{d\delta_5'} = \frac{E}{2}\sin(\beta)\sin(\phi) \tag{232}$$

$$\frac{d\alpha}{d(\delta_1',\ \delta_2',\ \delta_3')} = 0 \tag{233}$$

$$\frac{d\alpha}{d\delta_4'} = \cos\phi \tag{234}$$

$$\frac{d\alpha}{d\delta_5'} = \sin\phi \tag{235}$$

The derivatives of P_1 and M_1 with respect to the δ_j are

$$\frac{dP_1}{d\delta_j'} = \left(\frac{dP_1}{d\Delta_1}\frac{d\Delta_1}{d\Delta} + \frac{dP_1}{d\alpha_1}\frac{d\alpha_1}{d\Delta}\right)\frac{d\Delta}{d\delta_j'} + \left(\frac{dP_1}{d\Delta_1}\frac{d\Delta_1}{d\alpha} + \frac{dP_1}{d\alpha_1}\frac{d\alpha_1}{d\alpha}\right)\frac{d\alpha}{d\delta_j'} \tag{236}$$

$$\frac{dM_1}{d\delta_j'} = \left(\frac{dM_1}{d\Delta_1}\frac{d\Delta_1}{d\Delta} + \frac{dM_1}{d\alpha_1}\frac{d\alpha_1}{d\Delta}\right)\frac{d\Delta}{d\delta_j'} + \left(\frac{dM_1}{d\Delta_1}\frac{d\Delta_1}{d\alpha} + \frac{dM_1}{d\alpha_1}\frac{d\alpha_1}{d\alpha}\right)\frac{d\alpha}{d\delta_j'} \tag{237}$$

160

$$\overline{F}_3 = \sum_{j=1}^{N_L} F_{3j} \tag{245}$$

$$\overline{F}_4 = \sum_{j=1}^{N_L} \left(F_{4j} + L_j\, F_{3j} \right) \tag{246}$$

$$\overline{F}_5 = \sum_{j=1}^{N_L} \left(F_{5j} + L_j\, F_{2j} \right) \tag{247}$$

Equilibrium of the system requires that

$$\overline{F}_1 + \sum_{i=1}^{N_B} F'_{1i} = \epsilon_1 \doteq 0 \tag{248}$$

$$\overline{F}_2 + \sum_{i=1}^{N_B} F'_{2i} = \epsilon_2 \doteq 0 \tag{249}$$

$$\overline{F}_3 + \sum_{i=1}^{N_B} F'_{3i} = \epsilon_3 \doteq 0 \tag{250}$$

$$\overline{F}_4 + \sum_{i=1}^{N_B} \left(F'_{4i} + L_i\, F'_{3i} \right) = \epsilon_4 \doteq 0 \tag{251}$$

$$\overline{F}_5 + \sum_{i=1}^{N_B} \left(F'_{5i} + L_i\, F'_{2i} \right) = \epsilon_5 \doteq 0 \tag{252}$$

For a given set of displacements δ_1 through δ_5 at the origin, the resulting displacements at a bearing location are

$$\delta'_{1i} = \delta_1 + \delta''_{1i} \tag{253}$$

$$\delta'_{2i} = \delta_2 + \delta''_{2i} + L_i\, \delta_5 - Z_{2i} \tag{254}$$

value of Y_1 and the minimum value of Y_2. Call these $\overline{Y}_1$ and $\overline{Y}_2$.

$$\ell_e = \overline{Y}_1 - \overline{Y}_2 \tag{261}$$

ℓ_e is the effective length of contact for the race concerned and can be thought of as a band of that width extending around the raceway. The band is now sliced by an appropriate number of planes perpendicular to the axis.

At each of these stations including the end ones, the unit pressure p is evaluated. A mean value of p is found depending on whether or not the race rotates with respect to load.

If the race rotates with respect to load, the mean load P_m is

$$P_{mi} = \left(\frac{1}{n} \sum_{j=1}^{n} P_{ji}^4\right)^{1/4} \qquad i = 1, \text{ number of stations} \tag{262}$$

If the race is stationary with respect to load

$$P_{mi} = \left(\frac{1}{n} \sum_{j=1}^{n} P_{ji}^{\frac{9}{2}}\right)^{\frac{2}{9}} \qquad i = 1, \text{ number of stations} \tag{263}$$

The capacity of a race contact at a station is

$$C = \frac{A\lambda \ (1 \pm \gamma_X)^{\frac{29}{27}} d_X^{\frac{29}{27}} \gamma_X^{\frac{2}{9}} \ell_e^{\frac{7}{9}}}{n^{1/4} \ (1 \mp \gamma_X')^{1/4}} \tag{264}$$

$$\gamma_X' = \frac{(d + 2X \sin(\frac{\tau}{2})) \cos(\beta)}{E + 2X \sin(\frac{\tau}{2}) \tan(\beta - \frac{\tau}{2})} \qquad \text{for outer} \tag{265}$$

$$\gamma_X' = \frac{(d + 2X \sin(\frac{\tau}{2})) \cos(\beta - \tau)}{E + 2X \sin(\frac{\tau}{2}) \tan(\beta - \frac{\tau}{2})} \qquad \text{for inner} \tag{266}$$

The upper signs in Equation (264) apply to an outer contact and the lower to an inner.

Since the fatigue effects are different at each station, they must be combined statistically to obtain an equivalent load for the entire contact:

$$Q_i = \ell_{ei} \left(\frac{1}{J} \sum_{k=1}^{J} \frac{P_{mik}}{C_i} \right)^{\frac{2}{9}} \qquad i, 1, 2 \qquad (267)$$

where J = the total number of stations.

The life of a set of contacts is

$$L_i = \left(\frac{1}{Q_i}\right)^4 \frac{16666.7}{|N_1 - N_2|} \qquad (268)$$

The life of the complete bearing is

$$\bar{L} = \left(\left(\frac{1}{L_1}\right)^{\frac{9}{8}} + \left(\frac{1}{L_2}\right)^{\frac{9}{8}} \right)^{-\frac{8}{9}} \qquad (269)$$